






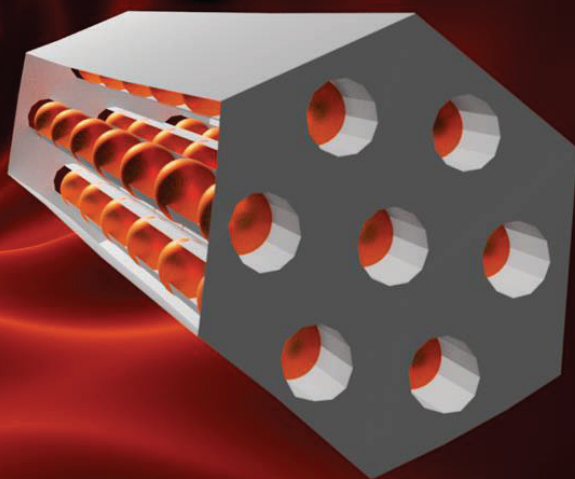
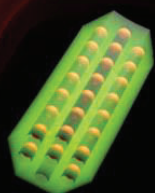
Universitat Autònoma de Barcelona

ADVERTIMENT. L'accés als continguts d'aquesta tesi queda condicionat a l'acceptació de les condicions d'ús establertes per la següent llicència Creative Commons:  http://cat.creativecommons.org/?page_id=184

ADVERTENCIA. El acceso a los contenidos de esta tesis queda condicionado a la aceptación de las condiciones de uso establecidas por la siguiente licencia Creative Commons:  <http://es.creativecommons.org/blog/licencias/>

WARNING. The access to the contents of this doctoral thesis it is limited to the acceptance of the use conditions set by the following Creative Commons license:  <https://creativecommons.org/licenses/?lang=en>

Magnetic and fluorescent mesoporous silica nanorods towards liver theranostic uses



Jan Grzelak
Doctoral Thesis
2021



**Universitat Autònoma
de Barcelona**

Magnetic and fluorescent mesoporous silica nanorods towards liver theranostic uses

Jan Grzelak

Doctoral thesis

Doctoral studies in Materials Science

Supervisors: Dr. Anna Roig Serra and Dr. Martí Gich Garcia

Departament de Química, Facultat de Ciències
Universitat Autònoma de Barcelona

2021

La **Dra. Anna Roig Serra**, professora d'investigació del CSIC, i el **Dr. Martí Gich Garcia**, científic titular del CSIC

Certifiquen:

Que en **Jan Grzelak**, graduat en Enginyeria de Nanoestructures per la Universitat de Varsòvia, Polònia, i amb un màster en Enginyeria de Nanoestructures per la Universitat de Varsòvia, Polònia, ha dut a terme aquesta tesi doctoral sota la seva direcció a l'Institut de Ciència de Materials de Barcelona (ICMAB-CSIC) i que presenta la memòria que porta per títol: "Magnetic and fluorescent mesoporous silica nanorods towards liver theranostic uses" per aspirar al títol de Doctor en Ciència de Materials per la Universitat Autònoma de Barcelona.

I perquè així consti, signen el present certificat

ROIG
SERRA
ANNA - DNI
39855642T



Firmado
digitalmente por
ROIG SERRA ANNA
DNI 39855642T
Fecha: 2021.08.20
11:09:05 +02'00'

Signat per GICH GARCIA
MARTI - DNI 33908278E el
20/08/2021 amb un
certificat digital emès
per AC Sector Público

Dr. Anna Roig
Directora de la Tesi

Dr. Martí Gich
Director i Tutor de la Tesi

Bellaterra, agost 2021

Nauczyłam się, że droga postępu nie jest ani szybka, ani łatwa
(I was taught that the way of progress is neither swift nor easy)

MARIA SKŁODOWSKA-CURIE



Obra Social "la Caixa"



**European
Commission**

Horizon 2020
European Union funding
for Research & Innovation

The project that gave rise to these results received the support through the INPhINIT Fellowship Grant for Doctoral Studies at Spanish Research Centers of Excellence from the "la Caixa" Foundation (ID **100010434**). The fellowship code is **LCF/BQ/DI17/11620041**.

This project has received funding from the European Union's Horizon 2020 research and innovation programme under the Marie Skłodowska-Curie grant agreement No. **713673**.

Acknowledgments

When I arrived in Barcelona for a semester of student exchange, I could not imagine that within five years I would be finishing my doctoral thesis here. I was warmly welcomed in the group of Nanoparticles and Nanocomposites at ICMAB by Anna Roig who encouraged me to apply for a “la Caixa” INPhINIT fellowship for PhD studies. I will always be grateful for this, Anna. On this occasion, I also thank the “la Caixa” Foundation for giving me this opportunity.

A wise scientist once said that the way of progress is neither swift nor easy. Indeed, it was not always easy. However, I believe that the most important thing about PhD studies is what one learns along the way. I feel that during this time I have developed as a scientist and as a person. I would like to thank everybody who has been a part of this valuable journey.

First of all, my supervisors Anna Roig and Martí Gich. Anna, thank you for believing in me, for your patience and professionalism. Your calm and balance has many times restored my faith in the meaning of my work. Martí, thank you for your valuable comments, creative ideas and your help with the experiments. The frequent supervisory meetings with both of you were very useful and have guided me through the project. Thank you for always having time for me.

I am very grateful to all the scientific and technical personnel of ICMAB for performing the experiments and providing the trainings. Especially Judith Oró, Bernat Bozzo, Julio Fraile and the Nanoquim technical staff.

All the present and past members of the N&N group which is a very special, multidisciplinary and multicultural community where everyone feels at home and always learns new things. My friend and office mate Ma, thanks to you the office has been a happy place. Thank you for your friendship. Sumi, thank you for enjoying my jokes and being always willing to help. Miquel, you are my ICMAB brother. Sole, you were one of the first friends I made at ICMAB and have never let me down. Wid, I have known you for a short time but you have helped me a lot. Amanda, your work ethic is inspiring. Thomas, thank you for taking some nice pictures of my samples. Andrea, for sharing the cyanine. Darla, I hope we will have the opportunity to play volleyball together. Jordi, thank you for hosting me when I was looking for a flat in Barcelona. All my friends from ICMAB and the neighboring research centres. Artur, Noemí, Cristina, Juri and all co-organizers of JPhD – organizing a big conference for PhD students was a fun and enriching experience, and we made a great team!

My fellow “la Caixa” fellows. It has been an honor to be a part of this group together with so many talented and creative people. Elena, I could not imagine a better friend. José, thank you for always being so helpful with the paperwork at ICMAB. Albert,

Aljoša, Andrea, Carmen, Giulia, Valentina and others. I hope that the end of the PhD will not be the end of our friendship.

The “la Caixa” foundation, thank you for putting so much effort in the organization of the trainings. You have created this group and contributed to many long-lasting friendships and collaborations. You also made sure we learned other useful skills such as presenting our work or project management.

During the elaboration of my doctoral project I have had the pleasure to work with some exceptional collaborators.

Alba Grayston, thank you for your professionalism and your help in analysing the FMI results.

Jaume Gázquez, thank you for performing the EELS measurements and for helping me with the interpretation of the results.

All the members of the IE group, thanks to you I have been feeling like an integral member of the zebrafish team. Mariana Teles, thank you for your positive attitude, for teaching me a topic that was completely new to me in such a short time, and your help with planning the experiments. Nerea Roher, thank you for your time and sharing your knowledge about zebrafish. Irene, for your advice regarding the ZFL cell cultures. Mauricio, for teaching me to operate the fluorescence microscope.

The members of the Smart Nano-Bio-Devices group at IBEC, thank you for the collaboration in the exciting field of catalytic nanomotors.

The members of the SeLiver group. I wish I could spend more time in Sevilla but still I have learned so much! Manuel Romero, thank you for making the research stay in your group possible. Ángela Rojas, thank you for your kindness and for teaching me everything. Rocío, Sheila and Rocío, for all the laughs and Mercadona lunches.

Special thanks to my uncle (Wuj) Ryszard for all his invaluable help.

To my dear Mum and Dad. Thank you so much for always supporting me, always believing in me, for all your sacrifices, for always thinking of me before yourselves. I am in this place thanks to you. I love you so much.

Attributions

I would like to thank the people who contributed to this thesis:

- Judith Oró (ICMAB) performed the TEM measurements.
- Mariana Teles and Nerea Roher (Evolutionary Immunology group, IBB-UAB) trained me in ZFL cell culture, cell viability assays, zebrafish larvae management, and supervised my work at IBB-UAB.
- Alba Grayston (Neurovascular Diseases group, VHIR) managed the FMI *in vitro* and *in vivo* studies and helped me analyse the results.
- Ángela Rojas (SeLiver group, IBiS, Sevilla) trained me in Huh7.5 cell culture and cell viability assays and supervised my work at IBiS.
- Julio Fraile (ICMAB) performed the nitrogen adsorption measurements.
- Bernat Bozzo and Ferran Vallès (ICMAB) performed the SQUID magnetometry measurements.
- Amable Bernabé (ICMAB) trained me in DLS/zeta potential measurements.
- Anna Esther Carrillo (ICMAB) trained me to use SEM and performed some of the measurements.
- Daniel Padro (CICbiomaGUNE) managed the *in vivo* MRI studies.
- Jaume Gázquez (ICMAB) performed the STEM-EELS measurements and helped me interpret the results.
- Fernando Herranz (IQM, Madrid) performed the MRI *in vitro* imaging of the phantoms.
- Rafael Mestre, Núria Cadefau, Ana Hortelão (Smart Nano-Bio-Devices group, IBEC) performed the motion dynamics studies of catalytic nanomotors.
- Anna Crespi, Javier Campos and Joan B. Esquius (ICMAB) performed the XRD and SAXS measurements.
- Marta Gerbolés, Neus Romà, Luigi Morrone, Marta Riba (Nanoquim platform, ICMAB) trained me in the use of clean room facilities (tubular furnace, fluorometer). Marta Gerbolés also trained me in the use of plate reader.
- Vega Lloveras (ICMAB) trained me in FT-IR spectroscopy.
- Guillermo Antorrena (LMI unit, Universidad de Zaragoza) performed the XPS measurements.
- The undergraduate student Marc Cervantes helped me develop the protocol for the amino-functionalization of silica rods.
- David Piña (ICMAB) trained me in the use of the lyophilizer.
- Marcos Rosado (ICN2) performed the EDX mapping.
- Roberta Ceravola (ICMAB) performed the TGA analysis.
- Ignasi Villarroya and Sandra Izquierdo (Chemical Analysis service, UAB) performed the ICP-OES analysis.
- Martina Capozza (*Ephoran*, Italy) performed the US imaging studies.

Abstract

In recent years, mesoporous silica nanoparticles have been widely studied in nanomedicine as nanocarriers for diagnostic and therapeutic purposes. However, most of the research has focused on spherical particles, whereas the effect of the particle shape on the toxicity, cell uptake and biodistribution has been marginally investigated. We hypothesize that mesoporous silica-based nanomaterials with rod-like morphology could present high liver accumulation and could be used as liver-targeting agents to treat hepatic pathologies. In particular, for the early diagnosis and treatment of non-alcoholic fatty liver disease (NAFLD), which has a high and ever-increasing global prevalence.

In this dissertation, I synthesized and extensively characterized mesoporous silica rods of well-defined sizes and two distinct aspect ratios. The rods were endowed with different surface charges, functional imaging moieties and a potential therapeutic capability. I studied the toxicity, cell uptake and biodistribution of the rods using *in vitro* and *in vivo* models, assessed the imaging potential of the rods using two imaging techniques and observed their high accumulation in the liver.

The thesis is organized as follows:

- **Chapter 1:** contains the state of the art and the thesis objectives.
- **Chapter 2:** focuses on the synthesis of silica rods and their characterization in terms of morphology and porosity.
- **Chapter 3:** explores strategies to load silica rods with different chemical species and reports the material characterization in terms of loading efficiency, chemical and phase composition, and magnetic properties. To this aim, the rods were functionalized by synthesizing nanoparticles inside the silica pores. In particular, the following specific theranostic functionalizations were addressed:
 - Magnetic gamma-Fe₂O₃ nanoparticles as MRI contrast agents,
 - Bismuth, barium and gold compounds as CT contrast agents,
 - Hollow silica channels as potential US agents,
 - Ceria as a potential therapeutic agent.
 - The capability of the rods as self-propelled nanomotors.
- **Chapter 4:** reports the functionalization of the silica surface with amine groups endowing the rods with positive surface charge and facilitating the anchoring of fluorophores with different emission wavelengths (fluorescamine, Cyanine5) for applications in optical imaging.
- **Chapter 5:** evaluates the *in vitro* and *in vivo* toxicity, uptake and biodistribution of silica rods. The toxicity is assessed by viability studies performed on zebrafish and human liver cells, as well as *in vivo* studies on zebrafish larvae and rodents. Uptake by liver cells *in vitro* and biodistribution in different organs *in vivo* is also studied.
- **Chapter 6:** lists the general conclusions of the thesis and suggests a few directions of future work.

Resumen

En los últimos años, las nanopartículas de sílice mesoporosa han sido ampliamente estudiadas para su uso como nanovehículos con fines diagnósticos y terapéuticos. Sin embargo, la mayor parte de estos estudios se han centrado en el uso de partículas esféricas, mientras que el efecto de la forma de las partículas sobre la toxicidad, la captación celular y la biodistribución se ha investigado de una forma más marginal. Nuestra hipótesis de partida ha sido que los nanomateriales de sílice mesoporosa con morfología en forma de rods podrían presentar una elevada acumulación en el hígado y ser de utilidad en patologías hepáticas. En particular, para el diagnóstico y tratamiento precoz de la enfermedad del hígado graso no alcohólico (NAFLD, según las siglas en inglés), una enfermedad con una alta prevalencia global y en constante aumento.

En esta tesis, he sintetizado y caracterizado exhaustivamente rods de sílice mesoporosa de tamaños bien definidos y con dos relaciones de aspecto distintas. Además, los rods se han funcionalizado para obtener diferentes cargas superficiales, varias funcionalidades y una potencial capacidad terapéutica. He estudiado su toxicidad, captación celular y su biodistribución utilizando modelos *in vitro* e *in vivo* y he podido confirmar su potencial como agentes de contraste para dos técnicas de imagen, así como su alta acumulación en el hígado.

La tesis está organizada de la forma siguiente:

- **Capítulo 1:** contiene el estado del arte y los objetivos de la tesis.
- **Capítulo 2:** se centra en la síntesis de rods de sílice y su caracterización.
- **Capítulo 3:** explora las estrategias investigadas para cargar los rods de sílice con diferentes especies químicas y la caracterización de materiales en términos de eficiencia de carga, composición química, estructura cristalográfica y propiedades magnéticas. Para ello, los rods se funcionalizaron sintetizando nanopartículas en el interior de los poros de sílice. En particular, se abordaron las siguientes funcionalizaciones:
 - Nanopartículas magnéticas de $\gamma\text{-Fe}_2\text{O}_3$ como agentes de contraste de resonancia magnética,
 - Compuestos de bismuto, bario y oro como agentes de contraste de tomografía computarizada,
 - Canales vacíos de sílice como posibles agentes de ultrasonografía,
 - Ceria como potencial agente terapéutico.
 - La capacidad de los rods como nanomotores autopropulsados.
- **Capítulo 4:** reporta la funcionalización de la superficie de sílice con grupos amina que dotan los rods de carga superficial positiva y facilitan el anclaje de fluoróforos con diferentes longitudes de onda de emisión (fluorescamina, cianina 5) para sus aplicaciones en imagen óptica.
- **Capítulo 5:** analiza la toxicidad, captación y biodistribución *in vitro* e *in vivo* de los rods de sílice. La toxicidad se evalúa mediante estudios de viabilidad realizados en células hepáticas de pez cebra y humanas, así como mediante estudios *in vivo* en larvas de pez cebra y roedores. También se estudia la captación de los rods por las células hepáticas *in vitro* y su biodistribución en diferentes órganos *in vivo*.
- **Capítulo 6:** enumera las conclusiones generales de la tesis y sugiere algunas direcciones de trabajo futuro.

Resum

En els darrers anys, les nanopartícules de sílice mesoporosa s'han estudiat àmpliament en nanomedicina com a nanovehicles amb fins diagnòstics i terapèutics. No obstant això, la major part d'aquests estudis s'han centrat en partícules esfèriques, mentre que l'efecte de la forma de les partícules en la toxicitat, la captació cel·lular i la seva biodistribució s'ha estudiat de forma més marginal. La nostra hipòtesi de partida és que nanomaterials mesoporosos de sílice en forma de rods podrien presentar una elevada acumulació en el fetge i ser d'utilitat en patologies hepàtiques. En particular, pel diagnòstic i tractament precoç de la malaltia del fetge gras no alcohòlic (NAFLD, segons les seves sigles en anglès), una malaltia amb una prevalença global alta i en constant augment.

En aquesta tesi, he sintetitzat i caracteritzat exhaustivament rods de sílice mesoporosa de mida ben definida i amb dues relacions d'aspecte. Els rods poden dotar-se de càrregues superficials diferents, varies funcionalitats i tenen una potencial capacitat terapèutica. He estudiat la seva toxicitat, captació cel·lular i biodistribució utilitzant models *in vitro* i *in vivo*. He pogut confirmar la seva aplicabilitat com a agents de contrast en dues tècniques d'imatge mèdiques i la seva alta acumulació en el fetge.

La tesi està organitzada de la següent manera:

- **Capítol 1:** conté l'estat de l'art i els objectius de la tesi.
- **Capítol 2:** es centra en la síntesi de rods de sílice i la seva caracterització.
- **Capítol 3:** explora les estratègies investigades per carregar els rods de sílice amb diferents espècies químiques i la caracterització dels materials en termes d'eficiència de càrrega, composició química, estructura cristal·logràfica i propietats magnètiques. Per a aquestes funcionalitzacions s'han sintetitzat nanopartícules a l'interior dels porus de la sílice. En particular, es van abordar les funcionalitzacions següents:
 - Nanopartícules magnètiques de gamma-Fe₂O₃ com a agents de contrast de ressonància magnètica,
 - Compostos de bismut, bari i or com a agents de contrast per tomografia computeritzada,
 - Canals buits de sílice com a possibles agents de ultrasonografia,
 - Ceria com a potencial agent terapèutic.
 - La capacitat dels rods com nanomotors autopropulsats.
- **Capítol 4:** descriu la funcionalització de la superfície de la sílice amb grups amina que doten als rods de càrrega superficial positiva i faciliten l'ancoratge de fluoròfors amb diferents longituds d'ona d'emissió (fluorescamina, cianina 5) per a aplicacions en imatge òptica.
- **Capítol 5:** analitza la toxicitat, captació i biodistribució *in vitro* i *in vivo* dels rods de sílice. La toxicitat s'ha avaluat mitjançant estudis de viabilitat realitzats en cèl·lules hepàtiques de peix zebra i humanes, així com mitjançant estudis *in vivo* en larves de peix zebra i rosegadors. També s'ha estudiat la captació per les cèl·lules hepàtiques *in vitro* i la biodistribució en diferents òrgans *in vivo*.
- **Capítol 6:** enumera les conclusions generals de la tesi i suggereix algunes direccions de treball futur.

Streszczenie

W ostatnich latach, nanocząstki mezoporowatej krzemionki stały się przedmiotem wielu badań w nanomedycynie jako nanoosiłki do celów diagnostycznych i terapeutycznych. Jednakże, większość badań jest poświęcona cząstkom sferycznym, podczas gdy wpływ kształtu cząstek na toksyczność, absorpcję przez komórki oraz biodystrybucję nie zostały wystarczająco zbadane. Zakładamy, że nanomateriały w kształcie drutów oparte na mezoporowatej krzemionce mogłyby znaleźć zastosowanie w patologich wątroby. W szczególności, do wczesnego wykrywania i leczenia niealkoholowego stłuszczenia wątroby (z ang. NAFLD), schorzenia dotykającego dużej populacji, która stale się zwiększa.

W niniejszej pracy, dokonałem syntezy i szczegółowej charakteryzacji drutów z mezoporowatej krzemionki o dobrze zdefiniowanych rozmiarach i dwóch różnych współczynnikach proporcji. Druty zostały wyposażone w różne ładunki powierzchniowe i przystosowane do wykorzystania w obrazowaniu medycznym oraz, potencjalnie, w terapii. Badałem toksyczność, absorpcję przez komórki oraz biodystrybucję drutów stosując je na modelach *in vitro* i *in vivo*, potwierdziłem ich potencjał do zastosowania w obrazowaniu dwoma różnymi technikami oraz zaobserwowałem znaczącą kumulację w wątrobie.

Praca jest zorganizowana w następujący sposób:

- **Rozdział 1.:** zawiera przegląd obecnej wiedzy i cele pracy.
- **Rozdział 2.:** skupia się na syntezie drutów z mezoporowatej krzemionki i na ich charakteryzacji.
- **Rozdział 3.:** bada strategie wypełniania krzemionkowych drutów różnymi substancjami chemicznymi i informuje o charakteryzacji materiału pod względem efektywności wypełniania, składu chemicznego, struktury krystalograficznej oraz właściwości magnetycznych. W tym celu, druty zostały zfunkcjonalizowane przez syntezę nanocząstek wewnątrz porów krzemionki. W szczególności, zostały uwzględnione następujące przystosowania teranostyczne:
 - Magnetyczne nanocząstki odmiany gamma tlenku żelaza jako środki kontrastowe w rezonansie magnetycznym,
 - Związki bizmutu, baru i złota jako środki kontrastowe w tomografii komputerowej,
 - Niewypełnione kanały krzemionki jako potencjalny kontrast w ultrasonografii,
 - Tlenek ceru jako potencjalny środek terapeutyczny,
 - Zastosowanie drutów jako samonapędzające się nanomotory.
- **Rozdział 4.:** informuje o modyfikacji powierzchni krzemionki grupami aminowymi, która wyposaża druty w dodatni ładunek powierzchniowy i umożliwia przyłączanie fluoroforów emitujących promieniowanie o różnych długościach fali (fluoreskamina, cyjanina 5) do zastosowania w obrazowaniu optycznym.
- **Rozdział 5.:** ocenia toksyczność, absorpcję i biodystrybucję drutów krzemionkowych *in vitro* i *in vivo*. Toksyczność oceniano stosując badania żywotności komórek wątroby ryby Danio przęgowanego oraz komórek wątroby ludzkiej, jak również badania *in vivo* przeprowadzone na larwach Danio przęgowanego oraz gryzoni. Absorpcja przez komórki wątroby *in vitro* i dystrybucja w poszczególnych organach w modelach *in vivo* jest również przedmiotem analizy.
- **Rozdział 6.:** przedstawia ogólne wnioski z pracy i proponuje kilka kierunków dalszych badań.

Abbreviations

ADF	Annular Dark Field
APTES	(3-Aminopropyl)triethoxysilane
AR	Aspect ratio
ASGPR	Asialoglycoprotein receptor
ASO	Antisense oligonucleotide
BET	Brunauer-Emmett-Teller
CA	Contrast agent
CT (1)	Computed tomography
CT (2)	Control
CTM	Cooperative templating mechanism
Cy	Cyanine
Cy5	Cyanine5
d	Diameter
D_{BJH}	Barrett–Joyner–Halenda pore diameter
d_{hkl}	Distance between (hkl) Miller planes
D_p	Pore diameter
EDX	Energy-dispersive X-ray spectroscopy
EELS	Electron energy loss spectroscopy
f	Stirring rate
FC	Field cooling
$Fe_2O_3@LR$	Long rods loaded with iron oxide nanoparticles
$Fe_2O_3@SR$	Short rods loaded with iron oxide nanoparticles
$Fe_2O_3@SR-Cy5$	Short rods loaded with iron oxide nanoparticles and functionalized with Cyanine5
FFP	Filtering facepiece
FMI	Fluorescence molecular imaging
FT-IR	Fourier transform infrared spectroscopy
GalNAc	N-Acetylgalactosamine

IBB-UAB	<i>Institut de Biotecnologia i de Biomedicina</i>
IBEC	<i>Institute for Bioengineering of Catalonia</i>
IBiS	<i>Instituto de Biomedicina de Sevilla</i>
ICMAB	<i>Institut de Ciència de Materials de Barcelona</i>
ICN2	<i>Institut Català de Nanociència i Nanotecnologia</i>
ICP-OES	Inductively coupled plasma - optical emission spectrometry
ID (1)	Identification
ID (2)	Injected dose
IUPAC	International Union of Pure and Applied Chemistry
k_B	Boltzmann constant
L	Length
LR	Long rods
LR-FL	Long rods functionalized with fluorescamine
m_r	Remanent magnetic moment
M_r	Magnetic remanence
MRI	Magnetic resonance imaging
mRNA	Messenger ribonucleic acid
M_s	Saturation magnetization
MSN	Mesoporous silica nanoparticles
MSNR	Mesoporous silica nanorods
MSNS	Mesoporous silica nanospheres
MSR	Mesoporous silica rods
MTT	3-(4,5-dimethylthiazol-2-yl)-2,5-diphenyltetrazolium bromide
NAFLD	Non-alcoholic fatty liver disease
NASH	Non-alcoholic steatohepatitis
NHS	N-Hydroxysuccinimide
NIR	Near-infrared
NP	Nanoparticles
P	Calculated probability
p	Pressure

P123	Pluronic P123
PET	Positron emission tomography
ROI	Region of interest
ROS	Reactive oxygen species
rpm	Revolutions per minute
SAXS	Small angle X-ray spectroscopy
SBA-15	Santa Barbara Amorphous-15 mesoporous silica
S _{BET}	Brunauer-Emmett-Teller surface area
SEM	Scanning electron microscopy
SI	Spectrum image
SPIONs	Superparamagnetic iron oxide nanoparticles
SQUID	Superconducting quantum interference device
SR	Short rods
SR-Cy5	Short rods functionalized with Cyanine5
SR-FL	Short rods functionalized with fluorescamine
STEM	Scanning transmission electron microscopy
Stk25	Serine/Threonine Kinase 25
T ₁	Longitudinal relaxation time
T ₂	Transverse relaxation time
T ₂ *	Transverse relaxation time acquired in axial planes
T _a	Aging temperature
t _a	Aging time
TEM	Transmission electron microscopy
TEOS	Tetraethyl orthosilicate
TGA	Thermogravimetric analysis
T _m	Melting point
TMOS	Tetramethyl orthosilicate
t _r	Reaction time
TRE	Total radiant efficiency
T _s	Synthesis temperature

t_s	Stirring time
UAB	<i>Universitat Autònoma de Barcelona</i>
US	Ultrasound imaging
UV-Vis	Ultraviolet–visible absorption spectroscopy
v	Volume
V_b	Volume of the bottle
VHIR	<i>Vall d’Hebron Institut de Recerca</i>
V_M	Magnetic volume
V_p	Pore volume
V_r	Reaction mixture volume
V_{total}	Total pore volume
w	Width
wt.	Weight
x g	Times gravity
XPS	X-ray photoelectron spectroscopy
XRD	X-ray diffraction
ZFC	Zero-field cooling
ZFL	Zebrafish liver cell line
$\alpha\text{-Fe}_2\text{O}_3$	Hematite
$\gamma\text{-Fe}_2\text{O}_3$	Maghemite
δ	Depth
λ_{em}	Emission wavelength
λ_{ex}	Excitation wavelength
λ_{IMFP}	Inelastic mean free path
μ	Magnetic moment
ρ	Density

Table of contents

Acknowledgments	ix
Attributions	xi
Abstract/Resumen/Resum/Streszczenie	xiii
Abbreviations	xxi
1. State of the art and objectives	1
1.1. Introduction	3
1.2. Multimodal imaging and theranostics	3
1.3. Mesoporous silica formulations	6
1.4. Shape and size of mesoporous silica particles	8
1.5. Synthesis of mesoporous silica nanoparticles	11
1.6. NAFLD - current diagnosis and treatment strategies	13
1.7. Objectives of the thesis	16
1.8. Chapter references	17
2. Mesoporous silica nanorods: synthesis and characterization	25
2.1. Synthesis of MSR	27
2.1.1. Introduction	27
2.1.2. Influence of reaction conditions on silica morphology	29
2.1.3. Properties of MSR	37
2.2. Chapter summary	42
2.3. Annex	43
2.3.1. Materials	43
2.3.2. Synthesis of long rods (LR)	43
2.3.3. Synthesis of short rods (SR)	43
2.3.4. Soxhlet cleaning	43
2.3.5. Calcination	44
2.3.6. Transmission electron microscopy (TEM)	44
2.3.7. Scanning electron microscopy (SEM)	44
2.3.8. Nitrogen adsorption/desorption isotherm	44
2.3.9. Small angle X-ray scattering (SAXS)	44
2.3.10. Thermogravimetric analysis	45
2.3.11. Safety	45

2.4. Chapter references	46
3. Loading the pores of the silica rods with chemical species	47
3.1. Introduction	49
3.2. In-situ fabrication of γ -Fe ₂ O ₃ NPs	49
3.2.1. Introduction	49
3.2.2. Loading and characterization	50
3.2.3. MRI performance of magnetic silica rods	64
3.2.4. Application as self-propelled nanomotors	66
3.3. Evaluation of MSRs as US contrast agents	66
3.4. Loading with ceria NPs for therapeutic purposes	67
3.5. Loading with potential CT contrast agents	72
3.6. Chapter summary	75
3.7. Annex	76
3.7.1. Materials	76
3.7.2. Synthesis of maghemite nanoparticles inside silica mesopores	76
3.7.3. Synthesis of cerium oxide nanoparticles inside silica mesopores	76
3.7.4. MSR loading with iron and cerium compounds	76
3.7.5. MSR loading with gold compound	77
3.7.6. MSR loading with barium compound	77
3.7.7. MSR loading with bismuth compounds	77
3.7.8. Silica etching	77
3.7.9. X-ray diffraction	78
3.7.10. Transmission electron microscopy (TEM)	78
3.7.11. Scanning electron microscopy (STEM) with electron energy loss spectroscopy (EELS)	78
3.7.12. Magnetometry (SQUID)	78
3.7.13. Elemental analysis by inductively-coupled plasma emission spectrometry (ICP-OES)	79
3.7.14. Energy-dispersive X-ray spectroscopy (EDX)	79
3.7.15. Small angle X-ray spectroscopy (SAXS)	79
3.7.16. MRI studies	79
3.7.17. Motion studies of MSR-based nanomotors	79
3.7.18. US studies	80

3.8. Chapter references	81
4. Surface functionalization of silica rods and conjugation of fluorophores	83
4.1. Introduction	85
4.2. Aminofunctionalization of silica rods	85
4.2.1. Introduction	85
4.2.2. MSR functionalization and characterization	86
4.3. Functionalization of MSRs with fluorophores	92
4.3.1. Functionalization with fluorescamine	92
4.3.2. Functionalization with Cy5	93
4.4. Chapter summary	97
4.5. Annex	98
4.5.1. Materials	98
4.5.2. Amino-functionalization of MSRs	98
4.5.3. Zeta potential measurements	98
4.5.4. Transmission electron microscopy (TEM)	98
4.5.5. Fourier transform infrared spectroscopy (FT-IR)	98
4.5.6. X-ray photoelectron spectroscopy (XPS)	99
4.5.7. MSR functionalization with fluorescamine	99
4.5.8. MSR functionalization with Cyanine5	99
4.5.9. Fluorescence spectroscopy	99
4.5.10. Ultraviolet-visible (UV-Vis) absorption spectroscopy	100
4.5.11. Fluorescence imaging	100
4.6. Chapter references	101
5. Cell and animal studies	103
5.1. Introduction	105
5.2. In vitro studies of MSRs	106
5.2.1. ZFL cell viability and uptake	106
5.2.2. Huh7.5 cell viability and uptake	109
5.3. Uptake of MSRs in zebrafish larvae and effects on survival	111
5.4. MRI imaging in rats	114
5.5. Fluorescence molecular imaging in mice	122
5.6. Chapter summary	125
5.7. Annex	126

5.7.1. Materials	126
5.7.2. ZFL cell viability studies	126
5.7.3. ZFL cell uptake studies	126
5.7.4. Huh7.5 cell viability and uptake studies	127
5.7.5. Uptake and toxicity studies in zebrafish larvae	127
5.7.6. In vivo MRI studies in rats	128
5.7.7. In/ ex vivo fluorescence imaging in mice	129
5.8. Chapter references	131
6. Conclusions	133
6.1. General conclusions	135
6.2. Outlook and future perspectives	136

Chapter 1

State of the art and objectives

1.1. Introduction

Despite great accomplishments and the constant development of medicine and science, there is still an urgent need for new strategies to diagnose and treat human diseases. Recent years have seen an increasing interest of the medical field in nanotechnology-based formulations.^{1,2} The unique properties of nanomaterials have been exploited to identify disease markers or deliver drugs to specific sites in the organism.³ Changing the morphology and chemical composition of nanomaterials allows us to tune their optical, electrical, or magnetic properties.⁴ In particular, nanoparticle (NP) formulations can be used in diagnostic, therapeutic, or combined (theranostic) applications.⁵ An advantage of nanoparticle-based vectors carrying imaging contrast agents or therapeutics is that they can be engineered to target specific cells, organs or tissues, limiting their systemic effects, in contrast to other more conventional treatments.⁶ Moreover, the high surface to volume ratio of nanomaterials allows loading the material with high doses of therapeutics or imaging agents.

The potential of nanoparticles has been exploited in various *in vitro* diagnostic devices, which are available for patient use or are being clinically evaluated.⁷⁻¹⁰ *In vivo* formulations also show great prospects to be beneficial for diagnosis and treatment of diseases, and increasingly diverse materials are appearing in clinical trials.¹¹ A very relevant recent example of the potential impact of nanomaterials on public health in the years to come are the COVID-19 vaccines developed by Pfizer-BioNTech and Moderna, consisting of mRNA encapsulated in lipid nanoparticles.^{12,13}

Nanomaterial formulations are associated with certain challenges, such as the potential toxicity or incompatibility of the nanomedicine upon interaction with a biological environment which could lead to immune reactions, inflammation and other cytotoxic effects.¹⁴ Other obstacles include nonspecific distribution and inadequate accumulation of the carriers.¹⁵ Nanomaterial interactions with the physiological environment depend on their size, shape, surface charge and chemical composition.¹⁶ Therefore, apart from being properly designed to perform their intended function, the new potential theranostic agents should be carefully studied in terms of biocompatibility, biodegradability and potential cytotoxicity.^{3,14,17,18}

1.2. Multimodal imaging and theranostics

As a result of the heterogeneity of human diseases and how they vary between patients, large amounts of detailed information about the progress of the disease are often needed.¹⁹ *In vivo* medical imaging techniques provide specific visualisations of the human body to diagnose, treat or monitor diseases.²⁰⁻²² Representative imaging modalities include magnetic resonance imaging (MRI), optical imaging, ultrasound imaging (US), X-ray computed tomography (CT), positron emission tomography

(PET), single-photon emission computed tomography (SPECT) and photoacoustic imaging. Each imaging modality gives different information about the area of interest and each has its advantages as well as drawbacks, such as low resolution or low sensitivity.

MRI is an imaging modality that can provide both structural and functional information of body tissues and organs. It has an excellent spatial resolution (depending on the magnetic field) and is used to acquire high-resolution anatomical images while providing excellent contrast.²³ MRI contrast in biological systems is produced as a result of different relaxation times of hydrogen proton spins in the organism under an external magnetic field, which depends on the microenvironment of the protons. Relaxation processes are characterized by the longitudinal (T_1) and transverse relaxation (T_2) times. Despite the excellent natural contrast of MRI, sometimes the use of contrast agents (CA) is required to better detect pathologies.²⁴ The MRI CAs shorten T_1 or T_2 relaxation times through magnetic interaction with neighboring water protons. T_1 agents, also known as positive contrast agents, increase the MRI signal intensity around them (brighter images), and are composed of paramagnetic materials based either on gadolinium or manganese, or consist of very small iron oxide nanoparticles.²⁵ On the other hand, T_2 (negative) contrast agents decrease the signal, resulting in darker images. Superparamagnetic iron oxide is often applied as a negative contrast agent.²⁶ The effect of MRI contrast agents is usually quantified using relaxivity values ($r_1=1/T_1[CA]$ or $r_2=1/T_2[CA]$).

Computed tomography (CT) is a technique that provides anatomical information by measuring the absorption of X-rays through tissues. This is characterized by the attenuation coefficient, dependent on the chemical composition and density of the tissue. Bones, fat, air and water all absorb the radiation differently and those differences provide anatomical contrast images.²⁷ CT using contrast agents has the advantage of short acquisition time and high resolution.²² Nanoparticles designed as CT contrast agents usually contain elements with high atomic numbers and large electron densities, such as iodine, bismuth, or gold.²⁸ Especially iodine-based contrast agents have been widely applied for this purpose.²⁹ However, iodinated molecules are characterized by rapid renal clearance and may induce toxicity in the kidneys.

Ultrasound imaging is one of the most frequently used clinical imaging modalities owing to its low cost, speed, and noninvasiveness. In this modality, a transducer that emits high-frequency sound waves (>20 kHz) is put in contact with the skin and the ultrasounds are reflected back from the internal organs.³⁰ US contrast agents are materials, such as gas, with acoustic properties which are radically different from those of the tissues.³¹ Materials employed as US contrast agents include bubbles filled with different gases, composed of soft- or hard-shell materials, in the size of nano- to micrometers.³²⁻³⁶ Recent studies have also reported contrast agents composed of silica nanoparticles filled with air, generating bubbles while subjected to an ultrasound pulse.³⁷

Optical imaging involves the detection of photons emitted from bioluminescent or fluorescent probes. Advantages of this technique include its noninvasiveness, high sensitivity, cost-effectiveness, the use of nonionizing radiation, as well as the possibility of imaging in real-time in a broad spectrum of light (from visible to near-infrared).^{22,38} For these reasons, *in vitro* and preclinical optical imaging is attracting much interest. On the other hand, optical imaging suffers from poor tissue penetration (0-2 cm) and susceptibility to noise. However, the near-infrared (NIR) tissue biological window (650-950 nm, NIR-I and 1000-1700 nm, NIR-II) is characterized by reduced tissue absorption and scattering, resulting in greater penetration depth and offering great potential for *in vivo* imaging applications.³⁹

Using a single imaging modality may be insufficient to obtain reliable and accurate information about the disease site. This approach may lead to errors, such as true-negative or false-positive results in the diagnosis of patients with cancer.²² Due to the limitations of each modality, monomodal imaging often cannot provide all the necessary anatomical, physiological or molecular information. Recently, imaging using multimodal nanoparticles has attracted significant attention as it can combine the advantages and minimize the limitations of each individual imaging modality, providing more accurate and detailed information about the body.²² Many possible modality combinations have been studied, including MRI-optical, MRI-PET, or MRI-CT. Figure 1-1 presents relevant examples of materials used as contrast agents for different modalities and types of platforms that have been used to incorporate them.

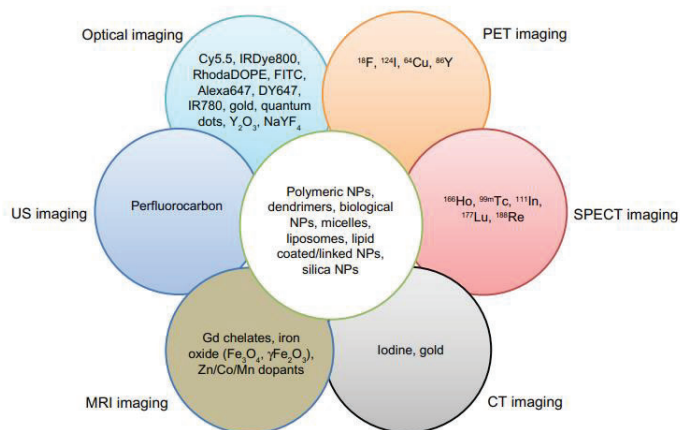


Figure 1-1. Materials incorporated in various multimodal imaging agents. This figure is obtained from *International Journal of Nanomedicine* (2014) by J. Key & J. Leary²²

Even though the combination of different imaging modalities should provide more detailed diagnostic information, it is important to rationally select imaging modalities to be incorporated into a nanocarrier, so that their synergistic effect is maximized.¹⁹ Another aspect that should be considered is the amount of each contrast material. For example, techniques such as MRI or CT need relatively high concentrations of contrast agents, unlike fluorescence imaging.⁴⁰

Multifunctionality of nanocarriers encompasses the integration of both imaging and therapeutic agents. Recently, imaging techniques have been combined with therapy to obtain biological information, confirm the accumulation of NPs at the target site or monitor the results of therapy.^{41,42} Various types of building blocks have been used to incorporate multimodal imaging contrast agents and therapeutics, including organic (liposomes, polymeric micelles, dendrimers) and inorganic (iron, gold or silica NPs) systems.

1.3. Mesoporous silica formulations

Among the materials investigated as potential nanocarriers for nanomedicine formulations, mesoporous silica particles have attracted much research attention.^{43–45} Mesoporous silica nanoparticles (MSNs) are solid materials that contain hundreds of empty channels (mesopores – having a diameter between 2 and 50 nm, according to IUPAC classification), with a homogeneous size distribution.^{46–48} In contrast to other amorphous silica materials, MSNs exhibit superior biocompatibility at concentrations used for pharmacological applications.^{49,50} Encapsulation of therapeutic or diagnostic agents inside mesoporous silica materials has certain advantages over conventional formulations. In this context, another attractive feature of mesoporous silica is its porosity, with high surface areas (up to $>1000 \text{ m}^2 \text{ g}^{-1}$) and large pore volumes (*circa* $1 \text{ cm}^3 \text{ g}^{-1}$) which can be attained with uniform porosity.^{47,51,52} This characteristic allows to load silica pores with large amounts of drugs or contrast agents and is also a reason why such materials are used in many other fields of research, such as catalysis^{53–55}, renewable energy^{56,57} or sensing^{58,59}. The pore diameter has some tunability range by varying the synthesis parameters. Moreover, therapeutic agents are protected from degradation and from being metabolized too fast by the silica matrix.⁶⁰ Sustained release of cargo can maintain its therapeutic levels in the body over extended periods of time, thus reducing the number of administration events. Lastly, the surface of silica is rich in silanol groups, which allow functionalization with a variety of chemical species, enabling the attachment of targeting ligands or additional therapeutic or diagnostic agents.

These unique features make MSNs excellent candidates for theranostic applications. Since the first report of a mesoporous silica material as a drug delivery system in 2001,⁶¹ mesoporous silica particles have been studied extensively as potential carriers of imaging and/or therapeutic moieties. An example of a multimodal MSN-based

theranostic agent is shown in Figure 1-2. In that study, dye-doped MSNs were decorated with multiple magnetite nanocrystals.⁶² The presence of superparamagnetic nanocrystals enabled the MSNs to be used as contrast agents in MRI, and the dye molecules added optical imaging modality. A large number of magnetic nanocrystals enhanced the MRI contrast. Additionally, an anticancer drug, doxorubicin (DOX), was loaded in the pores and induced cancer cell death. Accumulation of MSNs at tumor site was confirmed by both imaging modalities.

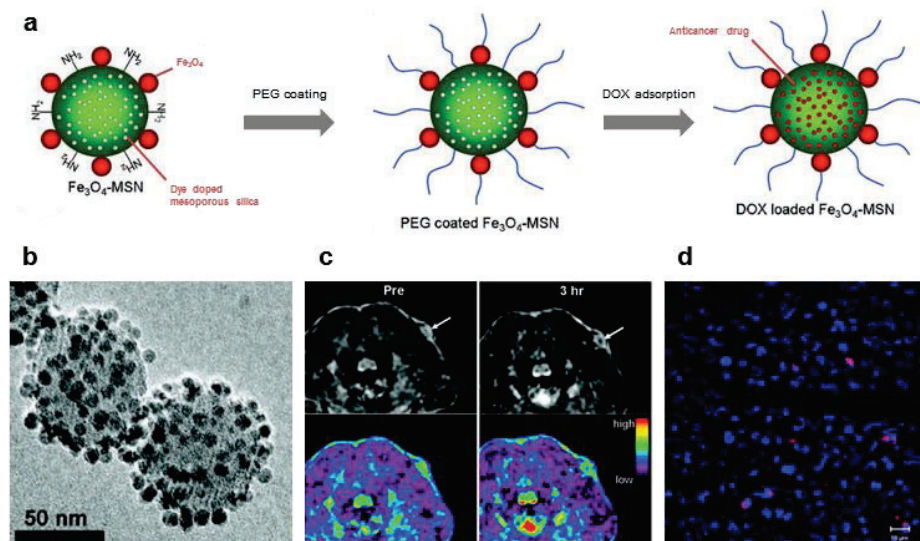


Figure 1-2. (a) Schematic illustration of the synthesis of multifunctional silica magnetic nanoparticles ($\text{Fe}_3\text{O}_4\text{-MSN}$).⁶² (b) TEM image of the particles. (c) *In vivo* T_2 -weighted MR images of the tumor site before and 3 h after intravenous injection of $\text{Fe}_3\text{O}_4\text{-MSN}$ (arrows indicating the tumor site). (d) Confocal laser scanning microscopic image of a section of tumor of a mouse after injection of DOX-loaded $\text{Fe}_3\text{O}_4\text{-MSN}$. Particle fluorescence (red) merged with DAPI-stained nuclei (blue). This figure is adapted from *J. Am. Chem. Soc.* (2010) by J. Lee et al.⁶²

Some of the recent mesoporous silica formulations are more complex, including particles with dynamic gates used to unload the cargo in a controllable way.^{47,63} MSNs capping systems have been designed to respond to chemical variations in the diseased site of the body (internal stimuli) such as the change of pH⁶⁴, dysregulation of enzymes⁶⁵, the presence of a specific pathogen⁶⁶ or changes in redox potential⁶⁷. Other systems were developed to release the cargo while triggered remotely by external stimuli: external magnetic fields⁶⁸, light⁶⁹ or ultrasounds⁷⁰. Although MSNs have not been approved for any clinical trials to date, large progress has been reported in the design and development of diagnostic and/or therapeutic MSN-based agents.⁴⁷

1.4. Shape and size of mesoporous silica particles

The vast majority of research on mesoporous silica materials for biomedical applications has been focused on spherical particles^{71,72} and not much attention was given to anisotropy, possibly due to the challenging fabrication of particles with well-controlled rod-like morphology. Some studies on mesoporous silica nanorods (MSNR) have been reported but they still represent an emerging field compared to the vast body of research on their spherical counterparts and the relevance of particle shape in nanomedicine remains largely unknown. Pioneering studies focused on rod-like particles have shown interesting results regarding their positive impact on therapeutic performance, including cell uptake, toxicity, degradation or drug release.^{73–81} In this context, it has been noted that these rod-shaped nanomaterials resemble biological entities such as certain types of bacteria (Figure 1-3), so that one might expect them to exhibit similar biobehavior.⁷⁵

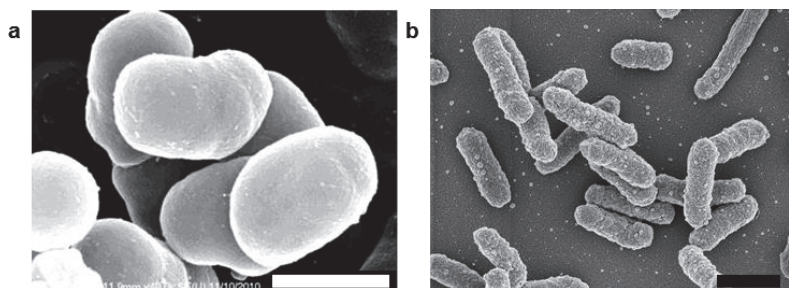


Figure 1-3. Rod-shaped bacteria. (a) *Acinetobacter baumannii*. SEM image obtained from *International Journal of Antimicrobial Agents* (2013) by M. Lai et al.⁸² (b) *Yersinia pestis*. SEM image obtained from M. Özel, G. Holland, R. Reissbrodt (*Robert Koch Institute*).⁸³ Scale bars: 1 μm .

Some studies have shown that elongated particles could be more efficient in therapeutic applications than their spherical counterparts, as suggested by their targeting specificity, biodistribution and cellular internalization.⁸⁴ The resemblance of rod-like particles to bacteria has been proposed as a potential reason for their superior internalization rate in non-phagocytic cells.⁸⁵ Similarly, in one study it was observed that silica rods exhibited higher diffusivity in intestinal mucus than spheres, leading to deeper mucus penetration and longer retention time in the gastrointestinal tract (Figure 1-4).⁸⁶ This behavior is analogous to that of rod-shaped pathogenic bacteria in the gastrointestinal tract, highly mobile in mucus.⁸⁷ Superior mucus diffusivity of silica rods has been explained by rotational dynamics facilitated by the fibrous structure of mucosal tissue and shear flow.

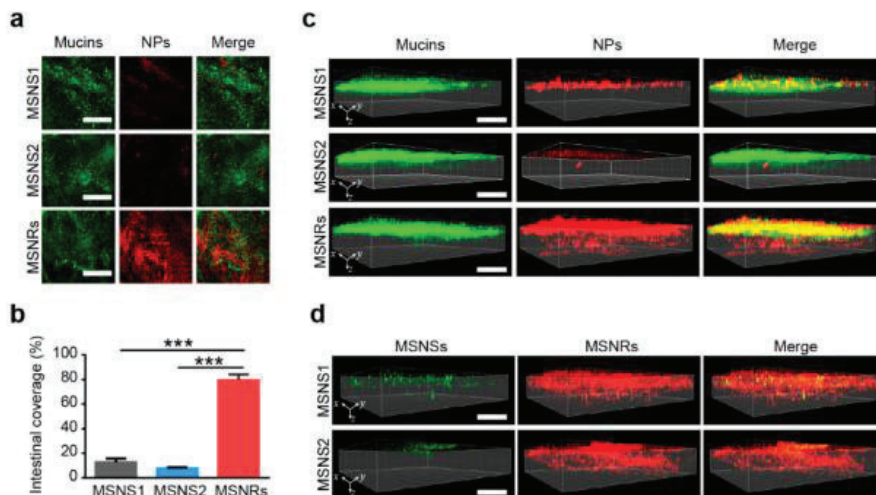


Figure 1-4. MSN distribution in rat intestinal mucus *ex vivo* – comparison of rods (MSNR) and spheres of two different sizes. (a) Two-dimensional coverage of NPs diffused in mucus. (b) Quantification of NP coverage in mucus in (a). (c) Three-dimensional images of mucus penetration. Mucus stained with Alexa Fluor 488-WGA (green) and NPs (red). (d) Comparison of penetration of MSNRs and MSNSs in the same mucus. MSNS1 or MSNS2 (green), and MSNRs (red). Images are representative of the averages. Scale bar: 50 μm . Depth: 40 μm . The data are presented as means \pm standard error means ($n \geq 3$). *** $P < 0.001$ compared to MSNS1 or MSNS2. This figure is obtained from *Nano Letters* (2016) by M. Yu et al.⁸⁶

MSNR are reported to be highly biocompatible materials^{74,88,89} but can lead to some biological toxicity when accumulated in large amounts.^{90,91} Therefore, silica particles with wider pore diameters and higher pore density have been used in various studies to achieve higher cargo loading capacity and minimize the amount of silica in the body. In one of the studies on *in vitro* toxicity, it was observed that mesoporous silica nanorods did not induce significant changes in Caco-2 cells compared to unexposed cells after incubation for 24 h at concentrations as high as 1 mg/ml, which indicates rather low toxicity.⁸⁸ In another study, no significant cell viability difference was found between HeLa cells treated with silica rods and spheres.⁷⁵ Other studies found cytotoxicity of silica rods at high concentrations on macrophages (RAW264.7), lung carcinoma cells, and hemolysis of human erythrocytes, albeit the toxicity levels were comparable to those of spheres.⁷⁴ These preliminary studies showed that the effect of particle shape on *in vitro* cytotoxicity may vary depending on cell origins and characteristics, culture medium, particle concentration, and incubation time.^{92,93} In contrast to the well-studied influence of particle size, surface chemistry and pore size on *in vivo* toxicity, the reports on the shape effects of mesoporous silica nanoparticles are very limited.

The intracellular delivery of theranostic agents depends critically on the uptake of carriers. Particle shape has been proven to be an important factor determining cellular

uptake.^{94,95} It has been suggested that mesoporous silica nanorods, unlike nanospheres, may enter cells either “side on” or “end on” and in this way the aspect ratio can influence the uptake pathway (Figure 1-5). A study on HeLa cells compared the internalization of mesoporous silica nanorods of different aspect ratios (ARs).⁸⁰ Interestingly, the uptake of rods with ARs of approximately 2.1 - 2.5 was higher compared to shorter (AR = 1.5 - 1.7) and longer (AR = 4.0 - 4.5) rods of the same width. In another study, mesoporous silica nanorods were more efficiently uptaken by Caco-2 cells than big or small nanospheres, indicating that the effect of particle shape was more significant than that of size.⁸⁸ It was also observed that the uptake efficiency of mesoporous silica rods varies for different cell types.^{73,80,81,88,92,96}

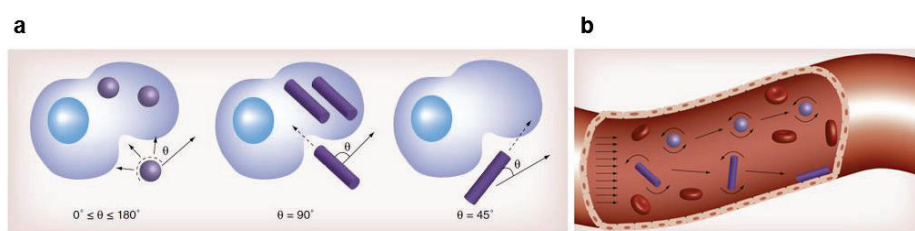


Figure 1-5. (a) Effect of particle shape on the internalization rate. Rod-shaped NPs are internalized the most quickly when their major axis is perpendicular to cell membrane. Internalization decreases with changing angle (θ) due to increased difficulty to “wrap” the particle. Spherical NPs are isotropic and internalized independently of θ . (b) Effect of shape on NP margination. Spherical NPs tend to remain at the center of the flow while forces and torques exerted on the rods under flow make them drift towards the vessel wall, where they are bound to receptors or extravasated through gaps between endothelial cells. This figure is adapted from *Nanomedicine (2014)* by R. Toy et al.⁹⁷

The particle shape can also affect their biodistribution. This effect has been already observed in carbon nanotubes characterized by a very high aspect ratio, which tend to accumulate preferentially in the liver and lungs after intravenous injection.⁹⁸ A study has shown that intravenously administered mesoporous silica nanorods were mainly present in the liver, spleen, and lung (>80%).⁷⁶ Rods with a low AR easily accumulated in the liver, while high AR rods were found in the spleen. Rod-like particles can be mainly excreted through urine and feces, and low AR particles were observed to have a more rapid clearance rate than high AR particles. A clear dependence of the aspect ratio of mesoporous silica rods on biodistribution has still not been fully determined due to the limited number of aspect ratio values that were considered in those studies.

Another biomedicine-related field where rod-like morphology could show superior performance compared to the spherical counterparts is the field of self-propelled nano- and microparticles. These active systems are inspired by the motion of biological organisms, and have found numerous applications in many fields,

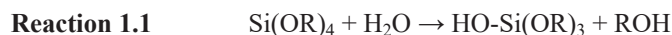
including biomedicine.⁹⁹ These systems convert the chemical energy from the environment into kinetic energy, leading to active motion. Due to the increasing need for versatile nanomotors with tunable properties, capable of hosting cargo or drugs, mesoporous silica has become an excellent candidate for such applications.^{100,101} Mesoporous silica motors powered by biochemical fuels such as glucose or urea have been reported and their potential for future use in biomedicine has been highlighted.¹⁰⁰ However, the systems studied for this purpose involved mostly spherical particles, and the influence of the particle anisotropy on the motion kinetics and directionality has not been given enough attention.

1.5. Synthesis of mesoporous silica nanoparticles

MSNs can be synthesized using a sol-gel process, which involves the transition of a colloidal suspension (sol) into an interconnected, rigid network (gel).¹⁰² MSN are generally prepared from alkoxy silanes (especially tetramethyl orthosilicate – TMOS or tetraethyl orthosilicate – TEOS) or silicates which serve as silica source.

A general procedure starts with the hydrolysis of the silica precursor.

Firstly, silicon alkoxides are hydrolysed in the presence of water and an acid or base catalyst (Reaction 1.1). Subsequently, condensation occurs between hydrolysed silica species and siloxane bonds (Si-O-Si) are created (Reactions 1.2 and 1.3):



Once there is a sufficient number of interconnected siloxane bonds in a particular region, colloidal particles are formed. The particles link together and grow into a three-dimensional silica network.

During the synthesis of MSNs, the silica structure is templated by supramolecular assemblies of surfactants. Examples include ionic or neutral surfactants, as well as block-copolymer surfactants such as alkyl polyethylene oxide and Pluronic tri-block copolymers which are widely employed due to their biocompatibility, non-toxicity and low cost.^{103,104} The surfactant is removed after the synthesis, commonly by pyrolysis or dissolution in an appropriate solvent, and empty pores are formed.

In 1998, ordered mesoporous silica SBA-15 with hexagonally arranged large cylindrical pores was synthesized using an amphiphilic triblock copolymer (poly(ethylene glycol)-block-poly(propylene glycol)-block-poly(ethylene glycol), Pluronic P123) as a structure-directing agent under acidic conditions.^{105,106} This occurs through a so-called Cooperative Templating Mechanism (CTM), by which the

material is formed in solution through self-assembly between a micellar surfactant and silica species coming from the silica precursor.¹⁰⁷ The most common morphologies of SBA-15 are wheat-like macrostructures aggregated by rope-like domains with sizes of approximately 1 μm .¹⁰⁵ SBA-15 is characterized by large adjustable pore size, thick walls and good stability.^{105,108–110}

Without an alkoxy silane in the solution, P123 forms spherical micelles. Upon addition of silica precursor under controlled temperature and stirring rate, cylindrical hybrid micelles which assemble into a hybrid organic/inorganic mesophase (Figure 1-6) can be formed.¹¹¹

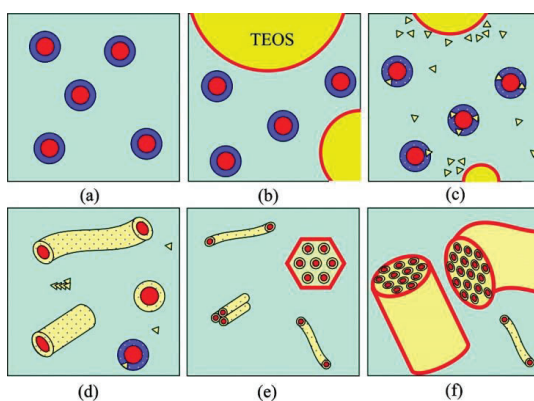


Figure 1-6. Sketch of different steps involved in mesoporous silica particles self-assembly. (a) Initial micellar solution of the surfactant. (b) Addition of silica precursor (TEOS). (c) Start of hydrolysis. (d) Shape evolution of the micelles. (e) Nucleation of the 2D-hexagonal phase. (f) Growth and precipitation of the 2D-hexagonal phase. This figure is obtained from *The Journal of Physical Chemistry B* (2011) by S. Manet et al.¹¹¹

The CTM route can be used to obtain (sub)micrometric particles of various morphologies which can be tuned by controlling synthesis parameters such as temperature or stirring rate, acidity, reaction duration, type of salt, co-solvent, co-surfactant, or introduction of organoalkoxysilane precursors.^{112–117} Such a method can lead to the formation of platelets, rice-like grains, hexagonal columns, rods of different aspect ratios or tori.¹¹⁸ A key step to obtain anisotropic SBA-15 particles was found to be stopping the solution stirring upon completion of TEOS hydrolysis.^{116,118} Following this step, the particles grow in static conditions (without stirring), which lets them reach equilibrium and slows down aggregation between particles.¹¹⁹

The addition of co-solvents, such as glycerol, decane, or 2,2,4-trimethylpentane (TMP) can also be effective in controlling the morphology but the use of excessive amounts could lead to a shift from the hexagonal mesostructure to different geometries.^{114,120} The addition of salt is another method of tuning the morphology and mesostructure of SBA-15 materials, which was also observed to facilitate the formation of ordered silicas at low temperature.^{112,115,121,122} For example, SBA-15 homogeneous rods and fibers can be synthesized from a reaction mixture consisting of sodium silicate and P123 under acidic conditions.^{103,123} In this configuration, sodium salts that are formed are important for determining the silica shape.

1.6. NAFLD - current diagnosis and treatment strategies

In this work, it has been hypothesized that mesoporous silica rods could be advantageous in targeting liver and in the future to be applied for addressing a current medical challenge, namely the early-stage diagnosis and therapy of non-alcoholic fatty liver disease (also known as NAFLD).

NAFLD is a major cause of liver disease worldwide, with a global prevalence of around 20-40%.¹²⁴⁻¹²⁶ Over the past three decades, lifestyle transformation has led to a steep increase in obesity, shifting NAFLD to an early onset in life.¹²⁷⁻¹²⁹ As a result, the prevalence of NAFLD in children and adolescents has risen considerably.¹²⁸ NAFLD starts with the accumulation of fat in hepatic cells and progresses in approximately 10-20% of cases to non-alcoholic steatohepatitis (NASH), characterized by hepatocellular steatosis, inflammation and fibrosis (Figure 1-7).¹³⁰ Liver fibrosis is characterized by the accumulation of extracellular matrix proteins such as collagen in the liver interstitial space.¹³¹ If untreated, it can develop to its endstage of cirrhosis, which poses a risk of developing into more severe and irreversible liver damage – hepatocellular carcinoma (HCC) and liver failure.¹³² Fibrosis is a dynamic and reversible process at its early stages and for this reason, it is important to be able to diagnose and treat NAFLD when the damage can still be reversed.

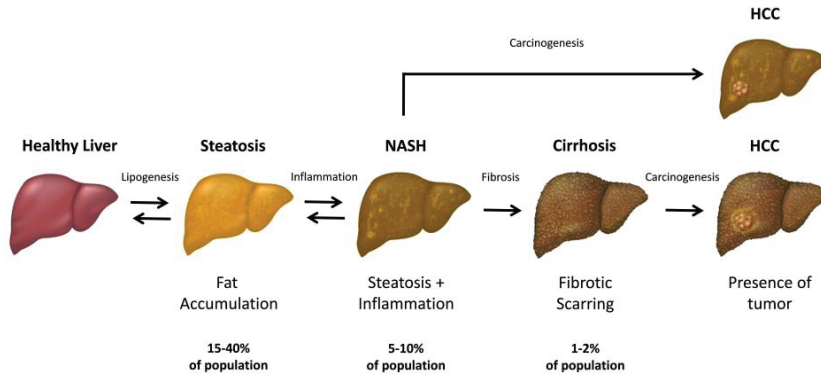


Figure 1-7. The progression of NAFLD. Steatosis (“fatty liver”) is the initial NAFLD stage and is characterized by excessive accumulation of fat in hepatic cells. Upon sustained inflammation, liver steatosis may develop to NASH, and subsequently, cirrhosis. NASH and cirrhotic liver have an increased chance to develop hepatocellular carcinoma (HCC). Steatosis and NASH are reversible, while cirrhotic tissue cannot be reversed to its healthy state. This figure is obtained from *Frontiers in Physiology* (2018) by A. Turchinovich et al.¹³³

The gold standard for diagnosing liver fibrosis is biopsy. However, it can lead to a sampling error as it only examines a small sample of the organ, has low patient acceptance, and low intra- and interobserver repeatability.^{134,135} Recently, efforts have been put in developing noninvasive techniques for the assessment of liver fibrosis. Various qualitative and quantitative imaging techniques offer the possibility of diagnosis, monitoring and staging of liver fibrosis and have been recently implemented on magnetic resonance imaging, ultrasound, or computed tomography.¹³⁶ These techniques allow studying changes in morphology or physical properties such as texture, mechanical properties, perfusion or hepatocellular function. The most commonly used liver fibrosis staging methods are US-based elastography techniques, including 1D transient elastography known in the clinical setting as Fibroscan.¹³⁶ Elastography techniques measure the mechanical shear wave propagation in the tissue. Liver fibrosis is associated with an exponential increase of liver stiffness that leads to an increase of the shear wave speed. Magnetic resonance-based elastography techniques have also been developed and studies have reported their higher diagnostic performance compared to US-based techniques.¹³⁷

To date, there is no established validated therapy for NAFLD/NASH due to an incomplete understanding of its underlying mechanisms. However, promising results have been obtained using various approaches. One strategy involves antisense therapy, where a single strand of RNA complementary to a specific mRNA (antisense oligonucleotide, ASO) can bind to it, inhibiting its expression.¹³⁸ Studies identified serine/threonine protein kinase Stk25, a member of the sterile 20 kinase superfamily, as a critical regulator of NAFLD.¹³⁹ Stk25 antisense oligonucleotide has been conjugated with N-acetyl galactosamine (GalNAc) moiety to selectively target

asialoglycoprotein receptors (ASGPR), abundantly expressed on hepatocytes.¹⁴⁰ A treatment of obese mice with GalNAc-Stk25 ASO efficiently ameliorated hepatic steatosis, inflammation and fibrosis.¹⁴¹

Another candidate with great potential for the treatment of NAFLD that has been studied recently are cerium oxide nanoparticles (CeO₂NPs).^{142,143} CeO₂NPs exhibit antioxidant properties due to the self-regeneration of their surface, which is based on redox-cycling between Ce³⁺ and Ce⁴⁺ states.^{144,145} The capacity of nanoceria to modify its oxidation state depending on its surroundings makes it appealing in biomedicine.^{146,147} In situations of reactive oxygen species (ROS) imbalance, the oxygen storage capacity of ceria lets it remove free radicals, thus protecting cells from several forms of lethal stress such as chronic inflammation or lipid peroxidation.^{148,149} It has been hypothesized that ceria could exhibit hepatoprotective properties *in vivo* against cellular damage owing to its passive accumulation in the liver and the capacity to degrade free radicals.¹⁴² Indeed, it was observed that intravenous administration of ceria NPs in CCl₄-treated rats prevented chronic liver injury.¹⁴² Ceria interferes with the pro-inflammatory signaling activation occurring in chronically injured liver. A similar effect has been previously induced by vitamin C or superoxide dismutase, but the advantage of CeO₂ over these compounds is that it can work without being consumed.¹⁴² It has been shown that CeO₂NPs significantly reduced hepatic steatosis, ameliorated pro-inflammatory cytokines and attenuated the intensity of the inflammatory response, indicating their therapeutic value against NAFLD.¹⁴² Recently, the *in vivo* use of CeO₂NPs coated with mesoporous silica has been reported.¹⁵⁰ The silica coating increased the stability of the CeO₂NPs in the physiological media, maximized their ROS scavenging activity, and minimized their non-hepatic distribution.

1.7. Objectives of the thesis

Since silica rods were found to show increased penetration in a fibrous tissue compared to their spherical counterparts⁸⁶, it is hypothesized in this thesis that similar behavior could be observed with mesoporous silica rods in fibrous liver tissue. Moreover, as a high accumulation in the liver is also expected, silica nanorod-based systems will be designed to take advantage of these phenomena and will be modified to act as a potential agent for multimodal liver imaging and eventually useful for the diagnosis and treatment of NAFLD.

In this context, the **overall aim of the thesis is to explore the suitability of mesoporous silica rods (MSRs) in terms of synthesis versatility, biocompatibility, biodistribution and theranostic potential for further studies to engage in more advanced models of fatty liver.**

The specific objectives are:

- **The synthesis of rods with well-defined size and two distinct aspect ratios** to be compared as potential theranostic agents in terms of their function, uptake and biocompatibility.
- **Endowing the mesoporous silica nanorods with different functional imaging modalities, therapeutic capabilities, and self-propulsion.**
- **Studying the toxicity of these rods, their biodistribution and their uptake by liver cells.**
- **Evaluating the biodistribution of the rods in-vivo in preclinical models.**

1.8. Chapter references

1. Lammers, T. & Ferrari, M. The success of nanomedicine. *Nano Today* **31**, 100853 (2020).
2. Mitchell, M. J. *et al.* Engineering precision nanoparticles. *Nat. Rev. Drug Discov.* **20**, 101–124 (2021).
3. Chan, W. C. W. Nanomedicine 2.0. *Acc. Chem. Res.* **50**, 627–632 (2017).
4. Baig, N., Kammakam, I. & Falath, W. Nanomaterials: A review of synthesis methods, properties, recent progress, and challenges. *Mater. Adv.* **2**, 1821–1871 (2021).
5. Bulte, J. W. M. & Modo, M. M. J. *Design and Applications of Nanoparticles in Biomedical Imaging*. (Springer International Publishing, 2017).
6. Dreifuss, T. *et al.* A challenge for theranostics: is the optimal particle for therapy also optimal for diagnostics? *Nanoscale* **7**, 15175–15184 (2015).
7. Nam, J.-M., Thaxton, C. S. & Mirkin, C. A. Nanoparticle-Based Bio-Bar Codes for the Ultrasensitive Detection of Proteins. **301**, 1884–1887 (2003).
8. Shehada, N. *et al.* Silicon Nanowire Sensors Enable Diagnosis of Patients via Exhaled Breath. *ACS Nano* **10**, 7047–7057 (2016).
9. Chen, K. *et al.* Applications and regulatory of nanotechnology-based innovative in vitro diagnostics. *VIEW* **2**, (2021).
10. Nelson, B. C., Minelli, C., Doak, S. H. & Roesslein, M. Emerging Standards and Analytical Science for Nanoenabled Medical Products. *Annu Rev Anal Chem (Palo Alto Calif)*. **13**, 431–452 (2020).
11. Smith, B. R. & Gambhir, S. S. Nanomaterials for in Vivo Imaging. *Chem. Rev.* **117**, 901–986 (2017).
12. Khurana, A. *et al.* Role of nanotechnology behind the success of mRNA vaccines for COVID-19. *Nano Today* **38**, 101142 (2021).
13. Tang, Z. *et al.* Insights from nanotechnology in COVID-19 treatment. *Nano Today* **36**, (2021).
14. Singh, D., Dilnawaz, F. & Sahoo, S. K. Challenges of moving theranostic nanomedicine into the clinic. *Nanomedicine (Lond.)* **15**, 111–114 (2020).
15. Blanco, E., Shen, H. & Ferrari, M. Principles of nanoparticle design for overcoming biological barriers to drug delivery. *Nat. Biotechnol.* **33**, 941–951 (2015).
16. Albanese, A., Tang, P. S. & Chan, W. C. W. The Effect of Nanoparticle Size, Shape, and Surface Chemistry on Biological Systems. *Annu. Rev. Biomed. Eng.* **14**, 1–16 (2012).
17. Nel, A. E. *et al.* Understanding biophysicochemical interactions at the nano–bio interface. *Nat. Mater.* **8**, 543–557 (2009).
18. Cheng, L.-C., Jiang, X., Wang, J., Chen, C. & Liu, R.-S. Nano–bio effects: interaction of nanomaterials with cells. *Nanoscale* **5**, 3547 (2013).
19. Lee, D.-E. *et al.* Multifunctional nanoparticles for multimodal imaging and theragnosis. *Chem. Soc. Rev.* **41**, 2656–2672 (2012).
20. Lee, S. Y., Jeon, S. I., Jung, S., Chung, I. J. & Ahn, C.-H. Targeted multimodal imaging modalities. *Adv. Drug Deliv. Rev.* **76**, 60–78 (2014).
21. Rieffel, J., Chitgupi, U. & Lovell, J. F. Recent Advances in Higher-Order, Multimodal, Biomedical Imaging Agents. *Small* **11**, 4445–4461 (2015).
22. Key, J. & Leary, J. F. Nanoparticles for multimodal in vivo imaging in nanomedicine.

- Int. J. Nanomedicine* **9**, 711–726 (2014).
23. Cole, J. T. & Holland, N. B. Multifunctional nanoparticles for use in theranostic applications. *Drug Deliv. Transl. Res.* **5**, 295–309 (2015).
 24. Silva, A. K. A., Espinosa, A., Kolosnjaj-Tabi, J., Wilhelm, C. & Gazeau, F. Medical Applications of Iron Oxide Nanoparticles. in *Iron Oxides: From Nature to Applications* 425–471 (Wiley-VCH Verlag GmbH & Co. KGaA, 2016).
 25. Taboada, E. *et al.* Relaxometric and Magnetic Characterization of Ultrasmall Iron Oxide Nanoparticles with High Magnetization. Evaluation as Potential T1 Magnetic Resonance Imaging Contrast Agents for Molecular Imaging. *Langmuir* **23**, 4583–4588 (2007).
 26. Taboada, E., Solanas, R., Rodríguez, E., Weissleder, R. & Roig, A. Supercritical-Fluid-Assisted One-Pot Synthesis of Biocompatible Core(γ -Fe₂O₃)/Shell(SiO₂) Nanoparticles as High Relaxivity T₂-Contrast Agents for Magnetic Resonance Imaging. *Adv. Funct. Mater.* **19**, 2319–2324 (2009).
 27. Weissleder, R. Scaling down imaging: molecular mapping of cancer in mice. *Nature Reviews Cancer* **2**, 11–8 (2002).
 28. Cormode, D. P., Skajaa, T., Fayad, Z. A. & Mulder, W. J. M. Nanotechnology in Medical Imaging: Probe Design and Applications. *Arterioscler. Thromb. Vasc. Biol.* **29**, 992–1000 (2009).
 29. Hasebroock, K. M. & Serkova, N. J. Toxicity of MRI and CT contrast agents. *Expert Opin. Drug Metab. Toxicol.* **5**, 403–416 (2009).
 30. Massoud, T. F. & Gambhir, S. S. Molecular imaging in living subjects: seeing fundamental biological processes in a new light. *Genes Dev.* **17**, 545–580 (2003).
 31. Blomley, M. J. K., Cooke, J. C., Unger, E. C., Monaghan, M. J. & Cosgrove, D. O. Microbubble contrast agents: a new era in ultrasound. *BMJ* **322**, 1222 (2001).
 32. Sheeran, P. S., Luo, S. H., Mullin, L. B., Matsunaga, T. O. & Dayton, P. A. Design of ultrasonically-activatable nanoparticles using low boiling point perfluorocarbons. *Biomaterials* **33**, 3262–3269 (2012).
 33. An, L. *et al.* Paramagnetic hollow silica nanospheres for in vivo targeted ultrasound and magnetic resonance imaging. *Biomaterials* **35**, 5381–5392 (2014).
 34. Yin, T. *et al.* Ultrasound-sensitive siRNA-loaded nanobubbles formed by hetero-assembly of polymeric micelles and liposomes and their therapeutic effect in gliomas. *Biomaterials* **34**, 4532–4543 (2013).
 35. Yang, F. *et al.* Superparamagnetic iron oxide nanoparticle-embedded encapsulated microbubbles as dual contrast agents of magnetic resonance and ultrasound imaging. *Biomaterials* **30**, 3882–3890 (2009).
 36. Schutt, E. G., Klein, D. H., Mattrey, R. M. & Riess, J. G. Injectable microbubbles as contrast agents for diagnostic ultrasound imaging: The key role of perfluorochemicals. *Angewandte Chemie - International Edition* **42**, 3218–3235 (2003).
 37. Yildirim, A., Chattaraj, R., Blum, N. T., Goldscheitter, G. M. & Goodwin, A. P. Stable Encapsulation of Air in Mesoporous Silica Nanoparticles: Fluorocarbon-Free Nanoscale Ultrasound Contrast Agents. *Adv. Healthc. Mater.* **5**, 1290–1298 (2016).
 38. Janib, S. M., Moses, A. S. & Mackay, J. A. Imaging and drug delivery using theranostic nanoparticles. *Adv. Drug Deliv. Rev.* **62**, 1052–1063 (2010).
 39. Cao, J. *et al.* Recent Progress in NIR-II Contrast Agent for Biological Imaging. *Front. Bioeng. Biotechnol.* **7**, (2020).
 40. Jennings, L. E. & Long, N. J. ‘Two is better than one’—probes for dual-modality

- molecular imaging. *Chem. Commun.* 3511–3524 (2009).
41. Park, K. *et al.* New Generation of Multifunctional Nanoparticles for Cancer Imaging and Therapy. *Adv. Funct. Mater.* **19**, 1553–1566 (2009).
 42. Kim, J., Piao, Y. & Hyeon, T. Multifunctional nanostructured materials for multimodal imaging, and simultaneous imaging and therapy. *Chem. Soc. Rev.* **38**, 372–390 (2009).
 43. Giri, S., Trewyn, B. G. & Lin, V. S. Y. Mesoporous silica nanomaterial-based biotechnological and biomedical delivery systems. *Nanomedicine (Lond.)* **2**, 99–111 (2007).
 44. Vallet-Regí, M., Balas, F. & Arcos, D. Mesoporous materials for drug delivery. *Angewandte Chemie - International Edition* **46**, 7548–7558 (2007).
 45. Slowing, I. I., Trewyn, B. G., Giri, S. & Lin, V. S.-Y. Mesoporous silica nanoparticles for drug delivery and biosensing applications. *Adv. Funct. Mater.* **17**, 1225–1236 (2007).
 46. Vivero-Escoto, J. L., Slowing, I. I., Lin, V. S.-Y. & Trewyn, B. G. Mesoporous Silica Nanoparticles for Intracellular Controlled Drug Delivery. *Small* **6**, 1952–1967 (2010).
 47. Manzano, M. & Vallet-Regí, M. Mesoporous Silica Nanoparticles for Drug Delivery. *Adv. Funct. Mater.* **30**, 3–5 (2020).
 48. Narayan, R., Nayak, U. Y., Raichur, A. M. & Garg, S. Mesoporous silica nanoparticles: A comprehensive review on synthesis and recent advances. *Pharmaceutics* **10**, 1–49 (2018).
 49. Descalzo, A. B., Martínez-Mañez, R., Sancenón, F., Hoffmann, K. & Rurack, K. The supramolecular chemistry of organic-inorganic hybrid materials. *Angew. Chem. Int. Ed. Engl.* **45**, 5924–5948 (2006).
 50. Trewyn, B. G., Slowing, I. I., Giri, S., Chen, H. & Lin, V. S. Synthesis and Functionalization of a Mesoporous Silica Nanoparticle Based on the Sol-Gel Process and Applications in Controlled Release. *Acc. Chem. Res.* **40**, 846–853 (2007).
 51. Yanagisawa, T., Shimizu, T., Kuroda, K. & Kato, C. The Preparation of Alkyltrimethylammonium–Kanemite Complexes and Their Conversion to Microporous Materials. *Bull. Chem. Soc. Jpn.* **63**, 988–992 (1990).
 52. Kresge C.T., Leonowicz M.E., Roth W.J., Vartuli J.C. & Beck J.S. Ordered mesoporous molecular sieves synthesized by a liquid-crystal template mechanism. *Nature* **359**, 710–712 (1992).
 53. Stein, A., Melde, B. J. & Schroden, R. C. Hybrid Inorganic–Organic Mesoporous Silicates—Nanoscopic Reactors Coming of Age. *Adv. Mater.* **12**, 1403–1419 (2000).
 54. Huh, S., Chen, H. T., Wiench, J. W., Pruski, M. & Lin, V. S. Y. Cooperative Catalysis by General Acid and Base Bifunctionalized Mesoporous Silica Nanospheres. *Angew. Chemie - Int. Ed.* **44**, 1826–1830 (2005).
 55. Kon'kova, T. V., Gordienko, M. G., Alekhina, M. B., Men'shutina, N. V & Kirik, S. D. Mesoporous silica based catalysts for the oxidation of azodyes in waste water. *Catal. Ind.* **8**, 128–133 (2016).
 56. Florek, J., Giret, S., Juère, E., Larivière, D. & Kleitz, F. Functionalization of mesoporous materials for lanthanide and actinide extraction. *Dalton Transactions* **45**, 14832–14854 (2016).
 57. Yang, X. *et al.* Synthesis of mesoporous silica from coal slag and CO₂ for phenol removal. *J. Clean. Prod.* **208**, 1255–1264 (2019).
 58. Tan, S. Y. *et al.* Responsive mesoporous silica nanoparticles for sensing of hydrogen peroxide and simultaneous treatment toward heart failure. *Nanoscale* **9**, 2253–2261

- (2017).
59. Das, T., Singha, D., Pal, A. & Nandi, M. Mesoporous silica based recyclable probe for colorimetric detection and separation of ppb level Hg²⁺ from aqueous medium. *Sci. Rep.* **9**, 19378 (2019).
 60. Park, J. H. *et al.* Biodegradable luminescent porous silicon nanoparticles for in vivo applications. *Nat. Mater.* **8**, 331–336 (2009).
 61. Vallet-Regí, M., Rámila, A., Del Real, R. P. & Pérez-Pariente, J. A new property of MCM-41: Drug delivery system. *Chem. Mater.* **13**, 308–311 (2001).
 62. Lee, J. E. *et al.* Uniform Mesoporous Dye-Doped Silica Nanoparticles Decorated with Multiple Magnetite Nanocrystals for Simultaneous Enhanced Magnetic Resonance Imaging, Fluorescence Imaging, and Drug Delivery. *J. Am. Chem. Soc.* **132**, 552–557 (2010).
 63. Aznar, E. *et al.* Gated Materials for On-Command Release of Guest Molecules. *Chem. Rev.* **116**, 561–718 (2016).
 64. Martínez-Carmona, M., Lozano, D., Colilla, M. & Vallet-Regí, M. Lectin-conjugated pH-responsive mesoporous silica nanoparticles for targeted bone cancer treatment. *Acta Biomater.* **65**, 393–404 (2018).
 65. Kumar, B., Kulanthaivel, S., Mondal, A. & Mishra, S. Mesoporous silica nanoparticle based enzyme responsive system for colon specific drug delivery through guar gum capping. *Colloids Surfaces B Biointerfaces* **150**, 352–361 (2017).
 66. Ruehle, B., Clemens, D. L., Lee, B., Horwitz, M. A. & Zink, J. I. A Pathogen-Specific Cargo Delivery Platform Based on Mesoporous Silica Nanoparticles. *J. Am. Chem. Soc.* **139**, 6663–6668 (2017).
 67. Lee, B.-Y. *et al.* Redox-Triggered Release of Moxifloxacin from Mesoporous Silica Nanoparticles Functionalized with Disulfide Snap-Tops Enhances Efficacy Against Pneumonic Tularemia in Mice. *Small* **12**, 3690–3702 (2016).
 68. Rühle, B., Datz, S., Argyo, C., Bein, T. & Zink, J. I. A molecular nanocap activated by superparamagnetic heating for externally stimulated cargo release. *Chem. Commun.* **52**, 1843 (2016).
 69. Wang, D. & Wu, S. Red-Light-Responsive Supramolecular Valves for Photocontrolled Drug Release from Mesoporous Nanoparticles. *Langmuir* **2016**, 632–636 (2016).
 70. Paris, J. L., Manzano, M., Cabañas, M. V. & Vallet-Regí, M. Mesoporous silica nanoparticles engineered for ultrasound-induced uptake by cancer cells. *Nanoscale* **10**, 6402 (2018).
 71. Du, X. & He, J. Spherical silica micro/nanomaterials with hierarchical structures: Synthesis and applications. *Nanoscale* **3**, 3984–4002 (2011).
 72. Shiba, K., Shimura, N. & Ogawa, M. Mesoporous silica spherical particles. *Journal of Nanoscience and Nanotechnology* **13**, 2483–94 (2013).
 73. Huang, X., Teng, X., Chen, D., Tang, F. & He, J. The effect of the shape of mesoporous silica nanoparticles on cellular uptake and cell function. *Biomaterials* **31**, 438–448 (2010).
 74. Yu, T., Malugin, A. & Ghandehari, H. Impact of Silica Nanoparticle Design on Cellular Toxicity and Hemolytic Activity. *ACS Nano* **5**, 5717–5728 (2011).
 75. Karaman, D. Sen *et al.* Shape engineering vs organic modification of inorganic nanoparticles as a tool for enhancing cellular internalization. *Nanoscale Res. Lett.* **7**, (2012).

76. Huang, X. *et al.* The shape effect of mesoporous silica nanoparticles on biodistribution, clearance, and biocompatibility in vivo. *ACS Nano* **5**, 5390–5399 (2011).
77. Li, L. *et al.* Biodistribution, excretion, and toxicity of mesoporous silica nanoparticles after oral administration depend on their shape. *Nanomedicine Nanotechnology, Biol. Med.* **11**, 1915–1924 (2015).
78. Vácha, R., Martínez-Veracoechea, F. J. & Frenkel, D. Receptor-Mediated Endocytosis of Nanoparticles of Various Shapes. *Nano Lett.* **11**, 5391–5395 (2011).
79. Trewyn, B. G., Nieweg, J. A., Zhao, Y. & Lin, V. S.-Y. Biocompatible mesoporous silica nanoparticles with different morphologies for animal cell membrane penetration. *Chem. Eng. J.* **137**, 23–29 (2008).
80. Meng, H. *et al.* Aspect Ratio Determines the Quantity of Mesoporous Silica Nanoparticle Uptake by a Small GTPase-Dependent Macropinocytosis Mechanism. *ACS Nano* **5**, 4434–4447 (2011).
81. Hao, N. *et al.* The shape effect of PEGylated mesoporous silica nanoparticles on cellular uptake pathway in Hela cells. *Microporous Mesoporous Mater.* **162**, 14–23 (2012).
82. Lai, M. J. *et al.* Identification and characterisation of the putative phage-related endolysins through full genome sequence analysis in *Acinetobacter baumannii* ATCC 17978. *Int. J. Antimicrob. Agents* **42**, 141–148 (2013).
83. Özel, M., Holland, G. & Reissbrodt, R. *Yersinia pestis*, colony. Scanning electron microscopy.
84. Venkataraman, S. *et al.* The effects of polymeric nanostructure shape on drug delivery. *Adv. Drug Deliv. Rev.* **63**, 1228–1246 (2011).
85. Gratton, S. E. A. *et al.* The effect of particle design on cellular internalization pathways. *PNAS* **105**, 11613–11618 (2008).
86. Yu, M. *et al.* Rotation-Facilitated Rapid Transport of Nanorods in Mucosal Tissues. *Nano Lett.* **16**, 7176–7182 (2016).
87. Sycuro, L. K. *et al.* Peptidoglycan crosslinking relaxation promotes *Helicobacter pylori*'s helical shape and stomach colonization. *Cell* **141**, 822–33 (2010).
88. Zheng, N. *et al.* Mesoporous silica nanorods for improved oral drug absorption. *Artif Cells Nanomed Biotechnol.* **46**, 1132–1140 (2018).
89. Zhao, Y. *et al.* A comparison between sphere and rod nanoparticles regarding their in vivo biological behavior and pharmacokinetics. *Sci. Rep.* **7**, 4131 (2017).
90. Hu, J.-J., Xiao, D. & Zhang, X.-Z. Advances in Peptide Functionalization on Mesoporous Silica Nanoparticles for Controlled Drug Release. *Small* **12**, 3344–3359 (2016).
91. Yang, Y. *et al.* Understanding the Effect of Surface Chemistry of Mesoporous Silica Nanorods on Their Vaccine Adjuvant Potency. *Adv. Heal. Mater.* **6**, (2017).
92. Hao, N., Yang, H., Li, L., Li, L. & Tang, F. The shape effect of mesoporous silica nanoparticles on intracellular reactive oxygen species in A375 cells. *New J. Chem.* **38**, 4258–4266 (2014).
93. Slowing, I. I. *et al.* Exocytosis of Mesoporous Silica Nanoparticles from Mammalian Cells: From Asymmetric Cell-to-Cell Transfer to Protein Harvesting. *Small* **7**, 1526–1532 (2011).
94. Geng, Y. *et al.* Shape effects of filaments versus spherical particles in flow and drug delivery. *Nat. Nanotechnol.* **2**, 249–255 (2007).

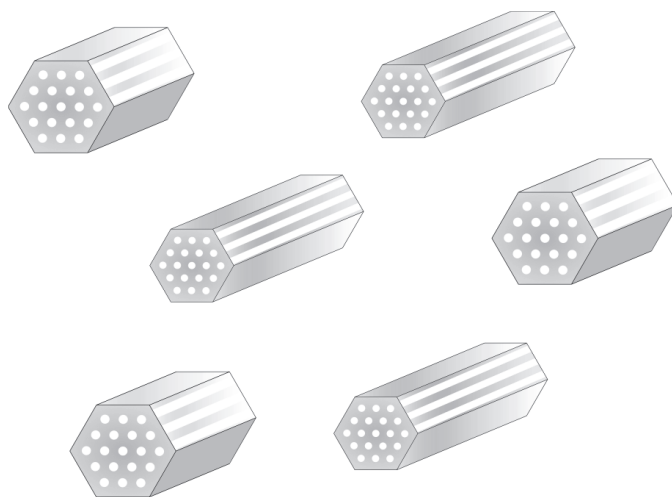
95. Champion, J. A. & Mitragotri, S. Role of target geometry in phagocytosis. *PNAS* **103**, 4930–4934 (2006).
96. Yang, X. *et al.* Synthesis of Hollow Mesoporous Silica Nanorods with Controllable Aspect Ratios for Intracellular Triggered Drug Release in Cancer Cells. *ACS Appl. Mater. Interfaces* **8**, 20558–20569 (2016).
97. Toy, R., Peiris, P. M., Ghaghada, K. B. & Karathanasis, E. Shaping cancer nanomedicine: the effect of particle shape on the in vivo journey of nanoparticles. *Nanomedicine (Lond.)* **9**, 121–134 (2014).
98. Jacobsen, N. R. *et al.* Biodistribution of Carbon Nanotubes in Animal Models. *Basic Clin. Pharmacol. Toxicol.* **121**, 30–43 (2017).
99. Patiño, T., Arqué, X., Mestre, R., Palacios, L. & Sánchez, S. Fundamental Aspects of Enzyme-Powered Micro- and Nanoswimmers. *Acc. Chem. Res.* **51**, 2662–2671 (2018).
100. Ma, X. *et al.* Mesoporous silica as micro/nano-carrier: From passive to active cargo delivery, a mini review. *J. Mater. Sci. Technol.* **33**, 1067–1074 (2017).
101. Xuan, M. *et al.* Near Infrared Light-Powered Janus Mesoporous Silica Nanoparticle Motors. *J. Am. Chem. Soc.* **138**, 6492–6497 (2016).
102. Singh, L. P. *et al.* Sol-Gel processing of silica nanoparticles and their applications. *Adv. Colloid Interface Sci.* **214**, 17–37 (2014).
103. Chao, M. C., Chang, C. H., Lin, H. P., Tang, C. Y. & Lin, C. Y. Morphological control on SBA-15 mesoporous silicas via a slow self-assembling rate. *J. Mater. Sci.* **44**, 6453–6462 (2009).
104. Hao, N. *et al.* Shape control of mesoporous silica nanomaterials templated with dual cationic surfactants and their antibacterial activities. *Biomater. Sci.* **4**, 87 (2016).
105. Zhao, D. *et al.* Triblock Copolymer Syntheses of Mesoporous Silica with Periodic 50 to 300 Angstrom Pores. *Science* **279**, 548–552 (1998).
106. Zhao, D., Huo, Q., Feng, J., Chmelka, B. F. & Stucky, G. D. Nonionic Triblock and Star Diblock Copolymer and Oligomeric Surfactant Syntheses of Highly Ordered, Hydrothermally Stable, Mesoporous Silica Structures. *J. Am. Chem. Soc.* **120**, 6024–6036 (1998).
107. Blin, J. L. & Impéror-Clerc, M. Mechanism of self-assembly in the synthesis of silica mesoporous materials: in situ studies by X-ray and neutron scattering. *Chem. Soc. Rev.* **42**, 4071–4082 (2013).
108. Kruk, M. & Jaroniec, M. Characterization of the Porous Structure of SBA-15. *Chem. Mater.* **12**, 1961–1968 (2000).
109. Impéror-Clerc, M., Davidson, P. & Davidson, A. Existence of a Microporous Corona around the Mesopores of Silica-Based SBA-15 Materials Templated by Triblock Copolymers. *J. Am. Chem. Soc.* **122**, 11925–11933 (2000).
110. Galarneau, A., Cambon, H., Di Renzo, F. & Fajula, F. True Microporosity and Surface Area of Mesoporous SBA-15 Silicas as a Function of Synthesis Temperature. *Langmuir* **17**, 8328–8335 (2001).
111. Manet, S. *et al.* Kinetics of the Formation of 2D-Hexagonal Silica Nanostructured Materials by Nonionic Block Copolymer Templating in Solution. *J. Phys. Chem. B* **115**, 11330–11344 (2011).
112. Zhao, D., Sun, J., Li, Q. & Stucky, G. D. Morphological Control of Highly Ordered Mesoporous Silica SBA-15. *Chem. Mater.* **12**, 275–279 (2000).
113. Yu, C., Fan, J., Tian, B. & Zhao, D. Morphology Development of Mesoporous

- Materials: a Colloidal Phase Separation Mechanism. *Chem. Mater.* **16**, 889–898 (2004).
114. Liu, J., Li, C., Yang, Q., Yang, J. & Li, C. Morphological and Structural Evolution of Mesoporous Silicas in a Mild Buffer Solution and Lysozyme Adsorption. *Langmuir* **23**, 7255–7262 (2007).
 115. Kubo, S. & Kosuge, K. Salt-Induced Formation of Uniform Fiberlike SBA-15 Mesoporous Silica Particles and Application to Toluene Adsorption. *Langmuir* **23**, 11761–11768 (2007).
 116. Sayari, A., Han, B. H. & Yang, Y. Simple Synthesis Route to Monodispersed SBA-15 Silica Rods. *J. Am. Chem. Soc.* **126**, 14348–14349 (2004).
 117. Sujandi *et al.* Amino-functionalized SBA-15 type mesoporous silica having nanostructured hexagonal platelet morphology. *Chem. Commun.* 4131–4133 (2006).
 118. Lee, H. I. *et al.* Morphology-selective synthesis of mesoporous SBA-15 particles over micrometer, submicrometer and nanometer scales. *J. Mater. Chem.* **20**, 8483–8487 (2010).
 119. Moulin, R., Schmitt, J., Lecchi, A., Degrouard, J. & Imp  rator-Clerc, M. Morphologies of mesoporous SBA-15 particles explained by the competition between interfacial and bending energies. *Soft Matter* **9**, 11085 (2013).
 120. Zhang, H. *et al.* Unusual Mesoporous SBA-15 with Parallel Channels Running along the Short Axis. *J. Am. Chem. Soc.* **126**, 7440–7441 (2004).
 121. Wan, Y., Shi, Y. & Zhao, D. Supramolecular Aggregates as Templates: Ordered Mesoporous Polymers and Carbons. *Chem. Mater.* **20**, 932–945 (2008).
 122. Yu, C., Tian, B., Fan, J., Stucky, G. D. & Zhao, D. Salt effect in the synthesis of mesoporous silica templated by non-ionic block copolymers. *Chem. Commun.* 2726–2727 (2001).
 123. Kosuge, K., Sato, T., Kikukawa, N. & Takemori, M. Morphological Control of Rod- and Fiberlike SBA-15 Type Mesoporous Silica Using Water-Soluble Sodium Silicate. *Chem. Mater.* **16**, 899–905 (2004).
 124. Younossi, Z. *et al.* Global Epidemiology of Nonalcoholic Fatty Liver Disease—Meta-Analytic Assessment of Prevalence, Incidence, and Outcomes. *Hepatology* **64**, (2016).
 125. Sanyal, A. J. Past, present and future perspectives in nonalcoholic fatty liver disease. *Nat. Rev. Gastroenterol. Hepatol.* **16**, 377–386 (2019).
 126. Ferguson, D. & Finck, B. N. Emerging therapeutic approaches for the treatment of NAFLD and type 2 diabetes mellitus. *Nat. Rev. Endocrinol.* **17**, 484–495 (2021).
 127. Pimpin, L. *et al.* Burden of liver disease in Europe : Epidemiology and analysis of risk factors to identify prevention policies. *J. Hepatol.* **69**, 718–735 (2018).
 128. Zhang, X. *et al.* Increasing prevalence of NAFLD/NASH among children, adolescents and young adults from 1990 to 2017: a population-based observational study. *BMJ Open* **11**, (2021).
 129. Goldner, D. & Lavine, J. E. Nonalcoholic Fatty Liver Disease in Children: Unique Considerations and Challenges. *Gastroenterology* **158**, 1967–1983 (2020).
 130. Wree, A., Broderick, L., Canbay, A., Hoffman, H. M. & Feldstein, A. E. From NAFLD to NASH to cirrhosis—new insights into disease mechanisms. *Nat. Rev. Gastroenterol. Hepatol.* **10**, 627–636 (2013).
 131. Bataller, R. & Brenner, D. a. Liver fibrosis. *J. Clin. Invest.* **115**, 209–218 (2005).
 132. Gariani, K. *et al.* Inhibiting poly ADP-ribosylation increases fatty acid oxidation and protects against fatty liver disease. *J. Hepatol.* **66**, 132–141 (2017).

133. Turchinovich, A., Baranova, A., Drapkina, O., Prince, R. & Hospital, A. Cell-Free Circulating Nucleic Acids as Early Biomarkers for NAFLD and NAFLD-Associated Disorders. *Front. Physiol.* **9**, 1256 (2018).
134. Rockey, D. C., Caldwell, S. H., Goodman, Z. D., Nelson, R. C. & Smith, A. D. Liver biopsy. *Hepatology* **49**, 1017–1044 (2009).
135. Bedossa, P. & Carrat, F. Liver biopsy: The best, not the gold standard. *J. Hepatol.* **50**, 1–3 (2009).
136. Petitclerc, L., Sebastiani, G., Gilbert, G., Cloutier, G. & Tang, A. Liver Fibrosis: Review of Current Imaging and MRI Quantification Techniques. *J. Magn. Reson. Imaging* **45**, 1276–1295 (2017).
137. Huwart, L. *et al.* Magnetic Resonance Elastography for the Noninvasive Staging of Liver Fibrosis. *Gastroenterology* **135**, 32–40 (2008).
138. Dias, N. & Stein, C. A. Antisense Oligonucleotides: Basic Concepts and Mechanisms. *Mol. Cancer Ther.* **1**, 347–355 (2002).
139. Amrutkar, M. *et al.* Protein kinase STK25 regulates hepatic lipid partitioning and progression of liver steatosis and NASH. *FASEB J.* **29**, 1564–1576 (2015).
140. Prakash, T. P. *et al.* Targeted delivery of antisense oligonucleotides to hepatocytes using triantennary N-acetyl galactosamine improves potency 10-fold in mice. *Nucleic Acids Res.* **42**, 8796–8807 (2014).
141. Cansby, E. *et al.* Targeted Delivery of Stk25 Antisense Oligonucleotides to Hepatocytes Protects Mice Against Nonalcoholic Fatty Liver Disease. *Cell. Mol. Gastroenterol. Hepatol.* **7**, 597–618 (2019).
142. Oró, D. *et al.* Cerium oxide nanoparticles reduce steatosis, portal hypertension and display anti-inflammatory properties in rats with liver fibrosis. *J. Hepatol.* **64**, 691–698 (2016).
143. Parra-Robert, M. *et al.* Beyond the Scavenging of Reactive Oxygen Species (ROS): Direct Effect of Cerium Oxide Nanoparticles in Reducing Fatty Acids Content in an In Vitro Model of Hepatocellular Steatosis. *Biomolecules* **9**, (2019).
144. Dhall, A. & Self, W. Cerium Oxide Nanoparticles: A Brief Review of Their Synthesis Methods and Biomedical Applications. *Antioxidants* **7**, (2018).
145. Celardo, I. *et al.* Ce³⁺ Ions Determine Redox-Dependent Anti-apoptotic Effect of Cerium Oxide Nanoparticles. *ACS Nano* **5**, 4537–4549 (2011).
146. Wason, M. S. & Zhao, J. Cerium oxide nanoparticles: potential applications for cancer and other diseases. *Am. J. Transl. Res.* **5**, 126–131 (2013).
147. Walkey, C. *et al.* Catalytic properties and biomedical applications of cerium oxide nanoparticles. *Environ. Sci. Nano* **2**, 33–53 (2015).
148. Heckert, E. G., Karakoti, A. S., Seal, S. & Self, W. T. The role of cerium redox state in the SOD mimetic activity of nanoceria. *Biomaterials* **29**, 2705–2709 (2008).
149. Xia, T. *et al.* Comparison of the Mechanism of Toxicity of Zinc Oxide and Cerium Oxide Nanoparticles Based on Dissolution and Oxidative Stress Properties. *ACS Nano* **2**, 2121–2134 (2008).
150. Parra-Robert, M. *et al.* Mesoporous silica coated CeO₂ nanozymes with combined lipid-lowering and antioxidant activity induce long-term improvement of the metabolic profile in obese Zucker rats. *Nanoscale* **13**, 8452 (2021).

Chapter 2

Mesoporous silica nanorods: synthesis and characterization



2.1. Synthesis of MSR

2.1.1. Introduction

As discussed in Chapter 1, the shape and aspect ratio of mesoporous silica particles have a significant impact on their overall performance and applications in biomedicine. A protocol taking into account several synthesis parameters has to be established to fabricate particles of the desired shape in a reproducible way. Although our group has extensive experience in silica-based materials by sol-gel synthesis, the group did not have experience in the fabrication of mesoporous silica in the form of rods. This thesis has initiated a new line of study within the group that I have developed.

Thus, this chapter focuses on the fabrication of SBA-15-type mesoporous silica rods (MSR). This particular silica type was chosen due to the large (4.6 – 30.0 nm), highly ordered pores¹, and the stability² that characterize it and therefore make it a good candidate for hosting theranostic agents.

Silica rods were synthesized using a sol-gel method in an acidic environment, with TEOS as a source of silica species and the block-copolymer Pluronic P123 as the structure-directing agent.^{1,3} It has been reported that the surfactant forms hybrid cylindrical micelles in the presence of silica species, leading to the self-assembly of hexagonal mesophases.⁴ As previously mentioned, it has been also observed that initial stirring of the reaction mixture, followed by no stirring, can lead to the formation of rod-like particles.^{5,6} All these aspects will be investigated in this chapter.

Silica rods were synthesized following a general protocol with variations of specific parameters. Generally, a solution of hydrochloric acid was prepared in a 250 ml glass bottle. Then, Pluronic P123 was dissolved in the acid. After complete dissolution of the surfactant, TEOS was added to the mixture dropwise under magnetic stirring at a specified temperature. The synthesis details are included in the Annex of this chapter. The stirring was then stopped and the reaction mixture was held at the same temperature in static conditions for 24 h until it was placed in an oven at 80 °C for 24 h for silica aging to occur. Subsequently, the product was filtered in a Büchner funnel and dried in air at 55 °C.



Figure 2-1. Silica formed during the synthesis. Scale bar: 2 cm.

To remove the remaining surfactant molecules, the silica was cleaned with ethanol in a 500 ml soxhlet extractor. For that, the sample was loaded in a cellulose thimble inside the extractor connected to a round-bottomed flask on the bottom and a condenser cooled with flowing water on the top (Figure 2-2). Ethanol was heated to boiling in the flask and the vapor moved up along the soxhlet extractor until it condensed at the top part. Ethanol was filling the extractor, washing away the surfactant. When the ethanol level reached a specific height, it was removed through a thin tube back into the flask. This technique allows us to wash silica multiple times using a relatively small amount of solvent.⁷

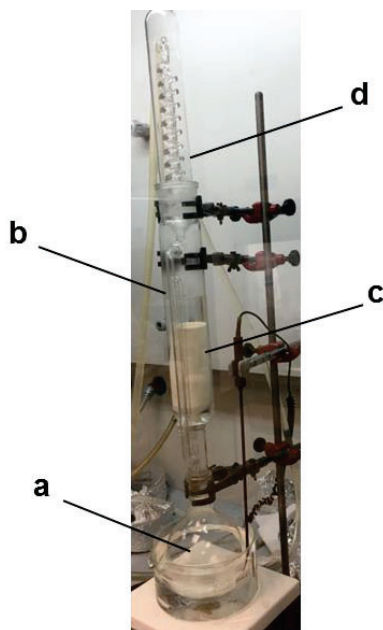


Figure 2-2. Soxhlet cleaning setup. (a) Flask filled with ethanol. (b) Soxhlet extractor. (c) Cellulose thimble loaded with the silica sample. (d) Condenser.

Next step involved the calcination of silica in a tubular furnace in air (550 °C, 5 h). This treatment facilitates the removal of residual surfactant left after cleaning.⁸

2.1.2. Influence of reaction conditions on silica morphology

The first synthesis, which was taken as a point of reference, adapted from Moulin et al.³, involved heating the reaction mixture at 50 °C and adding TEOS while stirring at 700 rpm. The full set of conditions is listed in Table 2-1.

Table 2-1. Starting parameters of silica synthesis. V_r – volume of reaction mixture, V_b – volume of the bottle, $[HCl]$ – hydrochloric acid concentration, $[P123]$ – Pluronic P123 concentration, $[TEOS]$ – TEOS concentration, T_s – temperature during the synthesis, f – stirring rate, t_r – reaction time, T_a – temperature of the aging process, t_a – aging time.

V_r (ml)	V_b (ml)	$[HCl]$ (M)	$[P123]$ (mg/ml)	$\frac{[P123]}{[TEOS]}$	T_s (°C)	f (rpm)	t_r (h)	T_a (°C)	t_a (h)
95	250	1.7	21	0.5	50	700	24	80	24

With this synthesis, rods with a relatively high dispersity of sizes (Figure 2-3 a) were obtained and a large number of bent rods was present among the straight rods. To decrease the polydispersity, higher control over the reaction parameters was to be ensured. The bottle was placed in silicone oil bath in such a way that the whole volume of the reaction mixture was immersed in the silicone oil. The temperature and stirring rate were set three hours before adding the silica precursor. TEOS was then added at a steady pace of approximately 120 drops per minute. This contributed to higher temperature homogeneity across the reaction mixture and a balanced distribution of silica species, resulting in the formation of more straight and monodisperse rods (Figure 2-3 b).

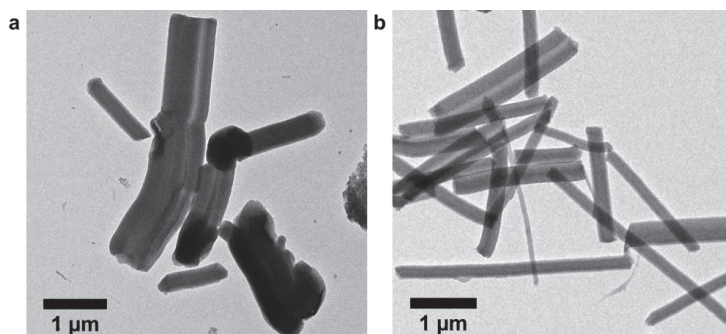


Figure 2-3. Transmission electron microscopy (TEM) morphologies of rods obtained (a) before and (b) after the initial optimization of synthesis parameters.

The effects of temperature and stirring rate were studied by applying different combinations of these parameters in relation to the reference synthesis of Table 2.1, with temperature varying from 40 °C to 60 °C and stirring rate from 500 rpm to 700 rpm. It has been reported in the literature that synthesis at lower temperatures only leads to the formation of amorphous silica.⁹ On the other hand, other studies indicated that temperatures above 60 °C result in a high degree of particle bending and production of tori-like silica particles.³ Moreover, it was also investigated if scaling the amount of the reagents to a different total reaction volume can affect the morphology. The variations of synthesis parameters are listed in Table 2-2. Due to the possible influence of various synthesis parameters, the synthesis conditions were chosen based on a fractional factorial experiment design.¹⁰ A set of two values was tested for each of the three conditions, and the effect of each condition could be investigated by performing $2^{3-1} = 4$ syntheses assuming that the effect of the interactions between synthesis parameters is negligible.

Table 2-2. Sets of synthesis conditions assayed: temperature (T_s), stirring rate (f) and the ratio between the volume of the reaction mixture and the volume of the bottle (V_r/V_b), in the sol-gel synthesis, and resulting silica morphologies.

Sample identification (ID)	T_s (°C)	f (rpm)	V_r/V_b	Morphology
MSN-3	40	500	0.5	branched network of rods
MSN-4	40	700	0.4	straight rods, AR \approx 4.5
MSN-5	60	500	0.4	amorphous
MSN-6	60	700	0.5	straight rods, AR \approx 15; tori

Transmission electron microscopy images of obtained particles are shown in Figure 2-4.

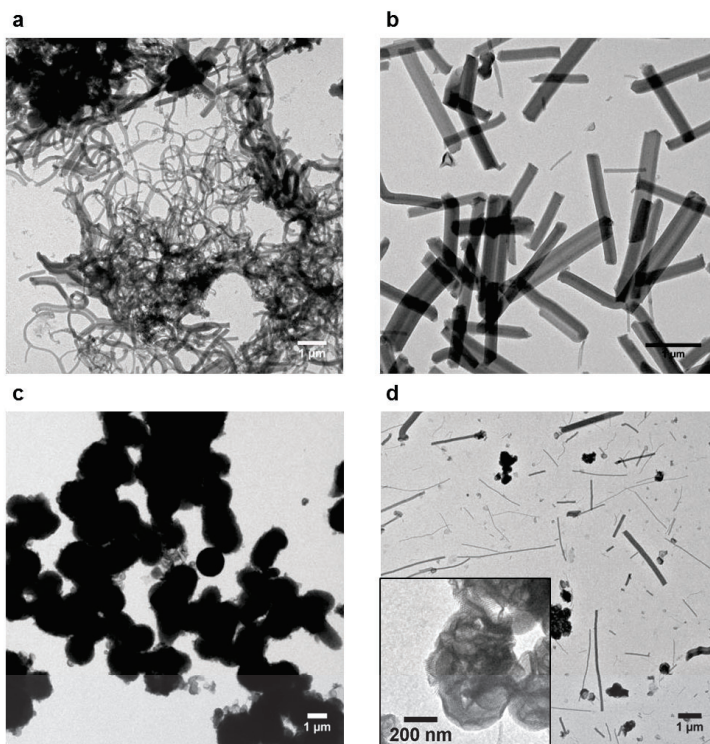


Figure 2-4. TEM morphologies of silica particles obtained at sets of conditions described in Table 2-2. a) MSN-3, b) MSN-4, c) MSN-5, d) MSN-6.

While the influence of the volume ratio in the studied range was not clear, a dependence of the shape on the stirring rate was observed. At a stirring rate of 700 rpm, rod shaped particles were obtained. At 60 °C thin and long rods were observed along with folded, tori-like particles, while at 40 °C, rods with aspect ratio of approximately 4.5 were obtained – a morphology similar to the particles produced in the previous syntheses. However, the sample synthesized at 40 °C had a lower percentage of bent rods compared to the one fabricated at 50 °C, indicating that these differences can be attributed to the temperature effect. At a lower stirring rate (500 rpm), different morphologies were observed: at 40 °C, a network of bent silica rods was formed, while synthesis at a higher temperature (60 °C) resulted in amorphous, semi-spherical particles. The mechanism of this effect is not clear - increased bending of particles observed at 700 rpm at increasing temperature was expected, as it was reported in the literature.^{6,11} A different relationship between the synthesis conditions

and silica morphology suggested by the results obtained at 500 rpm could illustrate how small experimental details can shift the equilibrium and lead to the formation of different morphologies. One of the possible reasons of such differences could be attributed to varying V_r/V_b ratio that was different than in the literature.

As the synthesis at 40 °C and 700 rpm (MSN-4) favoured the formation of straight rods, it was used as a further reference synthesis and relabeled as MSR1. Different conditions, such as acidity, surfactant concentration and stirring time were studied in terms of their influence on particle size and shape.

Another synthesis protocol, adapted from Johansson et al.¹², has also been used. However, unlike in the article, n-heptane was not added to the reaction mixture. In this way, the protocol compared better with the previous syntheses. While the surfactant to TEOS ratio was kept constant, the major differences to the previously described syntheses involved increasing hydrochloric acid concentration from 1.7 M to 2.0 M, the surfactant concentration from 21 mg/ml to 30 mg/ml, and the V_r/V_b ratio from 0.4 to 0.3. These changes led to the formation of shorter and wider particles, as observed in scanning and transmission electron microscopies (Figure 2-5). Scanning electron microscopy (SEM) images indicated the presence of a large number of rods of uniform sizes. TEM images allowed to observe the silica rods in more detail and have been used for the calculation of mean particle sizes. The shorter particles with bacteria-like shapes and a mean aspect ratio of 2.2 will be hereafter referred to as short rods (SR), in contrast to longer particles, with AR of 4.7, labeled as long rods (LR). These two types of particles will be used and compared in further studies throughout the thesis due to significant differences in their sizes and aspect ratios.

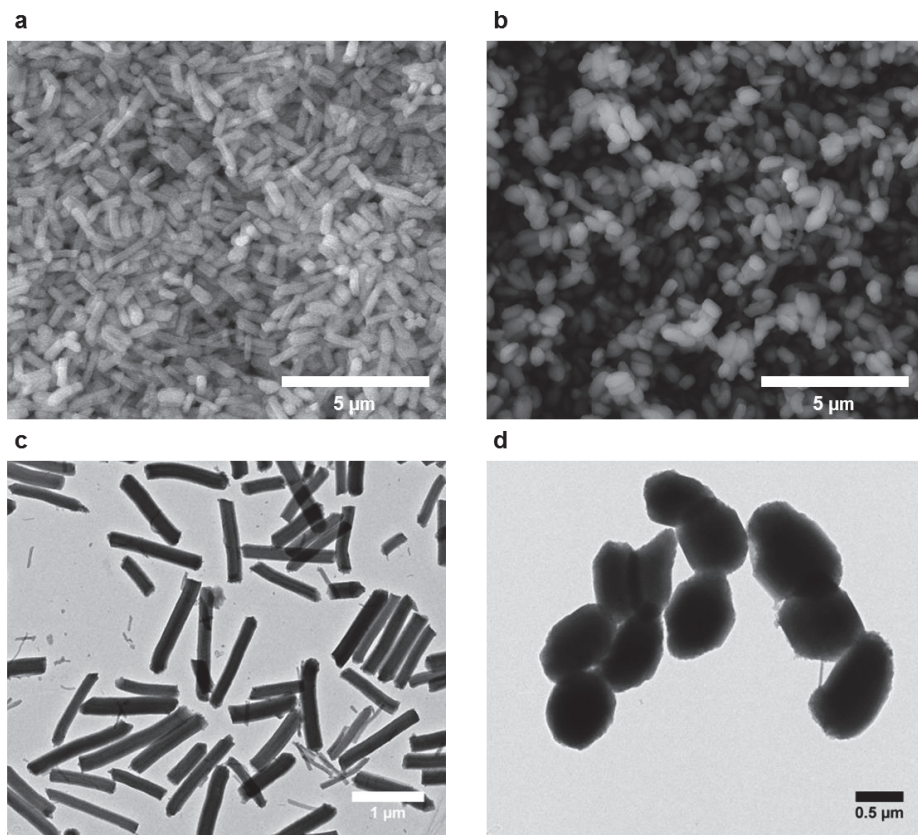


Figure 2-5. SEM images of (a) long and (b) short rods. TEM images of (c) long and (d) short rods.

It was not clear if the change of the aspect ratio was a result of the change in acidity, the surfactant concentration, the volume of the solution or rather a combination of all three. To determine the factor predominantly responsible for the change of morphology, each possible combination of the three varying synthesis parameters at two levels was studied while keeping the temperature, stirring rate and P123:TEOS ratio constant. The synthesis parameters and the resulting rod sizes are listed in Table 2-3.

Table 2-3. Morphologies of silica rods obtained at various conditions. Fixed parameters: $T_s = 40$ °C, $f = 700$ rpm, $[P123]/[TEOS] = 0.5$.

Sample ID	[HCl] (M)	[P123] (mg/ml)	$\frac{V_r}{V_b}$	Length (μm)	Width (μm)	Aspect ratio
MSR1 (LR)	1.7	21	0.4	1.4 ± 0.3	0.3 ± 0.1	4.7 ± 1.3
MSR2 (SR)	2.0	30	0.3	0.9 ± 0.1	0.4 ± 0.1	2.2 ± 0.7
MSR3	1.7	30	0.4	1.2 ± 0.2	0.3 ± 0.1	4.0 ± 1.0
MSR4	2.0	21	0.3	0.8 ± 0.1	0.4 ± 0.1	2.2 ± 0.5
MSR5	1.7	30	0.3	1.0 ± 0.2	0.4 ± 0.1	2.6 ± 0.6
MSR6	2.0	21	0.4	0.9 ± 0.2	0.3 ± 0.1	3.0 ± 0.9
MSR7	1.7	21	0.3	1.4 ± 0.3	0.3 ± 0.1	5.4 ± 1.3
MSR8	2.0	30	0.4	1.0 ± 0.2	0.4 ± 0.1	2.7 ± 0.8

A factorial design analysis¹⁰ of the obtained rod sizes was used to analyse the effect of each synthesis parameter. The specification of variables used in the design is presented in Table 2-4.

Table 2-4. Specification of variables in the experimental design.

Variable	Experimental domain	
	(-) level	(+) level
x_1 : HCl concentration (M)	1.7	2.0
x_2 : P123 concentration (mg/ml)	21	30
x_3 : Reaction mixture volume to bottle volume ratio	0.3	0.4

The matrix of the experimental design is shown in Table 2-5.

Table 2-5. Model matrix and the measured rod dimensions response.

Sample ID	I	x_1	x_2	x_3	$x_1 x_2$	$x_1 x_3$	$x_2 x_3$	$x_1 x_2 x_3$	L (μm)	w (μm)	AR
LR	+	-	-	+	+	-	-	+	1.4	0.3	4.7
SR	+	+	+	-	+	-	-	-	0.9	0.4	2.2
MSR3	+	-	+	+	-	-	+	-	1.2	0.3	4.0
MSR4	+	+	-	-	-	-	+	+	0.8	0.4	2.2
MSR5	+	-	+	-	-	+	-	+	1.0	0.4	2.6
MSR6	+	+	-	+	-	+	-	-	0.9	0.3	3.0
MSR7	+	-	-	-	+	+	+	-	1.4	0.3	5.4
MSR8	+	+	+	+	+	+	+	+	1.0	0.4	2.7

The effect of each parameter on the length, width and aspect ratio of the rods has been evaluated using the following response model:

$$y = b_0 + b_1x_1 + b_2x_2 + b_3x_3 + b_{12}x_1x_2 + b_{13}x_1x_3 + b_{23}x_2x_3 + b_{123}x_1x_2x_3$$

Where y represents the physical property measured (length L , width w or aspect ratio AR). The b_k parameters indicate the magnitude of the effect of the x_k variable, while the b_{kl} and b_{klm} coefficients correspond to the effect of the interaction between two or three variables (x_k , x_l or x_k , x_l , x_m), respectively. The interaction coefficients were not considered in this study. The coefficients were calculated by either adding or subtracting the measured response values, depending on the signs of the levels of the analysed variable, and dividing the result by the number of experiments:

$$b_{1,L} = 1/8 (-1.4 + 0.9 - 1.2 + 0.8 - 1.0 + 0.9 - 1.4 + 1.0) = -0.18$$

$$b_{2,L} = 1/8 (-1.4 + 0.9 + 1.2 - 0.8 + 1.0 - 0.9 - 1.4 + 1.0) = -0.05$$

$$b_{3,L} = 1/8 (1.4 - 0.9 + 1.2 - 0.8 - 1.0 + 0.9 - 1.4 + 1.0) = 0.05$$

The following polynomials were obtained:

$$L = b_{0,L} - 0.18x_1 - 0.05x_2 + 0.05x_3$$

$$w = b_{0,w} + 0.03x_1 + 0.03x_2 - 0.03x_3$$

$$AR = b_{0,AR} - 0.83x_1 - 0.48x_2 + 0.25x_3$$

Where $b_{0,L}$, $b_{0,w}$ and $b_{0,AR}$ are constants. By comparing the coefficients corresponding to the effect of each experimental variable, it can be seen that the acidity seemed to have the most predominant effect on the length of the rods, with shorter rods formed

at a lower pH. Moreover, the results suggested that increasing the acidity and the surfactant concentration, as well as decreasing the V_r/V_b ratio, had a similar effect on the increase of rod thickness. Overall, the HCl concentration had the largest influence on the MSR aspect ratio over the studied range of variable values.

The size obtained from TEM and SEM measurements could not be compared with the often-used technique of dynamic light scattering (DLS), since this technique is based on a model assuming the presence of spherical particles. Another aspect of the material preventing us from using this technique was the poor stability of MSR aqueous dispersions. To increase the dispersion stability for applications described in the following chapters, the rods were dispersed in a solution of a sugar, D-mannitol.

Changing the reaction time between 3 h and 24 h did not appear to affect the shape significantly (Table 2-6). This can suggest that in the presented system, the rods of the established shape were already formed at $t_r = 3$ h. The stirring time (t_s) was studied in the range of 3 to 5 min. Lower polydispersity for $t_s = 5$ min may suggest that the hydrolysis of TEOS was not complete at shorter stirring times.

Table 2-6. Morphologies of MSRs obtained by applying different stirring times (t_s) and reaction times (t_r) compared to the standard LR or SR protocol. All the other synthesis parameters were the same as for the reference sample labeled with the same symbol (LR or SR).

Sample ID	t_s (min)	t_r (h)	Length (μm)	Width (nm)	Aspect ratio
LR	5	24	1.4 ± 0.3	0.3 ± 0.1	4.7 ± 1.3
LR-A	4	3	1.3 ± 0.3	0.3 ± 0.1	5.3 ± 1.5
SR	4	3	0.9 ± 0.1	0.4 ± 0.1	2.2 ± 0.7
SR-A	5	24	0.9 ± 0.1	0.5 ± 0.1	1.8 ± 0.3
SR-B	3	3	1.0 ± 0.1	0.4 ± 0.1	2.7 ± 0.8

An important aspect of nanomaterial synthesis that is often neglected is the reproducibility of synthesis. The synthesis of long and short rods has been repeated in the same conditions with good reproducibility many times during the development of this thesis (over 10 times for LR and 5 for SR). Table 2-7 shows the results of rod morphology characterization which was performed for three different batches of both types of rods. It needs to be noted that it was very difficult to obtain rods of exactly the same mean sizes in each synthesis as it appears to depend on many independent factors, but the widths, lengths and aspect ratios of rods all lie within the error obtained from the standard deviation of the size distributions.

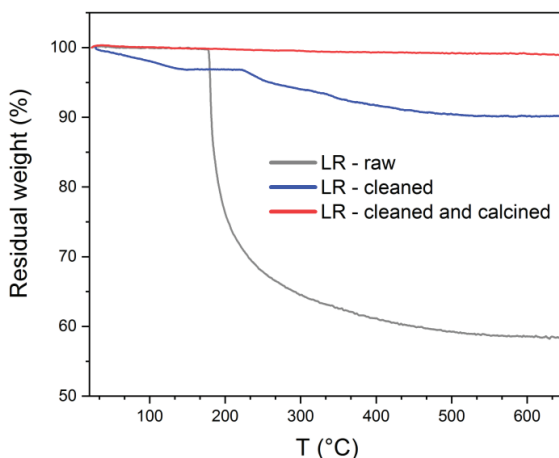
Table 2-7. Geometrical characterization of three different batches of LR and SR to illustrate the synthesis reproducibility.

Sample ID	Length (μm)	Width (μm)	Aspect ratio
LR-1	1.4 ± 0.3	0.3 ± 0.1	4.7 ± 1.3
LR-2	1.4 ± 0.4	0.3 ± 0.1	5.3 ± 1.7
LR-3	1.3 ± 0.3	0.3 ± 0.1	5.0 ± 1.6
SR-1	0.9 ± 0.1	0.4 ± 0.1	2.2 ± 0.7
SR-2	0.9 ± 0.2	0.5 ± 0.1	2.0 ± 0.4
SR-3	0.8 ± 0.1	0.4 ± 0.1	2.2 ± 0.4

The synthesis protocol followed by soxhlet cleaning enabled us to fabricate MSRs with high throughput. Remarkably, approximately 1.0 – 1.2 g of MSR material was produced in a single batch.

2.1.3. Properties of MSR

Thermogravimetry (TGA) studies (Figure 2-6) have shown that 24 cycles of soxhlet cleaning removed the vast majority of the surfactant. Heating the sample to 650°C resulted in a 10% decrease of mass, compared to 42% mass reduction observed in as-prepared rods not cleaned by soxhlet. The remaining impurities were removed after calcination. 1% of mass reduction in calcined silica is attributed to the elimination of adsorbed water from moisture.

**Figure 2-6.** TGA curves of LR: as-prepared, soxhlet-cleaned and after subsequent calcination.

The porosity of silica nanorods has been analysed by TEM studies (Figure 2-7 a), where parallel channels of approximately 5 nm in diameter, running along the rod axis, were observed. It was also seen that the channels were arranged in a hexagonal array (Figure 2-7 b, c).

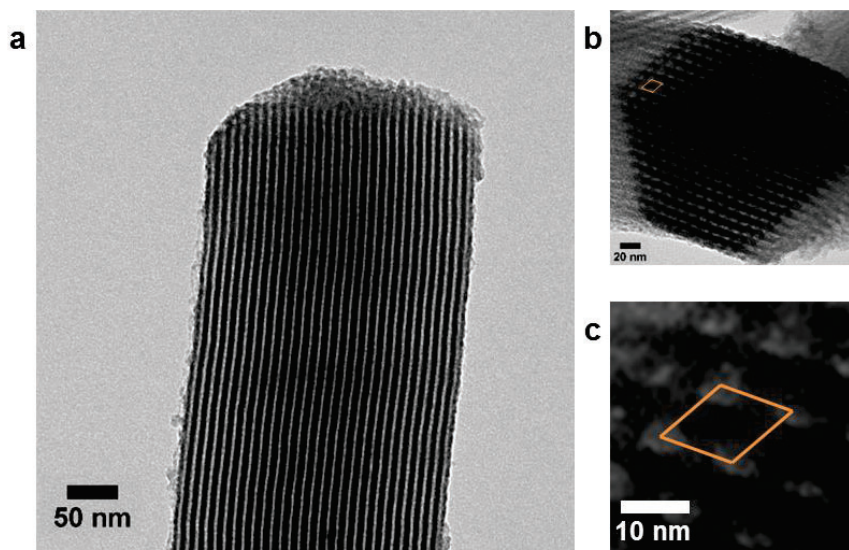


Figure 2-7. (a) TEM image showing the pores inside a silica rod. Silica walls are seen as dark image and the parallel channels are represented as bright lines. (b) Cross-section of a silica rod showing a hexagonal arrangement of the pores. Unit cell is marked in color. (c) Magnification of the image showing the unit cell.

The size of the pore spacings observed in TEM (approximately 10 nm) was compared with the lattice parameter obtained from small-angle X-ray scattering (SAXS). The SAXS pattern is shown in Figure 2-8. The scattering reflections at low angles are the ones expected from hexagonal pore ordering ($p6mm$ space group) previously reported for SBA-15.¹

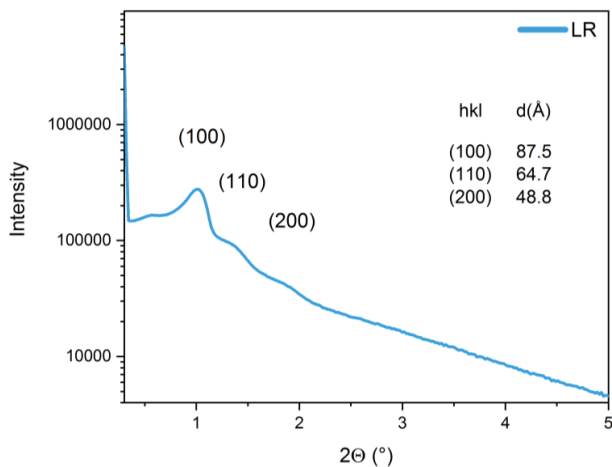


Figure 2-8. SAXS pattern of LR. Scattering reflections are indexed in a hexagonal unit cell of the $p6mm$ space group.

The lattice parameter was calculated using the equation:

$$\frac{1}{d_{hkl}^2} = \frac{4}{3} \left(\frac{h^2 + hk + k^2}{a^2} \right) + \frac{l^2}{c^2}$$

Where d_{hkl} is the d-spacing between planes indicated by Miller indices h, k, l , while a and c are the lattice parameters ($a = b$ for a hexagonal lattice). The lattice parameter of the hexagonal lattice of silica mesopores was calculated from d_{100} ($h = 1, k = l = 0$) spacing obtained from SAXS measurements ($d_{100} = 87.5 \text{ \AA}$). The calculated lattice parameter ($a = 10.1 \text{ nm}$) was in agreement with the sizes measured by TEM.

The porosity of silica rods has been further investigated by nitrogen adsorption isotherm. Both long and short rods exhibited type-IV isotherms with H1 type hysteresis (Figure 2-8 a, b, c), which correspond to mesopores with narrow pore size distribution.¹³

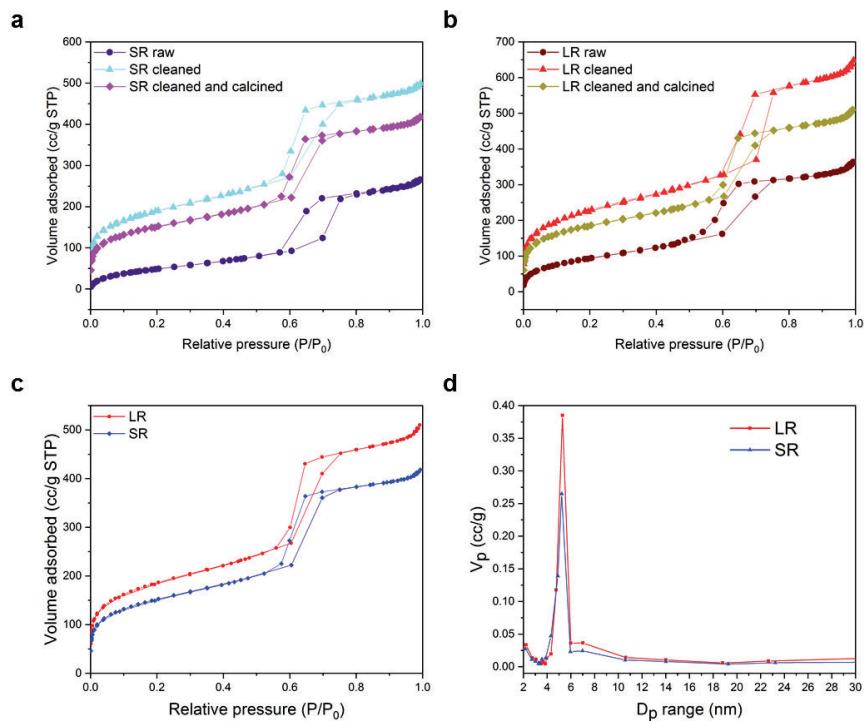


Figure 2-9. (a) BET nitrogen adsorption isotherms of SR – as-prepared, soxhlet-cleaned and calcined after cleaning. (b) BET nitrogen adsorption isotherms of LR – as-prepared, soxhlet-cleaned and calcined after cleaning. (c) Comparison of BET isotherms of LR and SR (cleaned and calcined samples used in further experiments). (d) Pore size distribution in LR and SR.

The mean pore diameters of SR and LR calculated from BET isotherms (Table 2-8) were 5.0 nm and 5.2 nm (after cleaning and calcination), respectively, in accordance with the approximate pore size observed in TEM.

Table 2-8. Porosity data of MSRs obtained from nitrogen adsorption/desorption isotherms. Total BET surface area (S_{BET}), total pore volume (V_{total}), and pore diameters (D_{BJH}) obtained from the desorption branches, of LR and SR. Data obtained for raw, soxhlet-cleaned (40 cycles), as well as soxhlet cleaned and calcined samples.

Sample	S_{BET} (m ² /g)	V_{total} (cc/g)	D_{BJH} (nm)	
SR	Raw	188	0.41	5.5
	Cleaned	672	0.77	4.9
	Cleaned and calcined	548	0.65	5.0
LR	Raw	346	0.56	4.9
	Cleaned	827	1.00	5.5
	Cleaned and calcined	673	0.79	5.2

Both types of MSRs have a large specific surface area and this value is higher in LR than in the case of SR, similarly to the total pore volume. Soxhlet cleaning greatly increased the specific surface area by opening up the space occupied by surfactant molecules. Calcination was found to decrease the specific surface area – this effect can be attributed to the shrinking of the hexagonal framework due to the densification of porous silica at high temperatures.⁸ However, this did not have any qualitative effect on the ordered porosity of the rods, as shown in Figure 2-10.

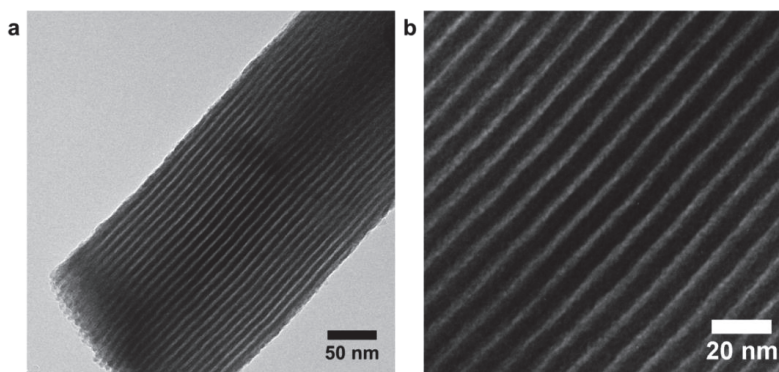


Figure 2-10. TEM images of a calcined rod (LR), showing the uniform porosity.

2.2. Chapter summary

Anisotropic rod-like mesoporous silica particles were synthesized using a block-copolymer templated, acid catalysed sol-gel method. Slight variations of reaction conditions led to the formation of different morphologies. Parameters such as stirring rate, temperature, acidity, surfactant concentration and the reaction mixture volume, all affected particle shape and size. The dependence of the particle morphology on all these parameters is complex and we decided to investigate the variation of only a few of those parameters. However, over the studied range of variable values, the acidity was found to have a larger effect on the rod dimensions than the surfactant concentration and the reaction mixture volume, as increasing acidity contributed to the formation of shorter rods.

By tuning the synthesis conditions, rods of two distinct aspect ratios were obtained and the synthesis was found to be reproducible yielding over 1 g of pure silica rods from a single batch. The two morphologies are referred to as long rods (LR, $AR = 4.7$) and short rods (SR, $AR = 2.2$). The MSRs were characterized by an array of hexagonally-ordered cylindrical pores running along the main axis of the rods. Moreover, both types of rods had a high surface area (827 m²/g for soxhlet cleaned LR and 672 m²/g for SR) and pore volume (1 cm³/g for LR and 0.8 cm³/g for SR) with a pore diameter of approximately 5 nm.

Soxhlet cleaning greatly improved the purity of silica rods, while calcination contributed to the elimination of residual surfactant but also resulted in a decrease in the specific surface area.

The properties of both MSR types such as longitudinal ordered mesopores, high surface area and pore volume, were beneficial for the modification of the rods with chemical species, described in the following chapter.

2.3. Annex

2.3.1. Materials

Mesoporous silica rods (MSR) were synthesized in our laboratory. Hydrochloric acid (37%), poly(ethylene glycol)-block-poly(propylene glycol)-block-poly(ethylene glycol) (Pluronic P123), tetraethyl orthosilicate (TEOS) were purchased from Sigma-Aldrich and used as received. Ethanol was purchased from PanReac. The purity of all reagents was 98% or higher.

2.3.2. Synthesis of long rods (LR)

In a typical synthesis, 2 g of Pluronic P123 were dissolved in 95 ml 1.7 M hydrochloric acid solution. After obtaining a homogeneous solution, the temperature was increased to 40 °C and the solution was stirred at 700 rpm. After 3 h, 4.2 g tetraethyl orthosilicate (TEOS) were added dropwise. Stirring was stopped after 5 min and the reaction was kept in static conditions for 24 h. After that, the reaction bottle was transferred to an oven at 80 °C and kept there for 24 h. In a subsequent step, silica was filtered and dried at 55 °C overnight. The surfactant was removed by washing the product in ethanol (24-40 cycles of a 500 ml soxhlet). Then, the material was calcined in air at 550 °C for 5 h.

2.3.3. Synthesis of short rods (SR)

2.4 g of Pluronic P123 were dissolved in 80 ml 2 M hydrochloric acid solution. After obtaining a homogeneous solution, the temperature was increased to 40 °C and the solution was stirred at 700 rpm. After 3 h, 5.1 g TEOS were added dropwise. Stirring was stopped after 4 min and the reaction was kept in static conditions for 3 h. Then, the reaction bottle was transferred to an oven at 80 °C and kept there for 24 h. Then, silica was filtered and dried at 55 °C overnight. The surfactant was removed by washing the product in ethanol (24-40 cycles of a 500 ml soxhlet). Finally, the material was calcined in air at 550 °C for 5 h.

2.3.4. Soxhlet cleaning

As-prepared silica was placed in a cellulose soxhlet thimble (Whatman) and put inside a 500 ml soxhlet extractor. The bottom part was connected to a round-bottomed flask filled with ethanol and pumice stones to facilitate boiling. The flask was immersed in a silicone oil bath on top of a hot plate. On the top part of the soxhlet, a condenser cooled continuously with flowing water was placed. The silicone oil bath was heated to 125 °C and the moment when ethanol started condensing in the extractor was marked as the start time. The time of one cycle (until emptying of the extractor) was approximately 2 h 25 min. Silica was cleaned for 24-40 cycles.

Afterwards, the heating was stopped and the thimble was removed. Silica was left in the thimble until complete evaporation of the remaining ethanol.

2.3.5. Calcination

Silica powder was placed in an alumina boat (Sigma-Aldrich) and placed inside a tubular furnace (ST 1002540, HOBERSAL). A thermal treatment was carried out in air, at 550°C for 5 hours, with a heating ramp of 5 °C per minute.

2.3.6. Transmission electron microscopy (TEM)

Silica particle morphology was examined by a JEOL 1210 transmission electron microscope (TEM) operating at 120 kV accelerating voltage. Samples for TEM analysis were prepared by drop-casting ethanol dispersions of the particles (1 mg/ml) on TEM copper grids. The size distributions were obtained using ImageJ software¹⁴ from a statistical number of the particles ($n=200$) from several frames acquired from different regions of the sample.

2.3.7. Scanning electron microscopy (SEM)

Field emitting scanning electron microscope (SEM, FEI Quanta 200 FEG, Thermo Fisher Scientific, Oregon, USA) was used to study the morphologies of silica particles. The images were acquired in high vacuum and with an accelerating voltage of 10 kV. The samples were prepared by covering a carbon tape attached to a metal SEM holder with a small amount of silica powder. The unattached excess of powder was then removed.

2.3.8. Nitrogen adsorption/desorption isotherm

Nitrogen adsorption/desorption isotherms were measured at 77 K using Micromeritics ASAP 2000 apparatus in standard operating mode. Before analysis, all samples were degassed for 20 h at 180 °C under vacuum ($p < 2 \times 10^{-3}$ torr). Pore size distribution was calculated from the Barrett-Joyner-Halenda (BJH) model from the desorption branch. The Brunauer-Emmett-Teller (BET) specific surface area was obtained in the 0.05 – 0.30 p/p_0 range.

2.3.9. Small angle X-ray scattering (SAXS)

SAXS measurements were performed using Bruker D8-Discover in 2θ range from 0.15 to 5° in steps of 0.02° with $\text{CuK}\alpha$ radiation. A lead plate was placed perpendicular to the sample plane, slightly above it, held with a specific support designed on purpose to minimize the background at the detector.

2.3.10. Thermogravimetric analysis

Around 2 mg of silica rods sample were measured in a SETSYS Evolution TGA (Setaram) from room temperature to 650 °C at a heating rate of 10 °C/min and under dynamic dry air flow.

2.3.11. Safety

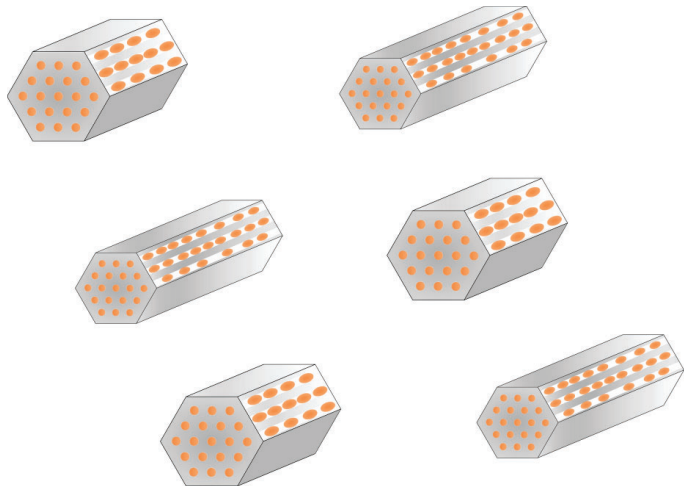
Silica powders used in this work were very easily airborne. Data available for different silica materials indicate that such materials can accumulate in the lungs when inhaled, leading to adverse effects on health, such as silicosis.¹⁵ For this reason, special protective measures were taken while working with silica in powder form. Sample manipulation was performed exclusively in a fume hood. FFP3 masks (3M™ Aura™ 9300/ Handanhy HY9330/ Labbox) were used by every person present in the laboratory at the time of manipulation, and double nitrile gloves were used for working with silica. The interior of the fume hood was then carefully cleaned with ethanol and all material contaminated with silica was disposed in an appropriate solid residue container.

2.4. Chapter references

1. Zhao, D. *et al.* Triblock Copolymer Syntheses of Mesoporous Silica with Periodic 50 to 300 Angstrom Pores. *Science* **279**, 548–552 (1998).
2. Cassiers, K. *et al.* A Detailed Study of Thermal, Hydrothermal, and Mechanical Stabilities of a Wide Range of Surfactant Assembled Mesoporous Silicas. *Chem. Mater.* **14**, 2317–2324 (2002).
3. Moulin, R., Schmitt, J., Lecchi, A., Degrouard, J. & Impéror-Clerc, M. Morphologies of mesoporous SBA-15 particles explained by the competition between interfacial and bending energies. *Soft Matter* **9**, 11085 (2013).
4. Manet, S. *et al.* Kinetics of the Formation of 2D-Hexagonal Silica Nanostructured Materials by Nonionic Block Copolymer Templating in Solution. *J. Phys. Chem. B* **115**, 11330–11344 (2011).
5. Sayari, A., Han, B. H. & Yang, Y. Simple Synthesis Route to Monodispersed SBA-15 Silica Rods. *J. Am. Chem. Soc.* **126**, 14348–14349 (2004).
6. Lee, H. I. *et al.* Morphology-selective synthesis of mesoporous SBA-15 particles over micrometer, submicrometer and nanometer scales. *J. Mater. Chem.* **20**, 8483–8487 (2010).
7. de Ávila, S. G., Silva, L. C. C. & Matos, J. R. Optimisation of SBA-15 properties using Soxhlet solvent extraction for template removal. *Microporous Mesoporous Mater.* **234**, 277–286 (2016).
8. Kleitz, F., Schmidt, W. & Schüth, F. Calcination behavior of different surfactant-templated mesostructured silica materials. *Microporous Mesoporous Mater.* **65**, 1–29 (2003).
9. Zhao, D., Huo, Q., Feng, J., Chmelka, B. F. & Stucky, G. D. Nonionic Triblock and Star Diblock Copolymer and Oligomeric Surfactant Syntheses of Highly Ordered, Hydrothermally Stable, Mesoporous Silica Structures. *J. Am. Chem. Soc.* **120**, 6024–6036 (1998).
10. Lundstedt, T. *et al.* Experimental design and optimization. *Chemom. Intell. Lab. Syst.* **42**, 3–40 (1998).
11. Zhao, D., Sun, J., Li, Q. & Stucky, G. D. Morphological Control of Highly Ordered Mesoporous Silica SBA-15. *Chem. Mater.* **12**, 275–279 (2000).
12. Johansson, E. M., Ballem, M. A., Córdoba, J. M. & Odén, M. Rapid Synthesis of SBA-15 Rods with Variable Lengths, Widths, and Tunable Large Pores. *Langmuir* **27**, 4994–4999 (2011).
13. Ravikovitch, P. I. & Neimark, A. V. Characterization of nanoporous materials from adsorption and desorption isotherms. *Colloids Surfaces A Physicochem. Eng. Asp.* **187–188**, 11–21 (2001).
14. Rasband, W. S. ImageJ, U. S. National Institutes of Health, Bethesda, Maryland, USA, <https://imagej.nih.gov/ij/>, 1997-2018.
15. Park, H. J. *et al.* Acute exposure to silica nanoparticles aggravate airway inflammation: different effects according to surface characteristics. *Exp. Mol. Med.* **47**, (2015).

Chapter 3

Loading the pores of the silica rods with chemical species



3.1. Introduction

The most distinctive features of mesoporous silica are its high surface area and pore volume; characteristics that enable to load it with large amounts of cargo of different chemical character. In this chapter, strategies of obtaining functional silica-based composites by loading the pores with various chemical species are presented along with the material characterization. A more extensive description is included for the pore loading with superparamagnetic iron oxide nanoparticles. The performance of the composites for different imaging techniques is also assessed.

3.2. In-situ fabrication of γ -Fe₂O₃ NPs

3.2.1. Introduction

Superparamagnetic iron oxide nanoparticles (SPIONs) have been widely employed as theranostic agents in nanomedicine.¹⁻³ In particular, due to their magnetic character, and under the influence of a magnetic field, they act as good T₂ MRI contrast agents; shortening the transverse relaxation time of the water-protons in the tissue where they are located and providing a hypotense signal in that specific area. Additionally, they can be employed in hyperthermia or guided by a magnetic field to be used as a drug delivery system.

The magnetic properties of a nanocomposite depend strongly on the magnetic nanoparticle size and crystallinity, the particle-matrix interactions, the magnetic loading, and the degree of dispersion of the particles inside the matrix.⁴ For this reason, embedding nanocrystalline magnetic particles in inorganic host materials such as silica can be advantageous for tailoring the nanoparticle size distribution and ensuring the dispersion of the nanoparticles.⁵ Various strategies have been used to incorporate SPIONs in mesoporous silica carriers and involve either dispersing co-precipitated pre-formed iron oxide nanoparticles in different sol-gel matrices or the precipitation of the particles during the silica matrix formation.⁶⁻⁸

Recently, a method of iron oxide NPs fabrication inside silica rods based on wet impregnation has been reported.^{9,10} In this method, which had been earlier described for loading silica with other chemical species^{11,12}, a precursor salt with a low melting point is mixed with SBA-15 and introduced inside the pores through capillary action after being melted. In a subsequent step, the iron precursor is subjected to a high temperature treatment, yielding iron oxide nanoparticles inside the silica pores. However, the loading parameters and their influence on the iron oxide content, phase composition and magnetic properties were not studied extensively. I will address some of these issues in this chapter.

3.2.2. Loading and characterization

Different impregnation and thermal treatment conditions were investigated as described in Table 3-1. For that, long silica rods were used as the matrix. Iron (III) nitrate nonahydrate ($T_m = 47\text{ }^\circ\text{C}$) was used as the iron precursor.

Table 3-1. Conditions used in silica impregnation with iron (III) nitrate nonahydrate and subsequent thermal treatment.

Sample index	Silica : Iron nitrate nonahydrate (w/w)	Impregnation	Thermal treatment
LR-F1	1:2	Powder mixing, then heating on top of a hot plate (100 °C, 30 min)	700 °C, 3 h
LR-F2	1:1	Powder mixing, then heating on top of a hot plate (100 °C, 30 min)	700 °C, 3 h
LR-F3	1:2	Powder mixing, then heating in a silicone oil bath (60 °C, 30 min, 3 times with mixing in between)	700 °C, 3 h
LR-F4	1:1	Powder mixing, then heating in a silicone oil bath (60 °C, 30 min, 3 times with mixing in between)	400 °C, 3 h
LR-F5	1:1	Impregnation with ethanolic solution (0.5 M) of the precursor	400 °C, 3 h

The initial protocol involved mixing the silica powder with the iron precursor in a vial and heating it to 100 °C on a hot plate, followed by thermal treatment at 700 °C. TEM images have shown particles inside silica pores, but a large amount of iron oxide in the form of individual particles or bigger agglomerates was also attached to the surface of the rods (Figure 3-1 a). This issue was addressed by reducing the amount of the iron precursor used for impregnation but, although in a lesser amount, nanocrystals were still observed on the surface of rods (Figure 3-1 B), and some rods had only empty channels.

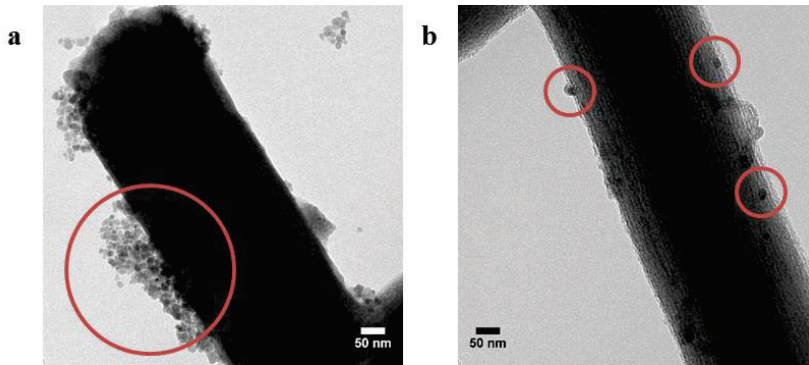


Figure 3-1. TEM images of individual rods after impregnation. (a) silica:iron precursor 1:2 mass ratio (sample LR-F1). (b) silica:iron precursor 1:1 mass ratio (sample LR-F2). Iron oxide particles outside the pores are marked with circles.

To facilitate the introduction of the iron nitrate inside the pores, the powders were thoroughly mixed three times in between heating steps (30 min each). Capillary action was favored by decreasing the impregnation temperature to 60 °C and homogeneous temperature distribution was provided by performing the impregnation in a silicone oil bath instead of placing the vial directly on a hot plate. The new protocol that I have developed improved the homogeneity of the loading and the amount of nanoparticles inside the pores, as can be seen in Figure 3-2 a. Similar results were obtained using a lower post-impregnation treatment temperature of 400 °C instead of 700 °C and by impregnating MSRs with an ethanolic solution of the same precursor (Figure 3-2 b, c).

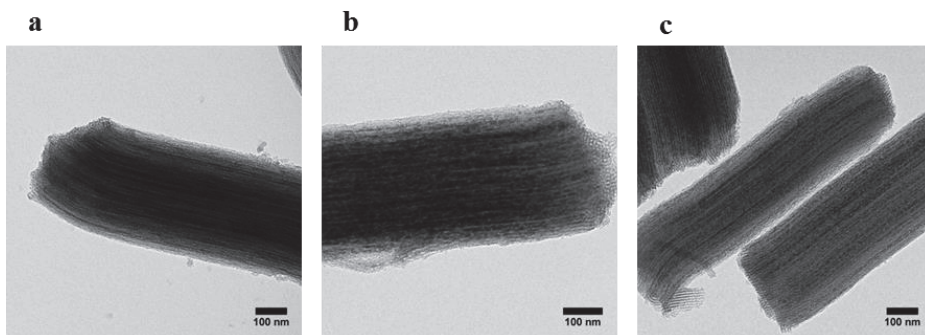


Figure 3-2. TEM images of representative rods of samples (a) LR-F3, (b) LR-F4, (c) LR-F5.

Although the loading of MSR was successful, X-ray diffraction (XRD) results revealed the presence of two distinct iron oxide phases: a magnetic phase, maghemite

(γ - Fe_2O_3), and hematite (α - Fe_2O_3) which presents a very weak magnetization at room temperature. The diffractograms are shown in Figure 3-3. The hematite peaks were present in both LR-F3 and LR-F4, which were thermally treated at 700 °C and 400 °C, respectively. In contrast, the sample impregnated with a precursor solution had a low crystallinity, as indicated by broader diffraction peaks.

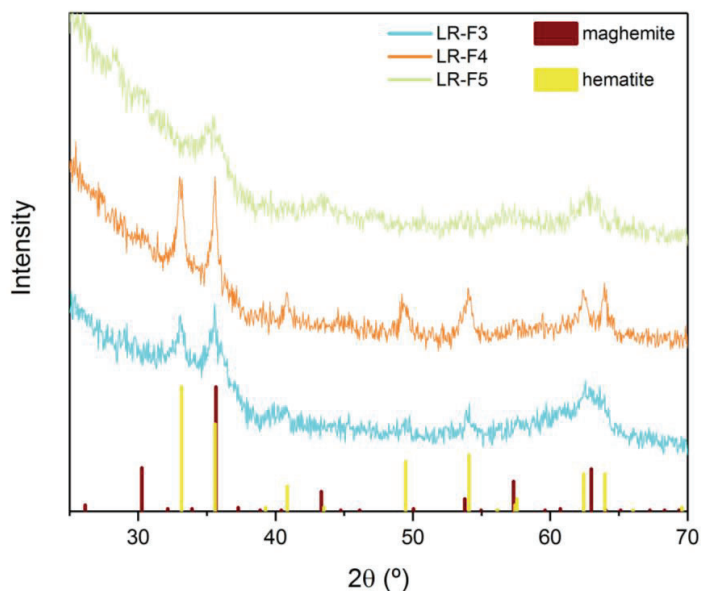


Figure 3-3. X-ray diffractograms of iron oxide loaded LR. Maghemite and hematite main peaks¹³ with their relative intensities.

The presence of hematite in silica rods is not favorable for their application as MRI contrast agents, as the overall magnetization is much lower than it would be with iron oxide particles of maghemite or magnetite phases. To increase the maghemite content in the composites, an additional thermal treatment (425 °C, 3 h) in a reducing atmosphere (95% Ar, 5% H₂, 100 cm³/min) was performed. It was expected that this treatment would induce the transformation of hematite into magnetite, which in prolonged contact with air would undergo gradual oxidation to the isostructural maghemite. X-ray diffractograms of the treated samples showed a decrease in the intensity of the hematite peaks and the appearance of more intense maghemite peaks. The pre- and post-treatment diffractograms are compared in Figure 3-4.

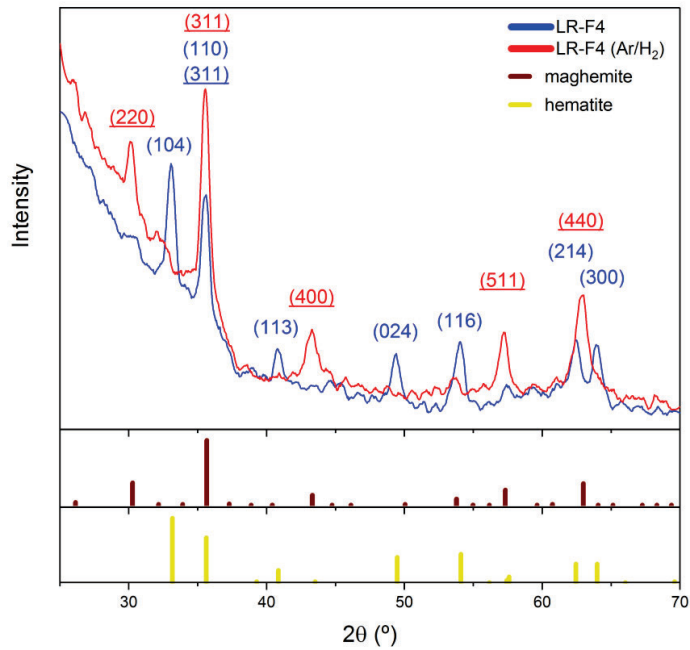


Figure 3-4. X-ray diffractograms before (LR-F4) and after (LR-F4(Ar/H₂)) the thermal treatment in Ar/H₂. The peaks are indexed in hematite (plain text) and maghemite (underlined) unit cells. Insets: XRD theoretical patterns for maghemite (top) and hematite (bottom).

Rietveld refinement was used to calculate the contributions of each phase, as illustrated in Figure 3-5. Table 3-2 shows the calculated phase compositions.

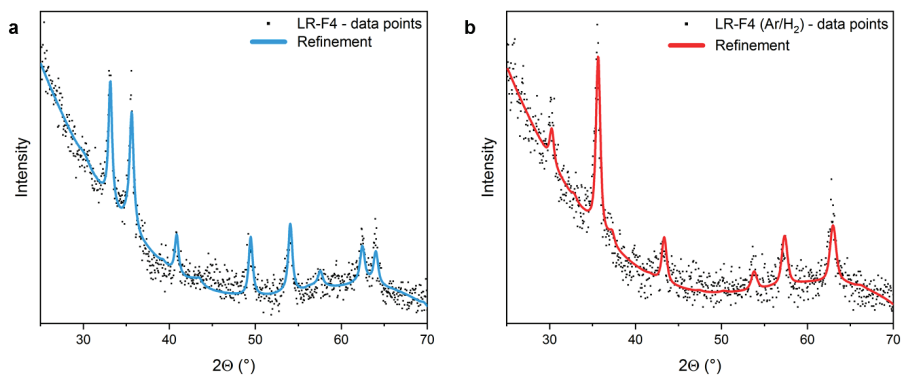


Figure 3-5. Rietveld refinement (using maghemite and hematite diffraction patterns) of the LR-F4 sample (a) after treatment in air, (b) after subsequent treatment in reducing atmosphere.

Table 3-2. Phase composition of iron oxide in silica composites after thermal treatment in air and subsequent treatment in the atmosphere of Ar/H₂.

Sample index	Hematite %		Maghemite %	
	Air treatment	Ar/H ₂	Air treatment	Ar/H ₂
LR-F3	70	0	30	100
LR-F4	85	3	15	97

The significant increase in maghemite content upon treatment in reducing atmosphere encouraged an additional modification of the loading protocol, replacing the two subsequent thermal treatments - in air and Ar/H₂ - with just one treatment (425 °C, 3 h, under 100 cm³/min of Ar/H₂). Following this approach, the time and complexity of material preparation could be reduced while obtaining similar results. Such protocol has been performed on both LR and SR. Throughout the rest of the thesis, these batches will be referred to as Fe₂O₃@LR and Fe₂O₃@SR, respectively. XRD measurements indicated that both Fe₂O₃@LR and Fe₂O₃@SR show only maghemite peaks (Figure 3-6). This was confirmed by the Rietveld refinement of the data (Figure 3-7).

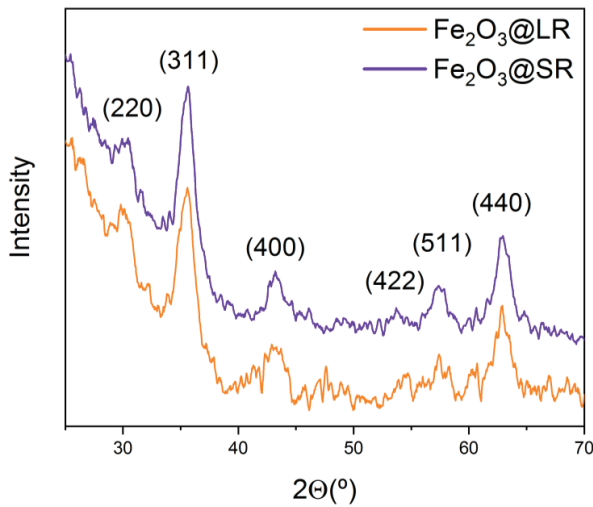


Figure 3-6. XRD diffractograms of Fe₂O₃@LR and Fe₂O₃@SR. The peaks are indexed in γ -Fe₂O₃ unit cell.

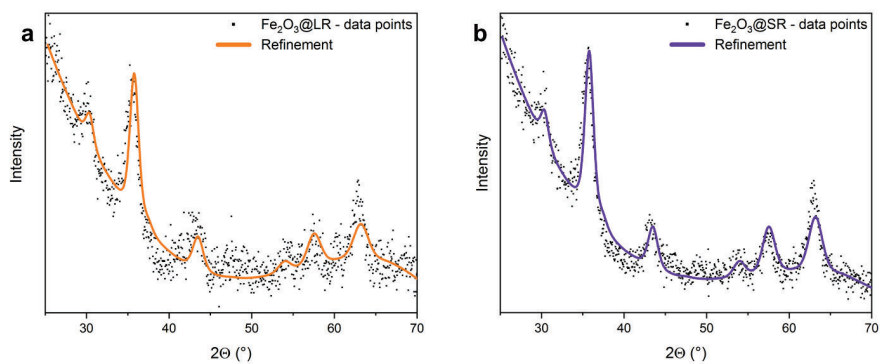


Figure 3-7. Rietveld refinement results of (a) $\text{Fe}_2\text{O}_3@\text{LR}$ and (b) $\text{Fe}_2\text{O}_3@\text{SR}$ XRD patterns.

TEM images showed that both long and short rods were abundantly filled with nanoparticles (Figure 3-8).

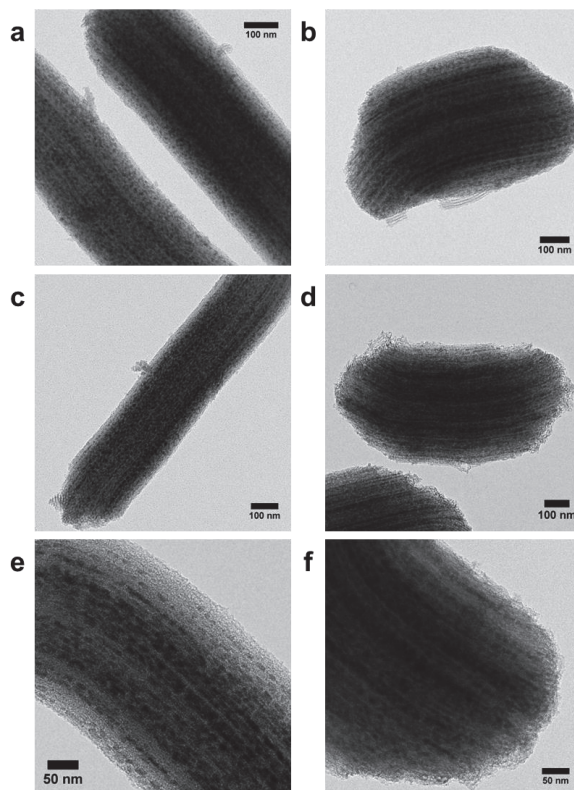


Figure 3-8. TEM images of $\text{Fe}_2\text{O}_3@\text{LR}$ (a, c, e) and $\text{Fe}_2\text{O}_3@\text{SR}$ (b, d, f).

The presence of iron oxide nanoparticles exclusively inside the pores and not attached to the surface was additionally confirmed by tilting the TEM stage and viewing the particles under different angles around the rod axis (Figure 3-9). As expected, under certain angles the channels were more visible and the particles appeared clearly aligned along them. No particles were observed on the outer surface of silica rods and only a very small number of empty rods were observed. The NPs induced local deformations of the pores as indicated by the increased pore width seen around the particles and the tortuosity of the channels along the rod axis.

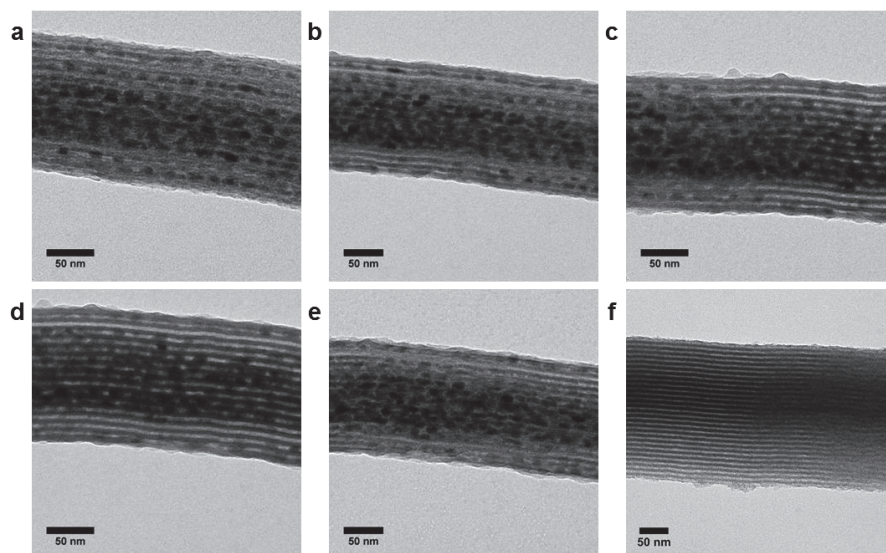


Figure 3-9. (a-e) TEM images of a representative silica rod filled with $\gamma\text{-Fe}_2\text{O}_3$ NPs obtained after tilting the TEM stage around the rod axis. The tilt angles with respect to first image (a) are: (b) 2.8° , (c) 5.5° , (d) 8.9° , (e) 14.8° . (f) A TEM image of an empty rod for comparison.

Electron diffraction studies of maghemite loaded rods indicated that while the particles are formed, confined inside the channels, they grow in a preferential direction. The diffraction pattern of (Figure 3-10) indicates that the crystals have different orientations in the direction perpendicular to the rod axis but all of them share a common preferential $[110]$ orientation along the rod axis. In particular, all the elongated diffraction spots of this pattern can be indexed by considering the superposition of patterns from maghemite crystals along the $[\bar{1}11]$, $[001]$, $[1\bar{1}0]$, $[1\bar{1}\bar{2}]$ and $[\bar{3}32]$ zone axes.

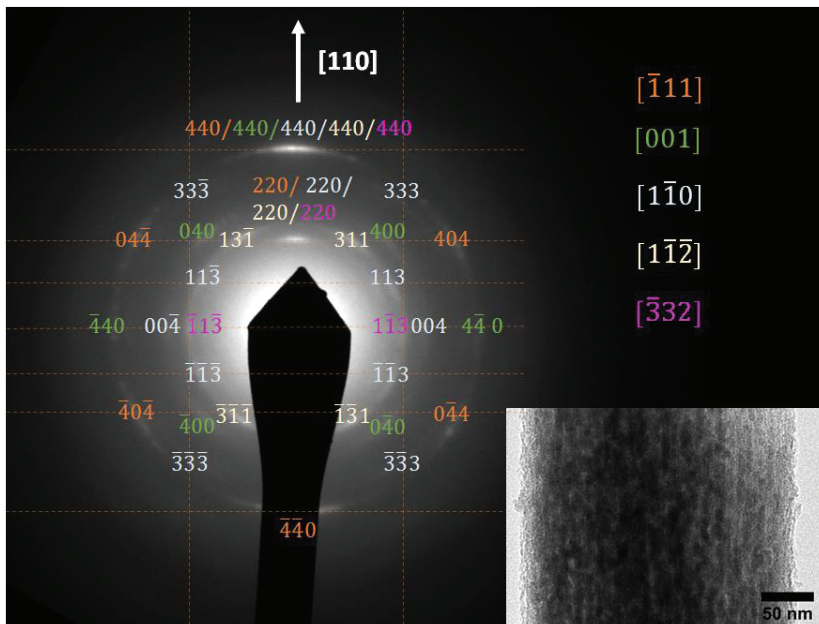


Figure 3-10. Electron diffraction pattern obtained from $\text{Fe}_2\text{O}_3@\text{LR}$ indexed considering the superposition of crystals with orientations along the $[\bar{1}11]$, $[001]$, $[1\bar{1}0]$, $[1\bar{1}\bar{2}]$ and $[\bar{3}32]$ zone axes, indicated in different colors. The parentheses in the Miller indices were omitted for clarity of the image. Inset: Corresponding TEM image of the rod.

The periodicity and loading of the channels were studied using small angle X-ray scattering (SAXS). The results are shown in Figure 3-11. Three peaks were observed in the pattern of LR and were indexed as (100) , (110) and (220) reflections associated with $p6mm$ two-dimensional space group, indicating a hexagonal mesoscopic periodical organization which is characteristic of SBA-15¹⁴ (see Fig. 2-7 c). After loading with iron oxide NPs, the intensity of the peaks decreased, and only (100) reflection was observed with a significantly decreased intensity. This indicates that loading the pores caused a decrease in the periodicity of electron density contrast, confirming the filling of a substantial fraction of the pores.

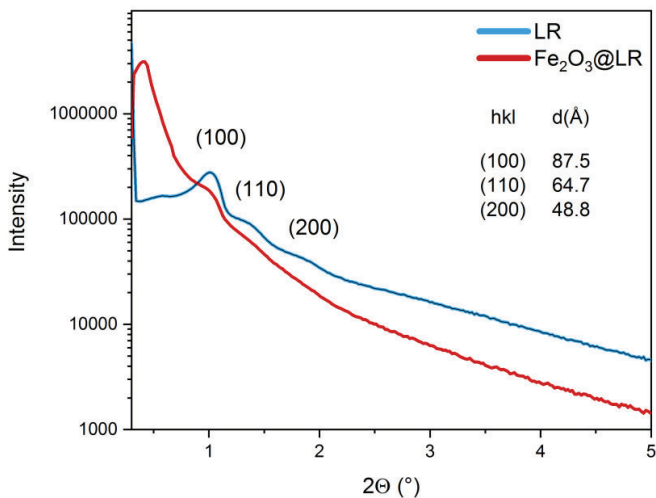


Figure 3-11. SAXS patterns of LR and Fe₂O₃@LR. Scattering reflections are indexed in a hexagonal unit cell of the $p\bar{6}mm$ space group.

The size and shape of nanoparticles filling the pores was difficult to assess from the TEM images of the rods but they appear as having a slightly elongated, ellipsoidal shape. To visualize individual nanoparticles, silica was etched with a concentrated solution of sodium hydroxide. Although the particles formed aggregates that were very difficult to separate, the elongated shape was confirmed in TEM measurements (Figure 3-12). Maghemite phase was identified using electron diffraction.

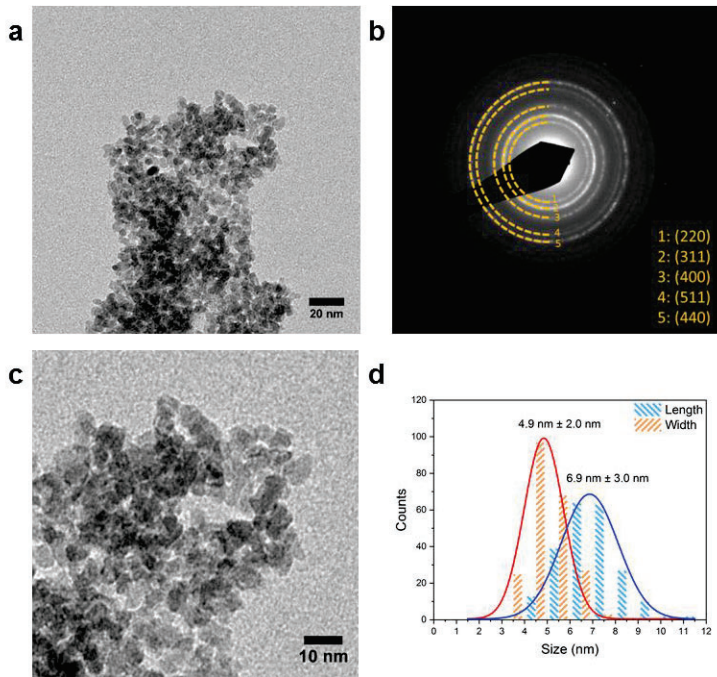


Figure 3-12. (a) TEM image of iron oxide nanoparticles obtained after silica etching in $\text{Fe}_2\text{O}_3@\text{LR}$. (b) Corresponding electron diffraction pattern with rings indexed in maghemite unit cell. (c) A magnification of the TEM image showing an ellipsoidal shape of the nanoparticles. (d) Size distribution of the nanoparticles ($n = 220$) fit with a Gaussian distribution.

EDX mapping was used to determine the distribution of elements inside the rods. The mapping showed a uniform distribution of iron inside the rods, confirming that the rods are filled homogeneously with iron oxide nanoparticles (Figure 3-13).

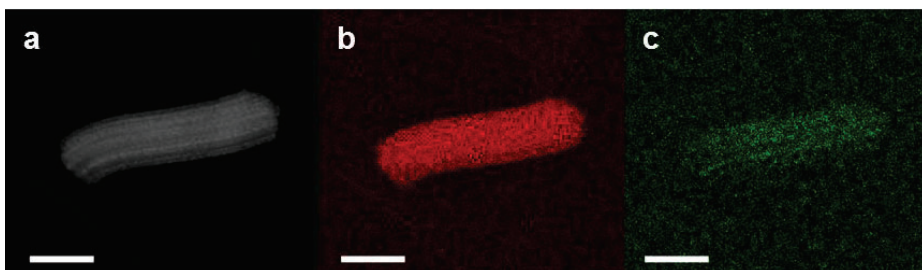


Figure 3-13. EDX maps of $\text{Fe}_2\text{O}_3@\text{LR}$. (a) Electron image. (b) Oxygen map. (c) Iron map. Scale bars: 300 nm.

The presence of γ -Fe₂O₃ was also confirmed by scanning transmission electron microscopy (STEM) with electron energy loss spectroscopy (EELS), as shown in Figure 3-14. This analysis was performed by Dr. Jaume Gázquez (ICMAB) at the *ICTS National Center of Electron Microscopy at Universidad Complutense de Madrid*. The Fe map obtained by integration of the signal of the Fe L_{2,3} edge for each pixel in the spectral image coincided with the map of the pre-peak of O K edge spectrum characteristic for iron oxide, confirming the presence of iron oxide nanoparticles inside the pores and excluding the presence of metallic iron. Moreover, the intensity ratio of iron L₃/L₂ white lines in Fe L_{2,3} spectra of approximately 5.5 indicated the presence of γ -Fe₂O₃ rather than Fe₃O₄, which presents a lower L₃/L₂ ratio.^{15,16}

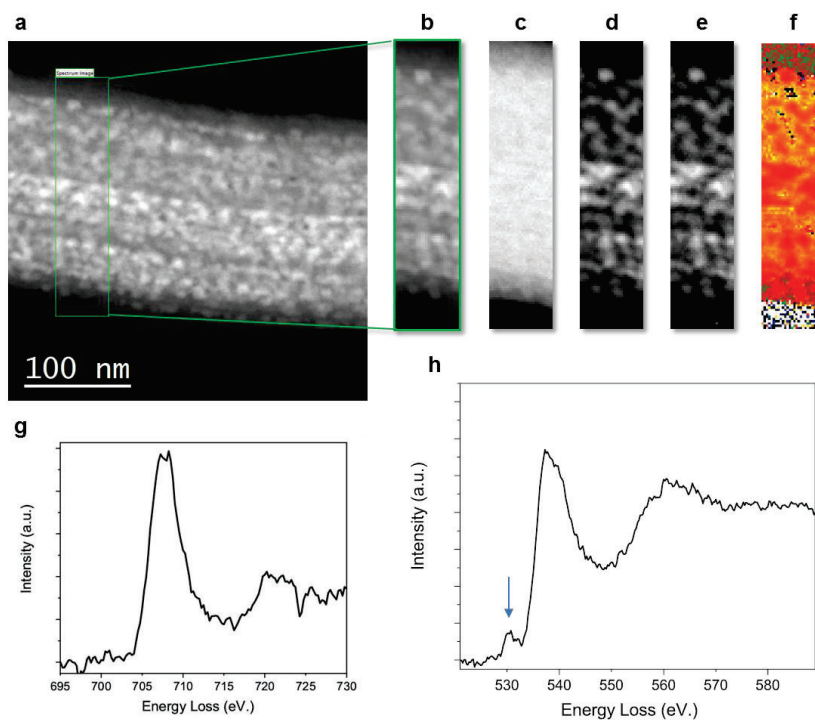


Figure 3-14. EELS data of Fe₂O₃@LR. (a) Zeta contrast image of a single rod. (b) Annular Dark Field (ADF) image of the area highlighted in the zeta contrast image. (c) Oxygen map generated by the integration of the signal of the O edge for each pixel in the spectrum image (SI). (d) Fe map generated by the integration of the signal of the Fe edge for each pixel in the SI. (e) Prepeak map obtained by selecting pixels in which the spectra contained a feature appearing at 530 eV. This spectrum feature belongs only to the O K edge signal corresponding to iron oxide nanoparticles. (f) Fe L₂₃ ratio map. (g) Fe L edge spectrum. The L₂₃ ratio has been obtained using the second derivative method.¹⁵ The L₂₃ ratio value (~ 5.5) is higher than that expected for Fe₃O₄ calculated using the same method (~ 5.1). It is known that the Fe L₂₃ ratio in γ -Fe₂O₃ is higher than in Fe₃O₄.¹⁶ (h) O K edge spectrum. The prepeak is indicated by an arrow.

The iron oxide content was assessed using inductively-coupled plasma optical emission spectrometry (ICP-OES). The results are shown in Table 3-3. The iron oxide content calculated from iron content analysed experimentally by ICP-OES agrees with the theoretical values calculated from the precursor amounts used for impregnation.

Table 3-3. Iron and iron oxide content in Fe₂O₃@LR and Fe₂O₃@SR obtained from ICP-OES compared with the values calculated from the amounts of precursors used for impregnation.

Sample ID	ICP-OES		Theoretical	
	Fe wt. %	Fe ₂ O ₃ wt. %	Fe wt. %	Fe ₂ O ₃ wt. %
Fe ₂ O ₃ @LR	10.6	15.1	10.0	14.3
Fe ₂ O ₃ @SR	10.5	15.0	10.0	14.3

Magnetic properties of maghemite-loaded MSR have been studied by magnetometry using a superconducting quantum interference device magnetometer (SQUID). Magnetic hysteresis loops recorded at room temperature (Figure 3-15) show a typical superparamagnetic behavior of the MSRs, characterized by a lack of coercivity. Such behavior is characteristic for small magnetic nanoparticles (typically below 14 nm in the case of maghemite) which contain a single magnetic domain.¹⁷ At room temperature and in the absence of a magnetic field, the magnetization can randomly flip. An external magnetic field magnetizes the particles and this effect is analogous to that of paramagnets but much stronger and saturation is achieved at significantly lower fields.

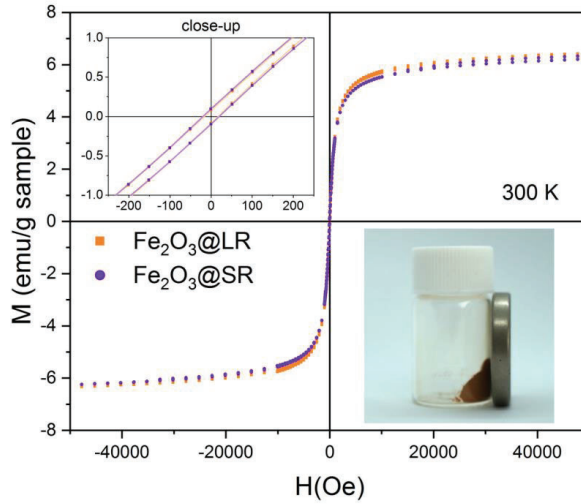


Figure 3-15. Magnetic hysteresis loops of $\text{Fe}_2\text{O}_3@LR$ and $\text{Fe}_2\text{O}_3@SR$ at 300K. Inset: Image of magnetic silica rods attracted by a magnet.

ZFC-FC measurements (Figure 3-16) showed similar blocking temperatures for both long and short magnetic MSRs (*circa* 40 K) and no separation between the ZFC and FC, indicating a similar magnetic character of both composites and no significant magnetic interactions.

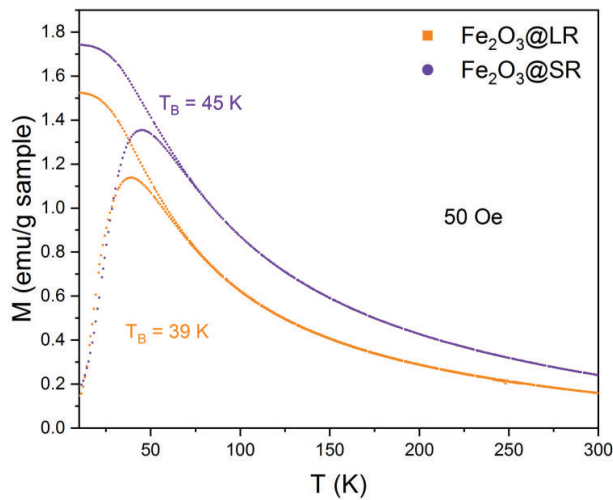


Figure 3-16. ZFC-FC curves of $\text{Fe}_2\text{O}_3@LR$ and $\text{Fe}_2\text{O}_3@SR$ measured at 50 Oe.

The saturation magnetization values at 300 K calculated in relation to the the mass of iron oxide (determined by ICP-OES) are listed in Table 3-4. The saturation magnetization value at 300 K is in the range reported in the literature for maghemite particles of similar sizes¹⁸ and lower than the 76 emu/g of bulk maghemite, measured at the same temperature.¹⁹

Table 3-4. Calculated saturation magnetization values of Fe₂O₃@LR and Fe₂O₃@SR at 300 K.

Sample ID	M_S (emu/g iron oxide)
Fe ₂ O ₃ @LR	43 ± 4
Fe ₂ O ₃ @SR	42 ± 4

The magnetic volume of the particles can be determined by fitting a branch of the $M(H)$ curve with the Langevin function $L(z)$:

$$M(H) \approx L(z) = M_S \left(\coth(z) - \frac{1}{z} \right)$$

Where M_S is the saturation magnetization $\coth(z)$ is the hyperbolic cotangent function of z :

$$z = \frac{H\mu}{k_B T}$$

Where μ is the magnetic moment of one particle, T is the temperature and k_B is the Boltzmann constant. The magnetic moment is determined from the fitting parameter and can be used to calculate the volume of one superparamagnetic nanoparticle V_M :

$$V_M = \frac{\mu}{\rho M_S} = \frac{\pi d^3}{6}$$

Where d is the mean magnetic particle diameter, and ρ is the density of maghemite (4.9 g/cm³).²⁰ The Langevin functions fitted to the magnetization curves are shown in Figure 3-17. It can be observed that for lower magnetic fields, the Langevin function fits the data accurately, but at increasing fields, the function starts to deviate from the data points. This observation of two regimes can be explained by the presence of a paramagnetic component, possibly from non-crystallized iron species, which has the effect of lowering the M_S . The fact that the saturation magnetization of MSRs was lower than in bulk maghemite can be also attributed to the canting of spins on the surface of small maghemite nanoparticles.²¹

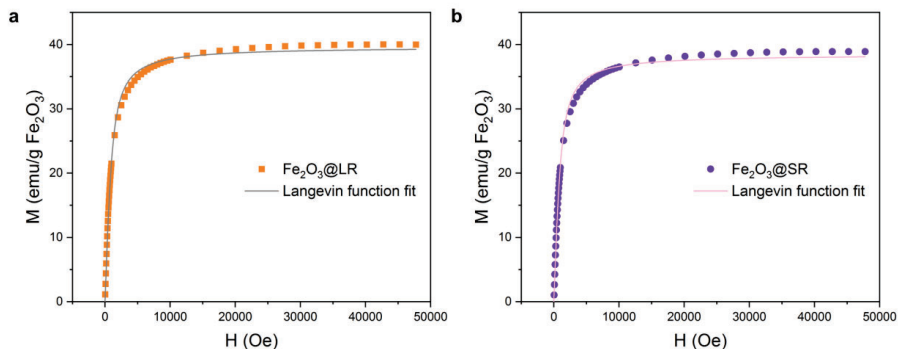


Figure 3-17. Langevin function fitted to magnetic hysteresis of (a) $\text{Fe}_2\text{O}_3@\text{LR}$ and (b) $\text{Fe}_2\text{O}_3@\text{SR}$. The contribution of the paramagnetic component has been removed by correcting the slope using a linear fit to the four data points at the highest magnetic fields.

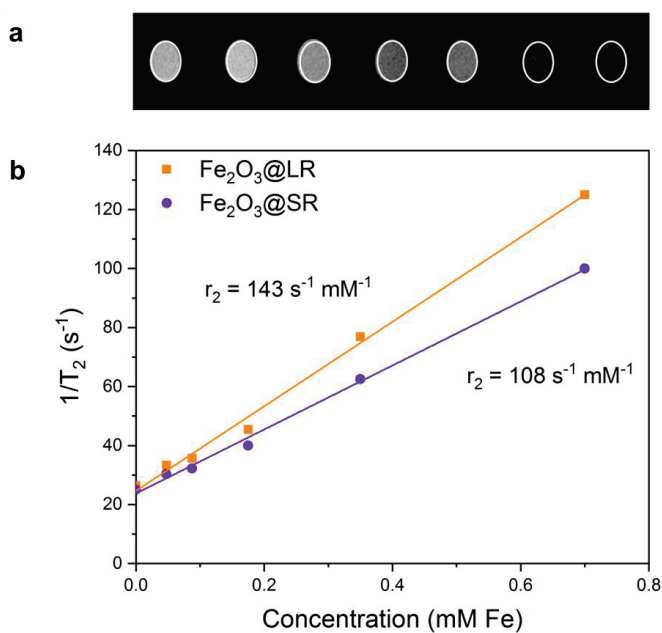
The maghemite particle diameter calculated from magnetic volume (approximately 9.5 nm for NPs inside both $\text{Fe}_2\text{O}_3@\text{LR}$ and $\text{Fe}_2\text{O}_3@\text{SR}$) is larger than the pore diameter measured by TEM or BET isotherm. This supports the TEM observations regarding the shape of the magnetic nanoparticles obtained after silica etching (elongated particles with a mean length of 6.9 nm measured by TEM). The particles are not spherical but rather ellipsoidal, as confinement inside the pores made them grow preferentially along the rod main axis. It should be noted that the growth of NPs across the pores was also observed, and it caused local deformations of the pore structure, breaking the periodicity of the channels.

3.2.3. MRI performance of magnetic silica rods

Next, the performance of the magnetic composites as T_2 MRI contrast agents was studied. Agarose phantoms containing different concentrations of particles ($\text{Fe}_2\text{O}_3@\text{LR}$ or $\text{Fe}_2\text{O}_3@\text{SR}$) were prepared at a series of concentrations and their MRI T_2 signal was recorded (Table 3-5). A decrease of the signal was observed as the concentrations of rods increased, for both long and short rods, and the inverse T_2 relaxation time presented a linear dependence on iron concentration in the composite (Figure 3-18 b). The signal decay of long rods was higher than that of short rods, which is illustrated by their slightly higher transverse relaxivity value at 7 T ($143 \text{ s}^{-1}\text{mM}^{-1}$ and $108 \text{ s}^{-1}\text{mM}^{-1}$, respectively).

Table 3-5. MRI T_2 relaxation times (expressed as T_2 , ms) of the MSR agarose phantoms at increasing concentrations.

Nanorods suspension		$\text{Fe}_2\text{O}_3@LR$	$\text{Fe}_2\text{O}_3@SR$
Agarose (wt. %)	Concentration (mM Fe)	T_2 (ms)	
4	0	38	40
4	0.044	30	33
4	0.088	28	31
4	0.175	22	25
4	0.350	13	16
4	0.700	8	10

**Figure 3-18.** (a) T_2 MRI signals of agarose phantoms with increasing concentrations of magnetic LR. (b) Evaluation of r_2 relaxivities of $\text{Fe}_2\text{O}_3@LR$ and $\text{Fe}_2\text{O}_3@SR$ ($n = 1$).

3.2.4. Application as self-propelled nanomotors

The characteristics of iron oxide loaded MSR also allowed us to induce their active motion, where chemical energy from the environment is converted into kinetic energy; an effect inspired by the motion of biological organisms. MSR have been used as self-propelled catalytic nanomotors in collaboration with the group of Prof. Samuel Sánchez at the *Institute for Bioengineering of Catalonia (IBEC)*. The motion of three systems was compared in presence of H_2O_2 as fuel: LR sputtered with platinum on one side, $Fe_2O_3@LR$ and $Fe_2O_3@LR$ sputtered with platinum on one side. The movement was induced by catalytic decomposition of H_2O_2 on platinum, by Fenton reactions on iron oxide nanoparticles, or by a combination of both. It was found that the presence of iron oxide NPs inside the rod channels alone is not enough to significantly induce enhanced motion, but it greatly improves the motion of platinum-coated rods by giving them directional propulsion (Figure 3-19). This effect has been explained by directionality stabilization by the inhibition of trajectory inversion, achieved by a jet-like expulsion of Fenton reaction products through the channels.

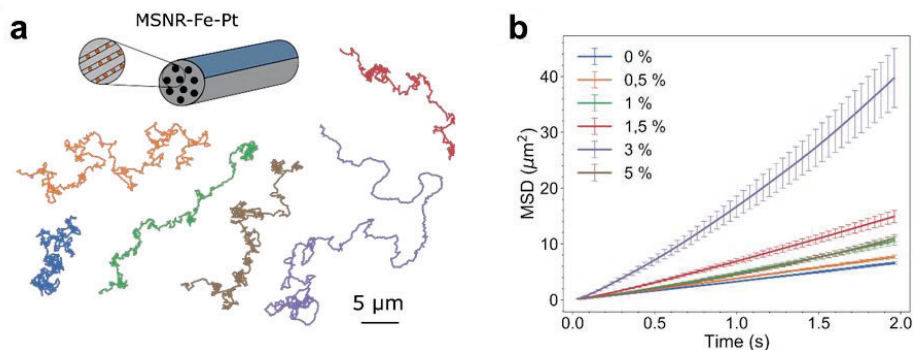


Figure 3-19. Motion of catalytic nanomotors. (a) Trajectories of $Fe_2O_3@LR$ sputtered with platinum, under different concentrations of H_2O_2 . (b) Mean squared displacements of the material, indicating greatly enhanced motion at 3% of fuel. At higher concentrations, it is possible that an inhibition mechanism related to increased reactivity takes place. This figure is obtained from *ChemNanoMat* (2021) by R. Mestre et al.²²

3.3. Evaluation of MSRs as US contrast agents

The performance of MSR as a contrast agent in another imaging modality – ultrasound imaging – was also investigated. It was assumed that hollow or partially filled channels could lead to a change in the acoustic properties and an increase in US contrast. LR and $Fe_2O_3@LR$ samples in a range of concentrations in water have been prepared and their performance as US contrast agents has been measured in a

preclinical US imaging scanner. Before preparing the dispersions of LR, moisture was removed by thermal treatment (200 °C, 3 h).

A stronger US signal was detected for $\text{Fe}_2\text{O}_3@\text{LR}$ compared to LR. (Figure 3-20 a) However, the registered ultrasound signal was lower than those observed for conventional microbubbles (Figure 3-20 b).

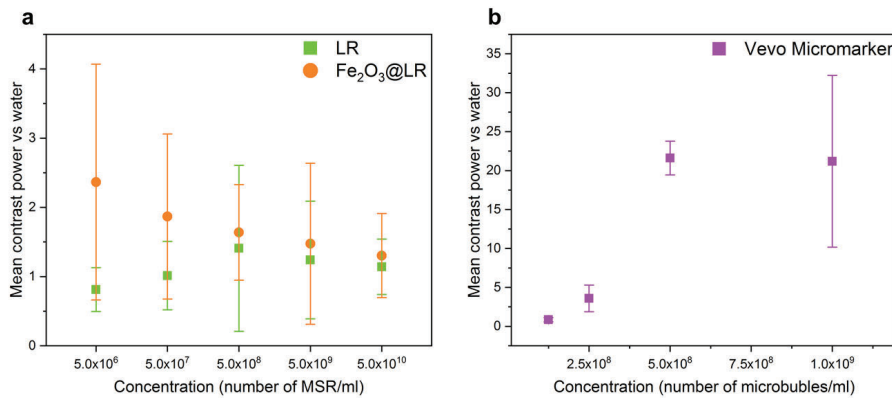


Figure 3-20. (a) US contrast mean power compared to water for different concentrations of LR and $\text{Fe}_2\text{O}_3@\text{LR}$, measured in triplicate. (b) US contrast mean power compared to water for different dilutions of commercially available microbubbles (Vevo Micromarker).

The results can be explained by the introduction of water into the pores of pure silica rods, which prevented the generation of air bubbles. In the case of iron oxide NP-loaded silica rods, the spaces between NPs are filled with air and are not penetrable by water. However, the overall performance of MSRs as ultrasound contrast agents is poor because of the relatively small diameter of the pores which is not enough for the generation of bubbles that would provide a contrast large enough to be considered an alternative to microbubbles.

3.4. Loading with ceria NPs for therapeutic purposes

As it was described in Chapter 1, cerium oxide offers great potential as a therapeutic agent in NAFLD due to its redox properties.^{23–25} The possibility of incorporating ceria into the MSRs has been investigated. Moreover, it was assessed whether both ceria and iron oxide nanoparticles can be simultaneously present inside the rods, forming a bimodal load for potential theranostic applications. The introduction of ceria inside the pores has been done similarly to loading with magnetic nanoparticles by wet impregnation method. For this purpose, cerium (III) nitrate hexahydrate

($T_m = 65\text{ }^\circ\text{C}$) was used as a precursor. Impregnation of pure LR at $80\text{ }^\circ\text{C}$ (30 min repeated twice, with mixing in between) resulted in filling of the pores with the cerium precursor (Table 3-6, Figure 3-21).

Table 3-6. Samples impregnated with cerium (III) nitrate hexahydrate. Thermal treatment: $600\text{ }^\circ\text{C}$, 3 h (Ar/H₂ 100 cm³/min).

Sample index	Silica : Ce : Fe precursors ratio (w/w)	Impregnation	Thermal treatment
LR-C1	1:1:0	LR impregnated with Ce precursor	-
LR-C1[R]	1:1:0	Sample LR-C1 after a thermal treatment	+
FeCe@LR-1	2:1:1	LR impregnated with a mix of precursors	+
FeCe@LR-2	3:1:1	LR impregnated with a mix of precursors	+
FeCe@LR-3	5:1:1	LR impregnated with a mix of precursors	+
Fe@Ce@LR	3:1:1	LR impregnated first with Ce and then Fe precursor	+
Ce@Fe@LR	3:1:1	LR impregnated first with Fe and then Ce precursor	+

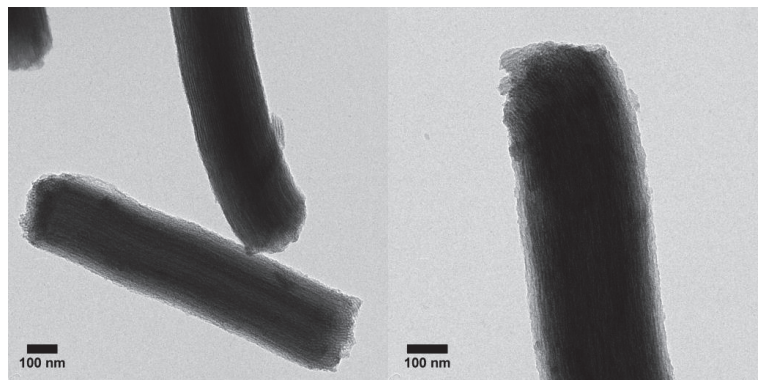


Figure 3-21. TEM images of LR impregnated with cerium (III) nitrate hexahydrate (sample LR-C1).

After performing a thermal treatment at $600\text{ }^\circ\text{C}$ in a reducing atmosphere, cerium (IV) oxide was formed, as confirmed by the presence of corresponding peaks in XRD diffraction (Figure 3-22).

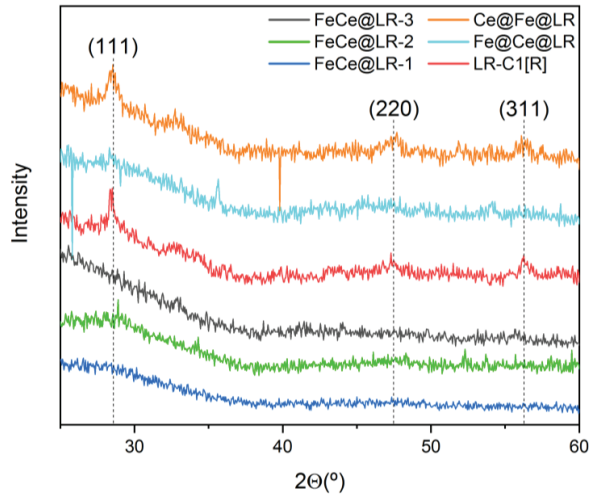


Figure 3-22. X-ray diffractogram of samples impregnated with cerium precursor, indexed in the cerium (IV) oxide unit cell.

It was intended to prepare rods loaded with both cerium oxide and iron oxide to obtain a material with potential use as a multimodal theranostic agent. For this purpose, silica rods were impregnated with a mixture of iron (III) nitrate nonahydrate and cerium (III) nitrate hexahydrate, which were previously ground thoroughly in a mortar. TEM images (Figure 3-23) of the samples prepared with different mass ratios between silica and the precursor mixture revealed that in some cases the material was deposited mostly on the surface of rods, and even though the loading was more effective in the sample FeCe@LR-2, the diffraction pattern indicated no presence of crystalline phases. This can be explained by the fact that no binary oxides containing iron and cerium are known to exist. Because the melt was formed by a homogeneous mixture of the two metal nitrates, no crystalline phase was able to form with the treatments at 600 °C.

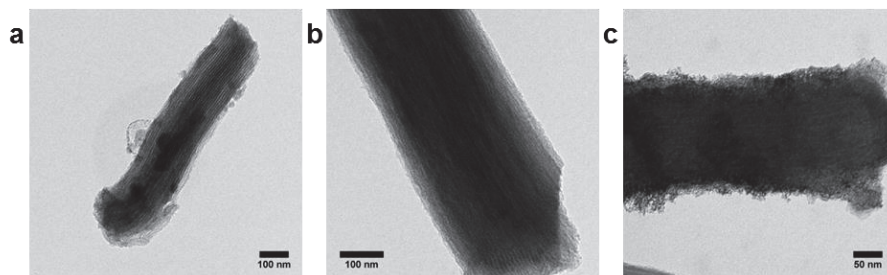


Figure 3-23. TEM images of (a) FeCe@LR-1, (b) FeCe@LR-2, (c) FeCe@LR-3.

Another trial was done by impregnating MSRs with one of the precursors, followed by a second impregnation with the other one. The rods impregnated first with cerium precursor and then with iron precursor (Sample Fe@Ce@LR) appeared as filled in the TEM images (Figure 3-24 a). It was also observed that the sample was magnetic. Magnetic measurements indicated superparamagnetic and paramagnetic contributions (Figure 3-24 c). However, electron diffraction (Figure 3-24 b) and XRD (Figure 3-22) did not reveal the presence of any crystalline phase formed within the rods.

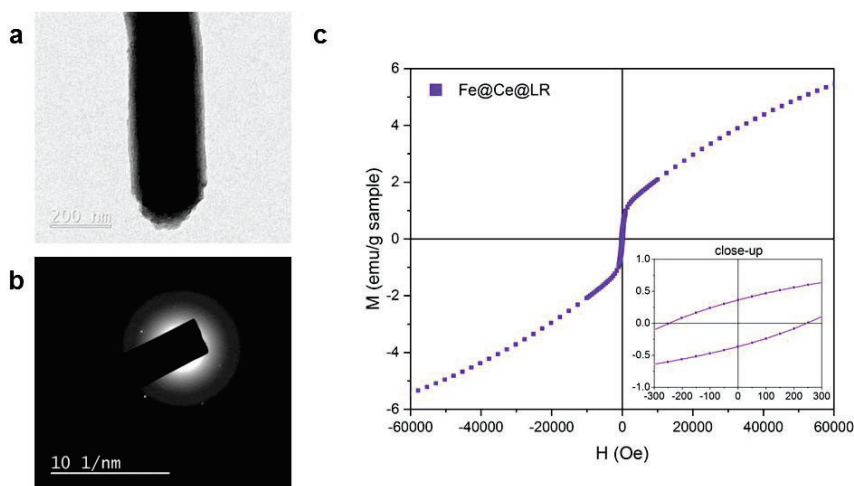


Figure 3-24. (a) TEM image of Fe@Ce@LR. (b) Corresponding electron diffraction pattern. (c) Magnetic hysteresis loop of the sample, acquired at 10K. Inset: magnification of the curve at low magnetic fields.

Magnetic properties of the sample can be explained by the presence of amorphous magnetic iron oxide, which has been reported in the literature.^{26,27}

To confirm the presence of both iron and cerium inside the pores and determine the oxidation state of cerium, EELS measurements have been performed (Figure 3-25). This analysis was performed by Dr. Jaume Gázquez (ICMAB) at the *ICTS National Center of Electron Microscopy at Universidad Complutense de Madrid*. It has been observed that both iron and cerium are co-localized inside the pores, following the channels. The ratio of cerium M_4 to M_5 peaks in EELS spectrum (located at 901 eV and 883 eV, respectively), with the intensity of M_4 larger than that of M_5 , is characteristic of Ce^{4+} .²⁸ This indicates that ceria is in form of CeO_2 and could be potentially used for capturing reactive oxygen species.

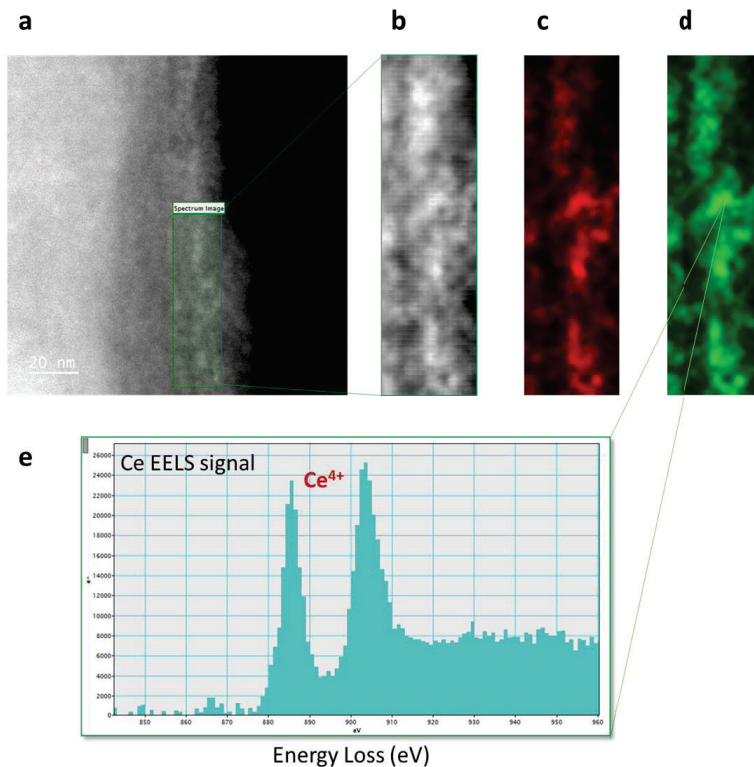


Figure 3-25. EELS spectrum at the Ce $M_{4,5}$ edge for Fe@Ce@LR. (a) Zeta contrast image of a single rod. (b) Annular Dark Field (ADF) image of the area highlighted in the zeta contrast image. (c) Iron map generated by integration of the signal of the Fe $L_{2,3}$ edge for each pixel in the spectrum image (SI). (d) Ce map generated by integration of the signal of the Ce edge for each pixel in the SI. (e) Ce EELS spectrum. The relative intensity of Ce M_4 and M_5 peaks resembles that of Ce^{4+} oxidation state.²⁸

3.5. Loading with potential CT contrast agents

Impregnation with chemical compounds containing elements of high atomic number that could be used as potential CT contrast agents was also attempted. The objective was to load large amounts of such compounds inside the pores, considering that a large amount is needed to provide enough CT contrast.

First, it was attempted to fabricate insoluble barium sulfate compounds inside the MSR pores. For this purpose, the MSRs were impregnated with a solution of barium chloride and subsequently, sodium sulfate was introduced. The barium compound was found only outside of the rods, in the form of large agglomerates (Figure 3-26 a).

Another trial involved the use of a gold precursor to load the pores with gold nanoparticles. After soaking the rods with the precursor solution, followed by cleaning the rods and centrifugation, a reducing agent – sodium borohydride – was used. As a result, only the surface of rods was covered with particles (Figure 3-26 b) and a small amount of clusters below 5 nm in diameter, less transparent to the electrons than silica and supposed to contain gold was found (Figure 3-26 c), but no defined lines in the diffraction pattern were observed.

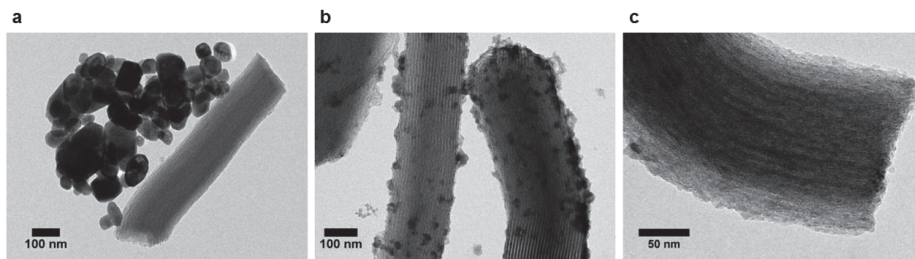


Figure 3-26. MSR after impregnation with (a) barium chloride, (b, c) hydrogen tetrachloroaurate (III) and subsequent reduction with borohydride.

The MSRs were also impregnated with bismuth compounds. Impregnation with bismuth (III) chloride led to partial loading of the MSR pores, as indicated by darker lines coinciding with the pores in TEM images (Figure 3-27 c) but large, elongated agglomerates attached to the silica surface were mostly observed (3-27 a, b).

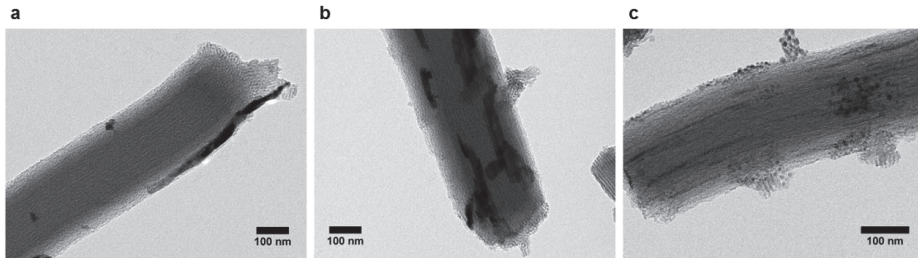


Figure 3-27. MSR after impregnation with bismuth (III) chloride.

MSRs were loaded with bismuth (III) bromide, which filled a relatively small percentage of available pores but formed continuous lines along the whole length of the rods (Figure 3-28). However, regardless of the precursor amount used, most of the bismuth compound was found outside of the rods as bismuth crystals. Due to the difficulty in the separation of the particles from MSR, this system was not considered optimal for the desired application as a CT contrast agent.

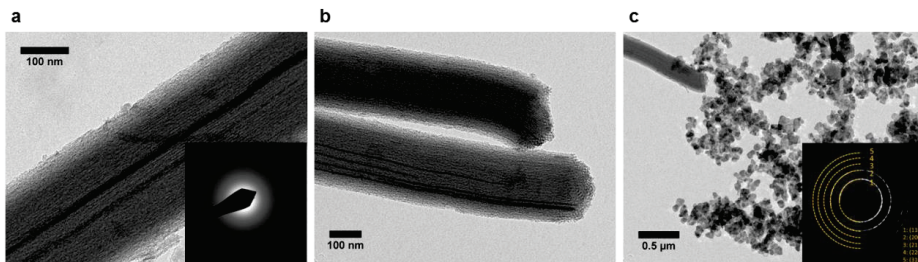


Figure 3-28. (a, b) MSR after impregnation with bismuth (III) bromide. Inset: corresponding electron diffraction pattern showing no rings. (c) Bismuth crystals found outside of the pores. Inset: Electron diffraction pattern of metallic bismuth.

Bismuth (III) nitrate pentahydrate was also tested as an impregnation precursor for its low melting point and similarity to other nitrates, which were successfully used for loading with different species such as iron oxide and cerium oxide. The rods were partially filled, even though the species did not extend along the whole pore length (Figure 3-29 a, b). However, most of the bismuth precursor did not enter the pores and was found as big particles the size of the rods (Figure 3-29 c).

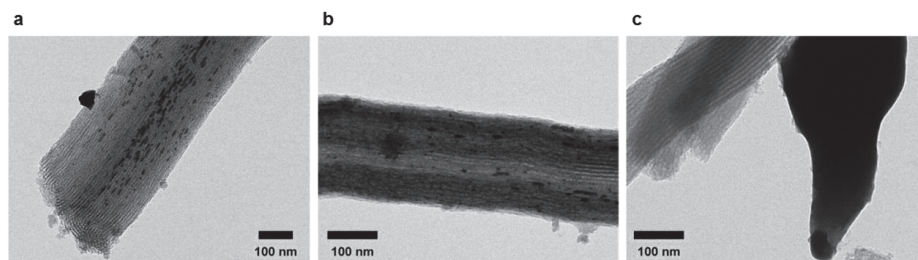


Figure 3-29. (a, b) MSR after impregnation with bismuth (III) nitrate pentahydrate. (c) Bismuth compound found outside the silica.

Impregnation with iron (III) nitrate and bismuth compounds was performed to obtain multifunctional materials. However, both simultaneous impregnation and subsequent impregnations with two metal precursors did not result in the coexistence of magnetic iron oxide and bismuth compounds inside the pores. The rods either contained only maghemite and no bismuth or were not magnetic.

3.6. Chapter summary

Mesoporous silica rods of two distinct aspect ratios (LR, SR) described in Chapter 2 have been successfully loaded with iron oxide nanoparticles by using a wet impregnation method followed by a single thermal treatment in reducing atmosphere. The presence of approximately 15 wt. % of nanoparticles composed of γ -Fe₂O₃ inside the channels has been confirmed using various techniques. The nanoparticles grew preferentially along the pores, taking ellipsoidal shapes. Growth in the direction across the pores resulted in local pore deformations and breaking of pore periodicity. The material demonstrated superparamagnetic properties with saturation magnetization similar to reported for maghemite nanoparticles of similar size.

MSRs loaded with iron oxide have been used as MRI phantoms and demonstrated a T₂ contrast agent-like behavior, with long rods displaying slightly higher relaxivity than short rods.

Moreover, cerium (IV) oxide has been loaded into MSR pores and multimodal magnetic rods containing both iron and cerium were fabricated although further optimization is needed.

MSRs have been studied as potential US contrast agents but their contrast power was significantly lower than for microbubbles used as a standard.

The possibility of loading MSRs with CT contrast agents using the same strategy has also been investigated but a satisfactory result was not achieved for various reasons. Barium compound could not be loaded inside the pores. Gold particles were either too small and too few to achieve the desired effect, or attached to the surface of silica rods. Bismuth compounds could be loaded inside the rods but were also found in large amount on the surface of rods. Moreover, multimodal contrast agents with both iron and bismuth compounds could not be formed.

Importantly, the rods have been also used as catalytic nanomotors powered by hydrogen peroxide, and iron oxide nanoparticles participated in inducing directional propulsion in platinum-coated rods.

Overall results indicate that the proposed system can combine multiple functions that may be beneficial for their potential use in theranostics.

3.7. Annex

3.7.1. Materials

Iron (III) nitrate nonahydrate, cerium (III) nitrate hexahydrate and sodium borohydride were purchased from ACROS Organics. Bismuth (III) nitrate pentahydrate, bismuth (III) chloride, bismuth (III) bromide, barium chloride, agarose, sodium hydroxide and sodium citrate were purchased from Sigma-Aldrich. Sodium sulfate was purchased from Labkem. Hydrogen tetrachloroaurate (III) was purchased from Alfa Aesar. The purity of all reagents was 98% or higher.

3.7.2. Synthesis of maghemite nanoparticles inside silica mesopores

The impregnation of mesoporous silica rods consisted of mixing the silica powder with iron (III) nitrate nonahydrate. To induce capillary action, it was made sure that the volume of the iron precursor $\left(V_{Fe(NO_3)_3 \cdot 9H_2O} = \frac{m_{Fe(NO_3)_3 \cdot 9H_2O}}{\rho_{Fe(NO_3)_3 \cdot 9H_2O}} \right)$ was not larger than the volume of the pores (calculated from BET isotherm; 0.65 cm³/g for LR, 0.79 cm³/g for SR). In a typical impregnation experiment, the powders were mixed at a ratio of 1:1 wt./wt. Iron (III) nitrate nonahydrate was ground in a mortar, weighed and added to a vial containing MSRs. The two powders were mixed thoroughly with a spatula and the vial was put in a silicone oil bath at 60 °C. After 30 minutes, the powders were mixed again. This step was performed twice. After another 30 minutes of heating, the powder was cooled down. Then, the impregnated silica was heated in a furnace (ST 1002540, HOBERSAL) at 425 °C for 3 hours under a flow of argon with 5% of hydrogen (100 cm³/min).

3.7.3. Synthesis of cerium oxide nanoparticles inside silica mesopores

The MSR powder was mixed with cerium (III) nitrate hexahydrate (1:1 wt./wt.). The cerium precursor was ground in a mortar, weighed and added to a vial containing MSRs. The two powders were mixed thoroughly with a spatula and the vial was put in a silicone oil bath at 80 °C. After 30 minutes, the powders were mixed again. This step was performed twice. After another 30 minutes of heating, the powder was cooled down. Then the impregnated silica was heated in a furnace (ST 1002540, HOBERSAL) at 600 °C for 3 hours under a flow of argon with 5% of hydrogen (100 cm³/min).

3.7.4. MSR loading with iron and cerium compounds

The MSR powder was mixed with cerium (III) nitrate hexahydrate (3:1 wt./wt.). The cerium precursor was ground in a mortar, weighed and added to a vial containing MSRs. The two powders were mixed thoroughly with a spatula and the vial was put in a silicone oil bath at 80 °C. After 30 minutes, the powders were mixed again. This

step was performed twice. After another 30 minutes of heating, the powder was cooled down. Then, iron (III) nitrate nonahydrate ground in a mortar was added ($m_{\text{iron precursor}} = m_{\text{cerium precursor}}$). The powders were mixed thoroughly and the vial was put in a silicone oil bath at 60 °C. After 30 minutes, the powders were mixed again. This step was performed twice. After another 30 minutes of heating, the powders were cooled down. The impregnated MSR were heated in a furnace (ST 1002540, HOBERSAL) at 600 °C for 3 hours under a flow of argon with 5% of hydrogen (100 cm³/min).

3.7.5. MSR loading with gold compound

15 µl of HAuCl₄ aqueous solution (0.1-1.0 mM) were added to 20 mg of MSR powder. The powder was then either heated overnight at 100 °C or 15 µl of 10⁻⁵ M NaBH₄ were added and the powder was dried at 70 °C. Then the rods were washed three times by dispersing in water and centrifuging at 116 x g.

3.7.6. MSR loading with barium compound

10 µl of 0.5 M BaCl₂ aqueous solution were added to 15 mg of MSR powder. After drying the powder at 50 °C, 10 µl of 0.5 M Na₂SO₄ aqueous solution were added. The powder was dried at 50 °C and then washed three times by dispersing in water and centrifuging at 116 x g.

3.7.7. MSR loading with bismuth compounds

(a) The MSR powder was mixed with bismuth (III) bromide or bismuth (III) chloride (2:1, 3:1, or 5:1 wt./wt.). The bismuth precursor was ground in a mortar, weighed and added to a vial containing MSRs. The two powders were mixed thoroughly with a spatula and the vial was put in a silicone oil bath at 245 °C for 30-60 min. Alternatively, the powders were placed in a furnace (ST 1002540, HOBERSAL) at 425 °C for 3 hours under a flow of argon with 5% of hydrogen (100 cm³/min).

(b) The MSR powder was mixed with bismuth (III) nitrate pentahydrate (1:1, 2:1, or 3:1 wt./wt.). The bismuth precursor was ground in a mortar, weighed and added to a vial containing MSRs. The two powders were mixed thoroughly with a spatula and the vial was put in a silicone oil bath at 60 °C for 60 min. Then, the powder was placed in a furnace (ST 1002540, HOBERSAL) at 425 °C for 3 hours under a flow of argon with 5% of hydrogen (100 cm³/min).

3.7.8. Silica etching

5 mg iron oxide-loaded MSRs were dispersed in 10 ml aqueous solution of sodium hydroxide (12 M). The dispersion was heated to 80°C and kept under stirring for 4 days. Then the mixture was centrifuged (4192 x g, 10 min) and magnetically

separated three times. Then the particles were dispersed in an aqueous solution of sodium citrate (1%) and ultrasonicated.

3.7.9. X-ray diffraction

A Siemens D-5000 diffractometer in Bragg-Brentano geometry with conventional X-ray source (Cu K α radiation, with $\lambda K\alpha = 1.5406 \text{ \AA}$) was used for X-ray diffraction measurements which were analysed by Rietveld refinement using the Materials Using Diffraction (MAUD) software.²⁹

3.7.10. Transmission electron microscopy (TEM)

The loading of MSRs with iron oxide nanoparticles was examined by a JEOL 1210 transmission electron microscope (TEM) operating at 120 kV accelerating voltage. Selected area electron diffraction was used to study the phase and orientation of the magnetic particles, and was performed using the same equipment. Samples for TEM analysis were prepared by drop-casting ethanol dispersions of the particles (1 mg/ml) on TEM copper grids.

3.7.11. Scanning transmission electron microscopy (STEM) with electron energy loss spectroscopy (EELS)

The STEM/EELS measurements were performed by Dr. Jaume Gázquez (ICMAB) at the *ICTS National Center of Electron Microscopy at Universidad Complutense de Madrid*. Samples were characterized using a JEOL JEM ARM200cF operated at 200 kV equipped with a CEOS aberration corrector and with a Gatan Quantum energy filter spectrometer for EELS measurements. The STEM microscopes were operated in high angle annular dark-field (HAADF) imaging mode, also referred to as Z-contrast because the brightness associated to each atomic column of the images scales with its atomic number.³⁰ The samples were prepared by dispersing the samples in ethanol and depositing a droplet of the suspension on a holey carbon film supported on a copper grid.

3.7.12. Magnetometry (SQUID)

Room temperature magnetic hysteresis loops were collected by a superconducting quantum interference magnetometer device (SQUID, Quantum Design Inc.) with a maximum applied field of 50 kOe. The temperature dependence of the magnetization (M-T) under a dc field of 50 Oe was recorded on heating at 2 K/min in zero-field-cooled (ZFC) and field-cooled (FC) conditions in 10–300 K temperature range using the same magnetometer.

3.7.13. Elemental analysis by inductively-coupled plasma emission spectrometry (ICP-OES)

The iron content in the samples was determined by ICP-OES. The experiments were performed at the chemical analysis service at *Universitat Autònoma de Barcelona*. Approximately 1 mg of sample (weighed on MX5 microbalance, Mettler Toledo) was digested with a mixture of concentrated HCl and HNO₃ in a microwave oven. The resulting digestions were diluted with 1% HCl (v/v) and introduced into an ICP-OES spectrometer (Perkin-Elmer, model Optima 4300DV) for the measurement.

3.7.14. Energy-dispersive X-ray spectroscopy (EDX)

Chemical composition of the samples was investigated by energy-dispersive X-ray analysis (EDX) in a FEI Quanta 200 FEG scanning electron microscope (SEM) with a field emission gun operating at 15 kV. EDX mapping was performed with a Magellan 400L Field Emission Scanning Electron Microscope with attached X-Max Ultim Extreme EDX (Oxford Instruments).

3.7.15. Small angle X-ray spectroscopy (SAXS)

SAXS measurements were performed using Bruker D8-Discover in 2 θ range from 0.15 to 5 degrees in steps of 0.02 with CuK α radiation. A lead plate was placed perpendicular to the sample plane, slightly above it, held with a specific support designed on purpose to minimize the background at the detector.

3.7.16. MRI studies

The MRI studies on phantoms were performed by Dr. Fernando Herranz (*Institute of Medical Chemistry, IQM-CSIC, Madrid*). The MRI equipment used in this study was an Agilent/Varian scanner (Agilent, Santa Clara, CA) equipped with a DD2 console and an actively shielded 205/120 gradient insert coil with 130 mT m⁻¹ maximum gradient strength, a TX/RX volume quadrature coil, and a 1H circularly polarized transmit–receive volume coil of 35 mm inner diameter and 30 mm active length built by Neos Biotec (Pamplona, Spain). The scans were performed at 7 T.

3.7.17. Motion studies of MSR-based nanomotors

The studies of motion dynamics of MSR-based systems were performed at the *Institute for Bioengineering of Catalonia (IBEC)* in collaboration with the group of Prof. Samuel Sánchez. LR and Fe₂O₃@LR were used in the experiments. Pt coatings were deposited on the two types of MSRs by adding 50 μ l of a 2 mg/ml water dispersion of each type of MSR on a glass slide (24 x 24 mm) kept at 45°, previously cleaned with acetone and isopropanol and treated with oxygen plasma. After drying of MSRs, Pt was sputtered on the exposed side of the MSRs using a Leica EM

ACE600 sputter coater, at a rate of 0.4 nm/s, with a working distance of 45 mm and a current of 35 mA. A thickness of 10 nm of sputtered Pt was achieved.

The motion of MSR-based nanomotors was performed with an optical inverted microscope (Leica DMI8), equipped with a 63x water immersion objective (NA = 1.2). A concentrated dispersion of nanomotors was diluted in 1 ml of water. Then, a drop of this solution was mixed in a 1:1 ratio with a H₂O₂ solution to achieve final concentrations of 0%, 0.5%, 1%, 1.5%, 3% and 5% (v/v), and the final solution was placed in a glass coverslip under the microscope. Several videos of 30 s at 25 frames per second (FPS) were recorded for each condition. The trajectories of the particles were obtained with a previously available home-made tracking software based on Python that locates and tracks the particles based on computer vision techniques, returning the positions of the particles with time.³¹ For each of the conditions of nanomotors and fuel concentration, a sample size between N = 50 - 150 was used. The 2D-projected mean squared displacement (MSD) was computed from the trajectories of the particles in time (x(t),y(t)):

$$\text{MSD}(\Delta t) = \langle (x(t_0 + \Delta t) - x(t_0))^2 \rangle + \langle (y(t_0 + \Delta t) - y(t_0))^2 \rangle$$

where $\langle \cdot \rangle$ represents ensemble and time average, t_0 is the initial time and Δt is the elapsed time.

3.7.18. US studies

Ultrasound imaging studies have been performed by the company *Ephoran Multi Imaging Solutions S.r.l.* (via Ribes 5, 10010 Colleretto, Giacosa (TO), Italy). Phantoms were prepared from dispersions of MSR at different concentrations in water that were put in a rectangular plastic box equipped with three polyethylene tubes passing through the mould. At the end of each tube, needles were placed to facilitate the loading of the contrast agents. The agar phantom (2% wt./v. in MilliQ water) was prepared by heating the agar solution until complete dissolution of the agar, then the solution was poured in the mould and refrigerated at 4 °C for at least a night. The ultrasound instrument used for measurements was the VevoLAZR 2100 from Visualsonics, Toronto, Canada. It was characterized by a broadband ultrasound frequency of 13 MHz-24 MHz. To register the ultrasound signal, the solutions of the test item were loaded in polyethylene tubes. The ultrasound frequency was set to 21 MHz and the US gain was 18 dB. An acoustic gel was used as coupling agent between the ultrasound transducer and the phantom. For each phantom, a polyethylene tube filled with water was set as reference. Ultrasound image analysis was performed with VevoLAB software package (Visualsonics, Toronto, Canada). Regions of interest (ROIs) were selected by the operator over the acquired ultrasound images of the phantom. The signal within the ROIs was determined automatically by the software and reported as US average.

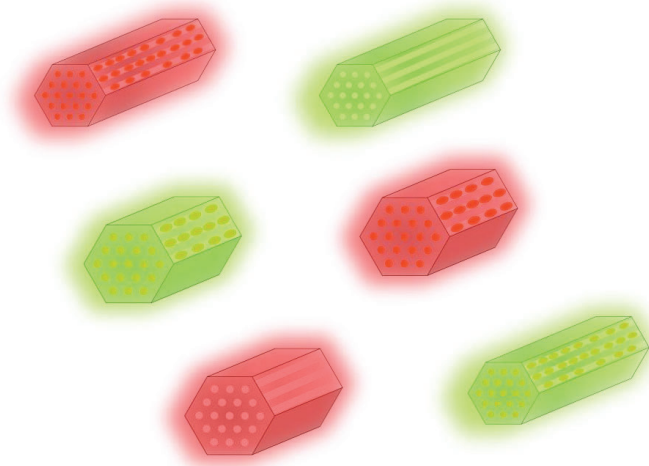
3.8. Chapter references

1. Shen, Z., Wu, A. & Chen, X. Iron Oxide Nanoparticle Based Contrast Agents for Magnetic Resonance Imaging. *Mol. Pharm.* **14**, 1352–1364 (2017).
2. Vangijzegem, T., Stanicki, D. & Laurent, S. Magnetic iron oxide nanoparticles for drug delivery: applications and characteristics. *Expert Opin. Drug Deliv.* **16**, 69–78 (2019).
3. Geppert, M. & Himly, M. Iron Oxide Nanoparticles in Bioimaging – An Immune Perspective. *Front. Immunol.* **12**, 688927 (2021).
4. Leslie-Pelecky, D. L. & Rieke, R. D. Magnetic Properties of Nanostructured Materials. *Chem. Mater.* **8**, 1770–1783 (1996).
5. Casas, L. *et al.* Iron oxide nanoparticles hosted in silica aerogels. *Appl. Phys. A Mater. Sci. Process.* **74**, 591–597 (2002).
6. Moreno, E. M. *et al.* Preparation of Narrow Size Distribution Superparamagnetic γ -Fe₂O₃ Nanoparticles in a Sol-Gel Transparent SiO₂ Matrix. *Langmuir* **18**, 4972–4978 (2002).
7. Tao, C. & Zhu, Y. Magnetic mesoporous silica nanoparticles for potential delivery of chemotherapeutic drugs and hyperthermia. *Dalt. Trans.* **43**, 15482 (2014).
8. Martín-Saavedra, F. M. *et al.* Magnetic mesoporous silica spheres for hyperthermia therapy. *Acta Biomater.* **6**, 4522–4531 (2010).
9. Li, J. G. *et al.* Alignment under Magnetic Field of Mixed Fe₂O₃/SiO₂ Colloidal Mesoporous Particles Induced by Shape Anisotropy. *Small* **12**, 5981–5988 (2016).
10. Li, J., Fornasieri, G., Bleuzen, A., Gich, M. & Impéror-Clerc, M. Epsilon-Fe₂O₃ Nanocrystals inside Mesoporous Silicas with Tailored Morphologies of Rod, Platelet and Donut. *ChemNanoMat* 1168–1176 (2018).
11. Eggenhuisen, T. M., Breejen, J. P. Den, Verdoes, D., de Jongh, P. E. & de Jong, K. P. Fundamentals of Melt Infiltration for the Preparation of Supported Metal Catalysts. The Case of Co/SiO₂ for Fischer-Tropsch Synthesis. *J. Am. Chem. Soc.* **132**, 18318–18325 (2010).
12. Ngene, P., Adelhelm, P., Beale, A. M., de Jong, K. P. & de Jongh, P. E. LiBH₄/SBA-15 Nanocomposites Prepared by Melt Infiltration under Hydrogen Pressure: Synthesis and Hydrogen Sorption Properties. *J. Phys. Chem. C* **114**, 6163–6168 (2010).
13. NIST Inorganic Crystal Structure Database, NIST Standard Reference Database Number 3, National Institute of Standards and Technology, Gaithersburg MD, 20899.
14. Zhao, D. *et al.* Triblock Copolymer Syntheses of Mesoporous Silica with Periodic 50 to 300 Angstrom Pores. *Science* **279**, 548–552 (1998).
15. Salafranca, J. *et al.* Surfactant Organic Molecules Restore Magnetism in Metal-Oxide Nanoparticle Surfaces. *Nano Lett.* **12**, 2499–2503 (2012).
16. Colliex, C., Manoubi, T. & Ortiz, C. Electron-energy-loss-spectroscopy near-edge fine structures in the iron-oxygen system. *Phys. Rev. B* **44**, 11402–11411 (1991).
17. Coey, J. M. D. *Magnetism and Magnetic Materials*. (Cambridge University Press, 2010).
18. Coduri, M. *et al.* Local Structure and Magnetism of Fe₂O₃ Maghemite Nanocrystals: The Role of Crystal Dimension. *Nanomaterials* **10**, (2020).
19. Cao, D. *et al.* High saturation magnetization of γ -Fe₂O₃ nanoparticles by a facile one-step synthesis approach. *Sci. Rep.* **6**, 32360 (2016).
20. Lucas, I., S., D.-V., Dubois, E., Chevalet, J. & Turq, P. Surface Charge Density of

- Maghemite Nanoparticle : Role of Electrostatics in the Proton Exchange. *J. Phys. Chem. C* **111**, pp.18568 (2007).
21. Morales, M. P. *et al.* Surface and Internal Spin Canting in γ -Fe₂O₃ Nanoparticles. *Chem. Mater.* **11**, 3058–3064 (1999).
 22. Mestre, R. *et al.* Nanorods Based on Mesoporous Silica Containing Iron Oxide Nanoparticles as Catalytic Nanomotors: Study of Motion Dynamics. *ChemNanoMat* **7**, 134–140 (2021).
 23. Kobylak, N. *et al.* Cerium dioxide nanoparticles possess anti-inflammatory properties in the conditions of the obesity-associated NAFLD in rats. *Biomed. Pharmacother.* **90**, 608–614 (2017).
 24. Parra-Robert, M. *et al.* Beyond the Scavenging of Reactive Oxygen Species (ROS): Direct Effect of Cerium Oxide Nanoparticles in Reducing Fatty Acids Content in an In Vitro Model of Hepatocellular Steatosis. *Biomolecules* **9**, (2019).
 25. Parra-Robert, M. *et al.* Mesoporous silica coated CeO₂ nanozymes with combined lipid-lowering and antioxidant activity induce long-term improvement of the metabolic profile in obese Zucker rats. *Nanoscale* **13**, 8452 (2021).
 26. Machala, L., Zboril, R. & Gedanken, A. Amorphous Iron(III) Oxide-A Review. *J. Phys. Chem. B* **111**, 4003–4018 (2007).
 27. van Diepen, A. M. & Popma, T. J. A. MÖSSBAUER EFFECT AND MAGNETIC PROPERTIES OF AN AMORPHOUS Fe₂O₃. *J. Phys. Colloq.* **37**, pp.C6-755-C6-758 (1976).
 28. Turner, S. *et al.* High resolution mapping of surface reduction in ceria nanoparticles. *Nanoscale* **3**, 3385 (2011).
 29. Lutterotti, L., S., M. & Wenk, H.-R. MAUD (Material Analysis Using Diffraction): a user friendly Java program for Rietveld Texture Analysis and more. *Proceeding Twelfth Int. Conf. Textures Mater.* **1**, 1599 (1999).
 30. Nellist, P. D. & Pennycook, S. J. Incoherent imaging using dynamically scattered coherent electrons. *Ultramicroscopy* **78**, 111–124 (2008).
 31. Ma, X., Hortelao, A. C., Miguel-López, A. & Sánchez, S. Bubble-Free Propulsion of Ultrasmall Tubular Nanojets Powered by Biocatalytic Reactions. *J. Am. Chem. Soc.* **138**, 13782–13785 (2016).

Chapter 4

Surface functionalization of silica rods and conjugation of fluorophores



4.1. Introduction

Besides having channels that allow loading with different chemical species, as described in Chapter 3, an additional advantage of mesoporous silica is the possibility of modifying its surface chemistry. The surface of the as-prepared silica is rich in silanol groups that can be modified using various strategies. This aspect is important for two reasons. First, it has been proven that the surface chemistry of a nanomaterial can affect the material's biomedical performance.^{1,2} Moreover, additional functional moieties can be introduced to the material, acting as targeting ligands or imaging contrast agents.³⁻⁵

In this chapter, a protocol for amino-functionalization of MSR surface has been developed and the effectiveness of the process has been confirmed by various characterization techniques. Then, the rods have been modified with fluorophores with emission wavelengths in different spectral ranges. MSRs with different surface charges, as well as fluorescent rods are then used in the next chapter for *in vitro* and *in vivo* trials.

4.2. Aminofunctionalization of silica rods

4.2.1. Introduction

One of the most commonly used surface modifications of mesoporous silica particles is the introduction of amine groups (amino-silanization). Amines are more reactive than silanol groups and allow the attachment of fluorophores or biomolecules. Amino-silanization is usually performed using (3-aminopropyl)triethoxysilane (APTES), due to its low cost and good coupling effectiveness.⁶ APTES is a silane consisting of three ethoxide groups and an aminopropyl group (Figure 4-1). In the presence of water, the ethoxide groups hydrolyse and form siloxane bonds with the silanols present on the silica surface.

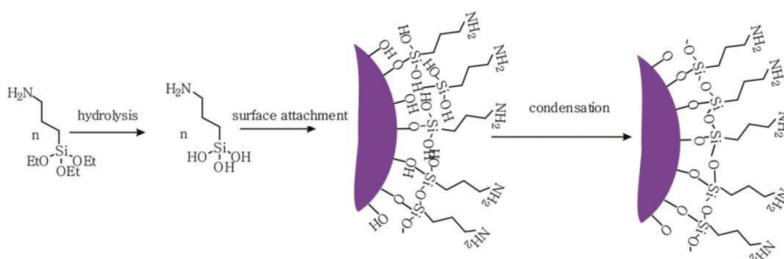


Figure 4-1. General mechanism of APTES functionalization by grafting. The ethoxide groups are hydrolysed. Free silanol groups attach covalently to the silanol groups on the silica surface, forming siloxane bonds. Further condensation occurs between neighboring silanol groups on the surface. This figure is adapted from *Langmuir* (2013) by Y. Liu et al.⁷

In general, surface functionalization with silanes can be achieved by two strategies: co-condensation and post-synthetic grafting.⁸ Co-condensation is a one-step process where an organoalkoxysilane is mixed with alkoxysilanes during the formation of a sol-gel matrix. Grafting is carried out once the synthesis of mesoporous silica has been completed and involves a reaction with an organoalkoxysilane that ends up covering the material surface. In this work, post-synthesis modification was explored, as the addition of APTES in a co-condensation method was found to alter the overall morphology of silica particles and it was difficult to optimize the parameters. The grafting method is more convenient because it can be used on already characterized rods essentially without changing their morphology, whether the rods are empty or filled with nanoparticles. This allows comparing rods of the same sizes with different surface charges and makes it possible to add new modalities to already functional rods by adapting the surface chemistry for further modification.

4.2.2. MSR functionalization and characterization

First MSR surface functionalization trials were performed under the conditions described in Table 4-1. A general protocol involved dispersing MSRs in a solvent and adding APTES at a given temperature under stirring (LR were used in all syntheses for comparison). After the reaction, the product was washed in ethanol and centrifuged three times. The precipitate was collected and dried in air.

Table 4-1. Aminofunctionalization conditions and post-functionalization characterization. The sample marked with an asterisk was subjected to a post-grafting thermal treatment (120 °C in air, for 2 h).

Sample ID	Temperature (°C)	Time (h)	Solvent	[APTES] (μl/ml)	Zeta potential (mV)	TEM observations
LR-N1	25	24	EtOH	10	-23	-
LR-N2	70	24	EtOH	20	-2	-
LR-N3	70	24	H ₂ O	20	-5	etched silica
LR-N4	70	1	H ₂ O	20	17	etched silica
LR-N5	70	1	H ₂ O	6	-12	-
LR-N6	70	24	EtOH:H ₂ O (70:30)	6	15	-
LR-N7 *	70	1	EtOH:H ₂ O (70:30)	6	33	-

A quick way to confirm the change of surface chemistry, in this case from silanol groups to amine groups, is by measuring the effective surface charge of the particles

(zeta potential). Silanol terminated MSRs are characterized by a negative zeta potential (-34 ± 4 mV for both LR and SR). A successful functionalization should result in a switch of zeta potential to high positive values, indicating that the rod surface is covered by amines carrying a positive charge.

The initial functionalization protocols did not show a successful surface modification for different reasons. It was observed that room temperature synthesis did not favor the attachment of APTES, as it was reflected by negative zeta potential (sample LR-N1). This can be explained by the low mobility of silanes and the lower probability of condensation reaction in those conditions.⁹ It has already been shown in the literature that higher temperatures can minimize undesired weak interactions such as the formation of hydrogen bonds, as well as changes in the kinetics of the reaction, resulting in lower times needed to reach the equilibrium.^{9,10} On the other hand, exposure of silica to high APTES concentrations (very basic pH) and high temperature lead to silica matrix etching and decomposition of the rods (Figure 4-2), even at short reaction times (LR-N3, LR-N4).

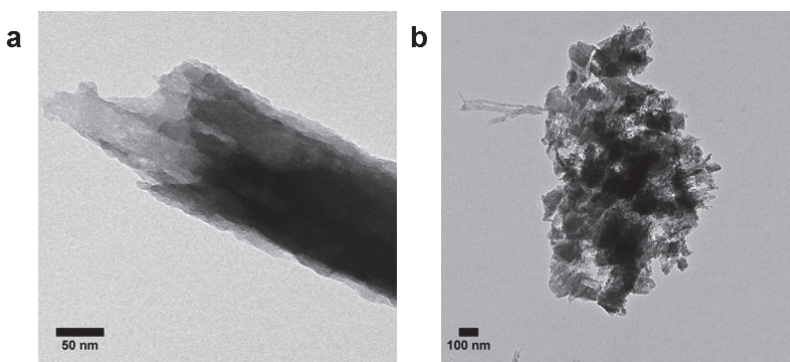


Figure 4-2. TEM images of APTES-functionalized samples. (a) LR-N3, (b) LR-N7.

The effect of solvent was also taken into account. In absence of water, the ethoxide groups are not hydrolysed and the siloxane bonds are formed through a nucleophilic substitution reaction, which is slower and less likely to produce a dense coating.¹¹⁻¹⁴ In contrast, an excess of water can result in uncontrolled polymerization in solution, generating oligomers and aggregates that are deposited on the surface through physisorption.^{14,15} To address these problems, a balance between these two effects has to be maintained. A 70:30 (v/v) ratio of ethanol to water has been used for further syntheses. The concentration of APTES was kept at 6 $\mu\text{l/ml}$ to prevent silica degradation and the temperature was set to 70°C. At these conditions, efficient functionalization could occur for reaction times as short as 1 h. However, to achieve high and stable coverage with aminosilanes, an additional modification of the

protocol has been applied. A *post-curing* thermal treatment was performed after the reaction with aminosilane. It has been reported that this thermal treatment helps to evaporate the physisorbed aggregates and causes the reorganization of the aminosilane chains, favoring the formation of siloxane bonds on the surface and increasing the stability of the coating.¹⁶⁻¹⁹ Zeta potential of the post-cured sample was larger than in all previous attempts, indicating a higher surface coverage with APTES.

As a result of performing the protocol described for LR-N7, a shift of zeta potential to positive values was observed for both short and long rods loaded with iron oxide NPs (Figure 4-3). The surface charge value was re-measured at 24 h and 48 h and remained unchanged. Moreover, TEM images showed that the structure of MSRs remained intact.

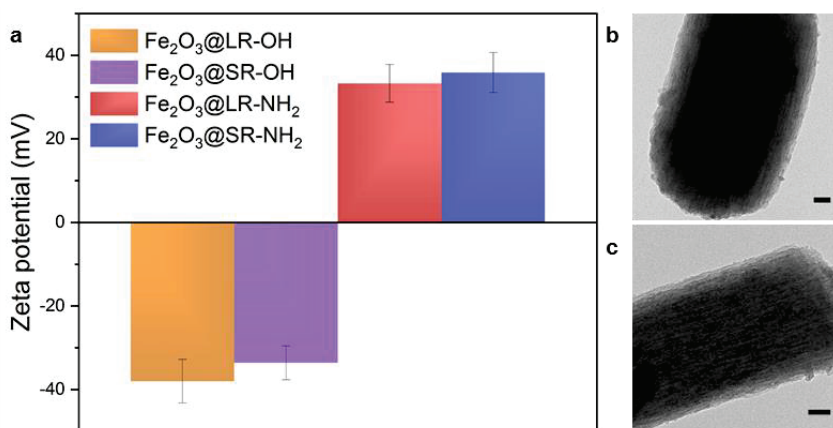


Figure 4-3. Zeta potential values before and after the functionalization. TEM images of MSRs after APTES functionalization using the final protocol. Scale bars: 50 nm.

Successful functionalization was confirmed by Fourier transform infrared spectroscopy (FT-IR) (Figure 4-4). The bands corresponding to Si-O-Si symmetric stretching at 805 cm⁻¹ and Si-O-Si asymmetric stretching at 1090 cm⁻¹ were observed in samples both before and after functionalization, suggesting that the main structure of silica was not affected by the modification. Bands at 1610-1643 cm⁻¹ observed in the functionalized silica correspond to -NH₂ in-plane scissoring in the amine groups²⁰, while bands at 2851 cm⁻¹ and 2920 cm⁻¹ indicate -CH₂ symmetric and asymmetric stretching vibrations from the propyl branch of APTES.²¹ The positions of the bands are indicative of a dense packing of the propyl chains.⁹ An asymmetric -CH₃ mode at 2962 cm⁻¹ may suggest that some ethoxide groups have not been fully hydrolysed and that the APTES molecules are not fully bonded with each other.^{9,20}

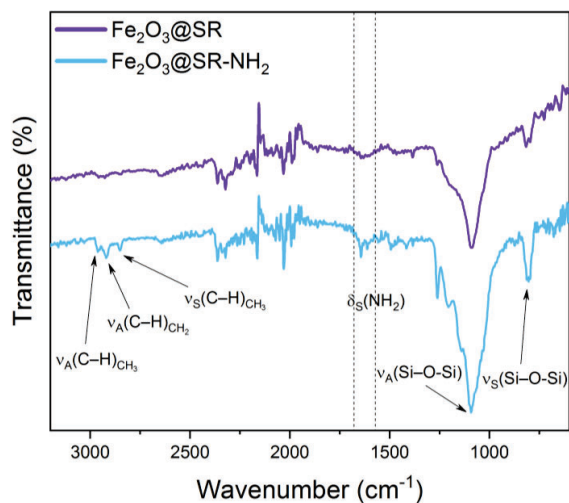


Figure 4-4. FT-IR spectra of iron oxide loaded MSRs ($\text{Fe}_2\text{O}_3@SR$) before and after surface functionalization.

The presence of $-\text{NH}_2$ groups on the MSR surface was additionally investigated qualitatively and semi-quantitatively by X-ray photoelectron spectroscopy (XPS). A general scan was performed for both $\text{Fe}_2\text{O}_3@LR-\text{NH}_2$ and $\text{Fe}_2\text{O}_3@SR-\text{NH}_2$, followed by high-resolution scans of regions of interest: C 1s, N 1s and O 1s. The elements present on the surface could be identified by the general scan displayed in Figure 4-5. The spectra show peaks at energies characteristic for nitrogen and carbon, introduced by APTES functionalization, as well as the silicon and oxygen from silica.^{22,23}

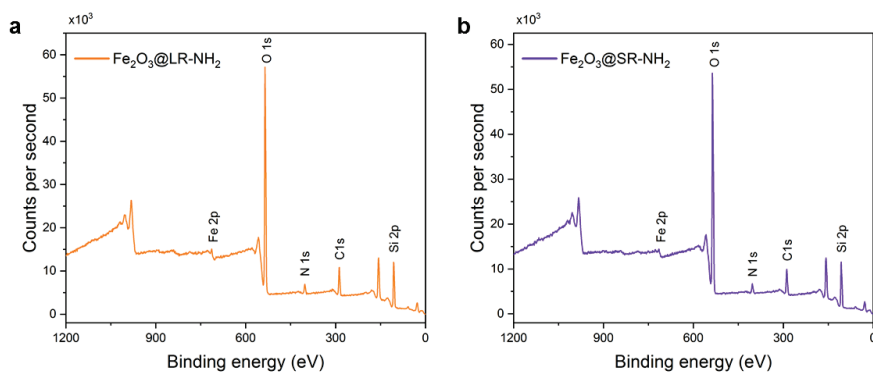


Figure 4-5. General XPS spectra of (a) $\text{Fe}_2\text{O}_3@SR-\text{NH}_2$ and (b) $\text{Fe}_2\text{O}_3@LR-\text{NH}_2$.

The high-resolution spectra of the studied regions are shown in Figure 4-6. Despite having tried to optimize the parameters of the charge neutralizer, the width of peaks evidences a significant influence of surface charging. The impossibility to use magnetic lenses could also contribute to that effect. Because of the high width of peaks in high-resolution scans, it was not possible to distinguish chemical species with clarity. However, the shape of peaks of both N 1s and C 1s was in good agreement with data found in the literature regarding APTES-functionalized surfaces.^{24,25}

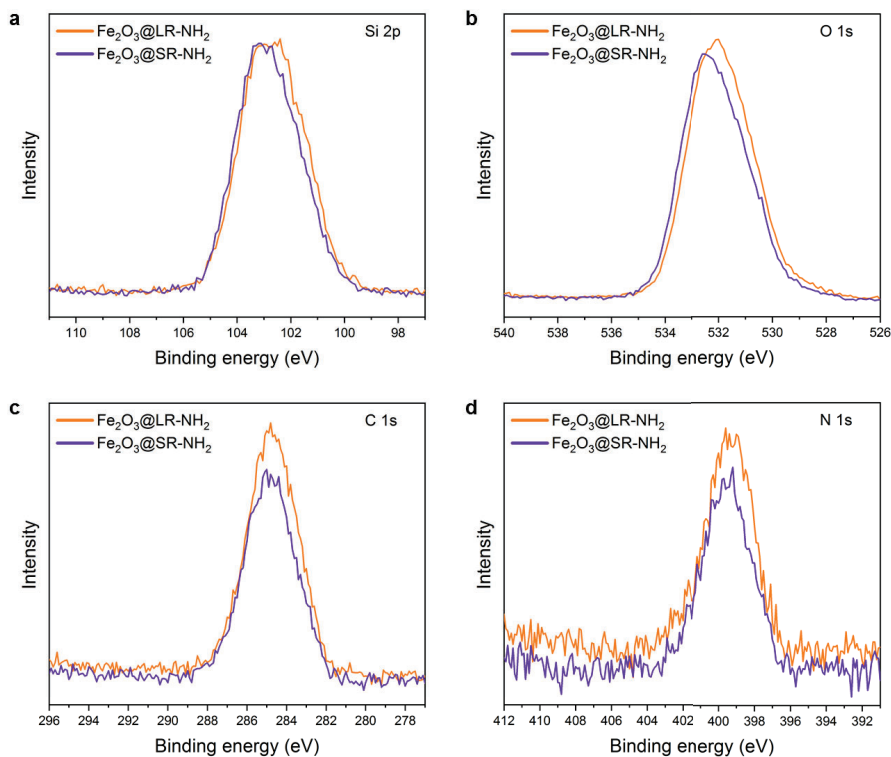


Figure 4-6. High resolution XPS spectra of regions of interest of Fe₂O₃@LR-NH₂ and Fe₂O₃@SR-NH₂: (a) Si 2p, (b) O 1s, (c) C 1s, and (d) N 1s.

The deconvolution of N 1s spectra (Figure 4-7) suggested surface species including C-NH₂ and C-NH₃⁺.²⁵ The amine group (C-NH₂) was dominant in both samples.

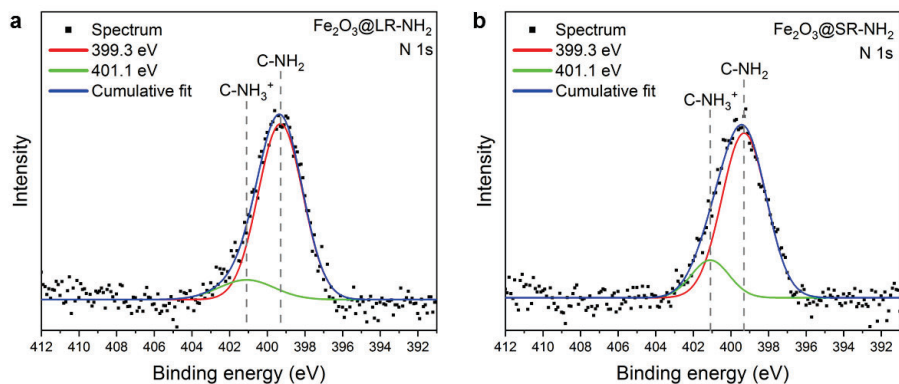


Figure 4-7. Surface species classification in N 1s spectra of $\text{Fe}_2\text{O}_3@LR\text{-NH}_2$ and $\text{Fe}_2\text{O}_3@SR\text{-NH}_2$.

The XPS spectra were also used for elemental quantification. The elemental amounts detected by XPS are presented in Table 4-2.

Table 4-2. Amount of silicon, oxygen, nitrogen and carbon atoms (in atomic %) on the surface of $\text{Fe}_2\text{O}_3@SR\text{-NH}_2$ and $\text{Fe}_2\text{O}_3@LR\text{-NH}_2$.

Sample ID	Si 2p (at. %)	O 1s (at. %)	N 1s (at. %)	C 1s (at. %)
$\text{Fe}_2\text{O}_3@SR\text{-NH}_2$	24.8	54.2	3.3	17.7
$\text{Fe}_2\text{O}_3@LR\text{-NH}_2$	24.6	53.1	3.7	18.6

When analysing the XPS results, it should be taken into account that the signal is collected from a depth down to $3\lambda_{IMFP}$, where λ_{IMFP} is the inelastic mean free path of the electron²⁶ (4.0 nm for SiO_2 under $\text{AlK}\alpha$ radiation²⁷). Therefore, the concentration of amine-terminated species on the outermost surface layer of silica rods is in fact larger than indicated by the N to Si ratios calculated from the data in Table 4-2 (0.13 for $\text{Fe}_2\text{O}_3@SR\text{-NH}_2$ and 0.15 for $\text{Fe}_2\text{O}_3@LR\text{-NH}_2$). The signal intensity I_0 for electrons emitted from a depth δ below the surface is attenuated according to:

$$I_s = I_0 e^{-\delta/\lambda_{IMFP}}$$

Where I_s is the signal intensity as it reaches the surface. Assuming homogeneous properties of the material throughout the depth of the analysis, the contribution of the outermost layer of Si atoms (*i.e.* for δ lower than the Si-O-Si spacing, which equals 0.3 nm in amorphous silica²⁸) is approximately 10% of the detected Si signal intensity. From the experimental determination of $\text{N/Si} = 0.13\text{-}0.15$ and considering that only 10% of analysed Si atoms are at the surface, it can be assumed that roughly

all the silanol groups on the surface of the rods have been efficiently functionalized with APTES, resulting in a homogeneous, saturated amine-terminated layer on MSRs.

4.3. Functionalization of MSRs with fluorophores

The introduction of amine groups to the surface of MSRs allowed me to chemically attach other molecules to obtain fluorescent materials that could be used as contrast agents in optical imaging.

4.3.1. Functionalization with fluorescamine

Fluorescamine, or fluram, is a non-fluorescent compound that reacts quickly with primary amines ($R-NH_2$), forming a fluorescent derivative that emits green light upon irradiation with ultraviolet (UV) light (Figure 4-8).²⁹ Fluorescamine was conjugated to the amine groups on the surface of the APTES functionalized MSRs. The LR and SR samples functionalized with fluram were denominated LR-FL and SR-FL, respectively. The attachment of fluram to the rods could be confirmed by fluorescence spectroscopy, considering that free fluram does not show fluorescence.

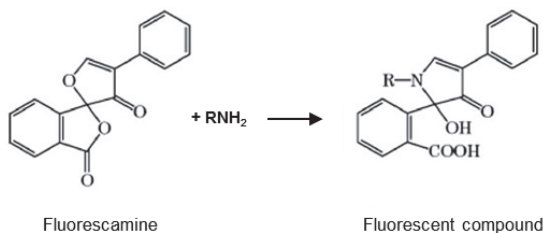


Figure 4-8. The structure of fluorescamine and the fluorescent compound formed as a result of its reaction with primary amines.

After the reaction, the color of the MSR dispersion changed from white to intense yellow (Figure 4-9 a). Under irradiation with UV light, green fluorescence was observed (Figure 4-9 b). The fluorescence emission spectrum was then recorded under irradiation at 390 nm and an intense emission peak was observed at 525 nm (Figure 4-9 c).

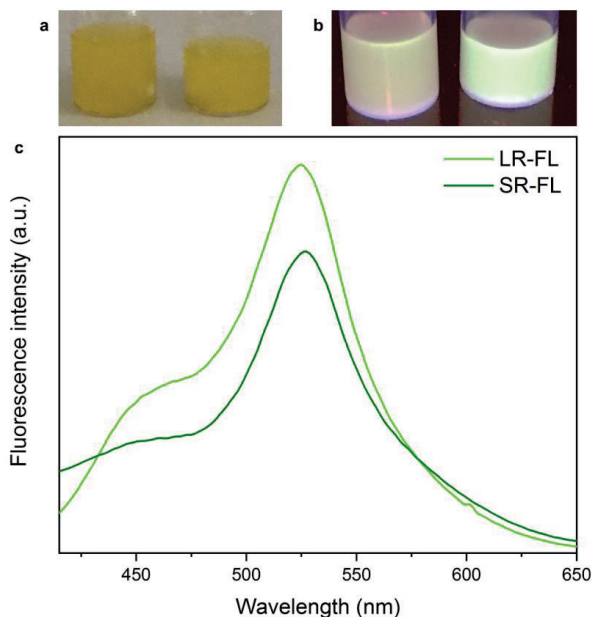


Figure 4-9. (a) Dispersions of LR-FL and SR-FL under white light. (b) Dispersions of LR-FL and SR-FL under UV light. (c) Fluorescence spectra of LR-FL and SR-FL under excitation at 390 nm.

4.3.2. Functionalization with Cy5

Cyanines (Cy) are a family of dyes belonging to the group of polymethine dyes, characterized by conjugated double bonds flanked by an electron acceptor and an electron donor.³⁰ Cationic cyanine dyes contain nitrogen atoms on both ends of the chromophore. Various cyanines have been used for life science applications but the most popular ones were introduced in the early 1990s as a modification of cyanine dye Indocyanine Green (ICG), and they all contain two indolenine rings flanking a polymethine chain. The dyes have large extinction coefficients and exhibit high quantum yields, resulting in bright fluorescence. Depending on the polymethine chain length, cyanine dyes absorb and emit in the visible (short chains) to infrared (long chains) regions of the electromagnetic spectrum.

In this work, MSRs were functionalized with Cyanine5 (also described as Cy5, where Cy stands for cyanine, and the number 5 refers to the number of carbon atoms between the indolenine groups).³⁰ This fluorophore is often used in biomedical research for cell and tissue labeling.³¹ Cy5 solutions have a very intense blue color and emit in the red region, where many CCD detectors exhibit maximum sensitivity, and biological objects show low absorption.

To attach the Cy5 dye to the MSR surface, N-hydroxysuccinimide (NHS) ester derivative of Cy5 was used and reacted with amine groups of APTES functionalized silica surface, forming an amide bond in basic conditions (Figure 4-10).³²

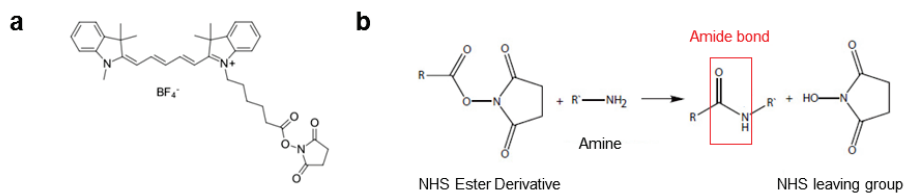


Figure 4-10. (a) Structure of Cy5 NHS ester. (b) Reaction scheme of an NHS ester derivative with a primary amine forming an amide bond.

After the reaction of aminofunctionalized MSRs with Cy5, a blue product was observed. UV-Vis absorption spectra confirmed the presence of Cy5, as shown in Figure 4-11 comparing the absorbance of free Cy5 with Cy5-functionalized SR (denominated SR-Cy5). A characteristic Cy5 band was observed at 652 nm, slightly shifted (~10 nm) towards higher wavelengths with respect to the absorbance curve of free Cy5. A similar effect has been reported in the literature for Cy5 and other fluorophores bound to surfaces^{33,34} and can be explained by the change in polarity and polarizability of the fluorophore environment compared to free fluorophore.³⁵

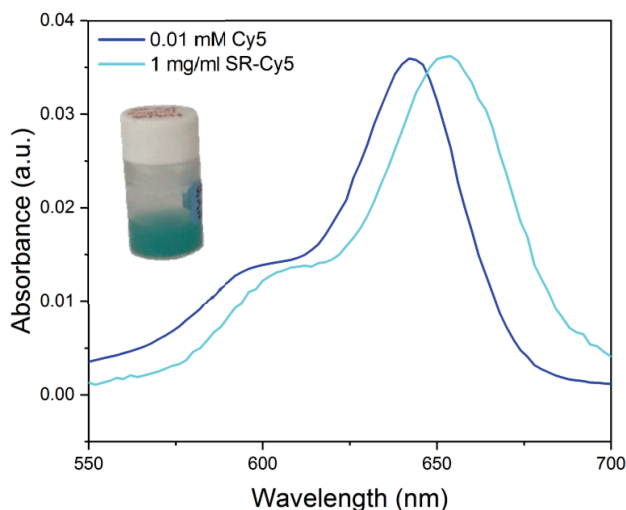
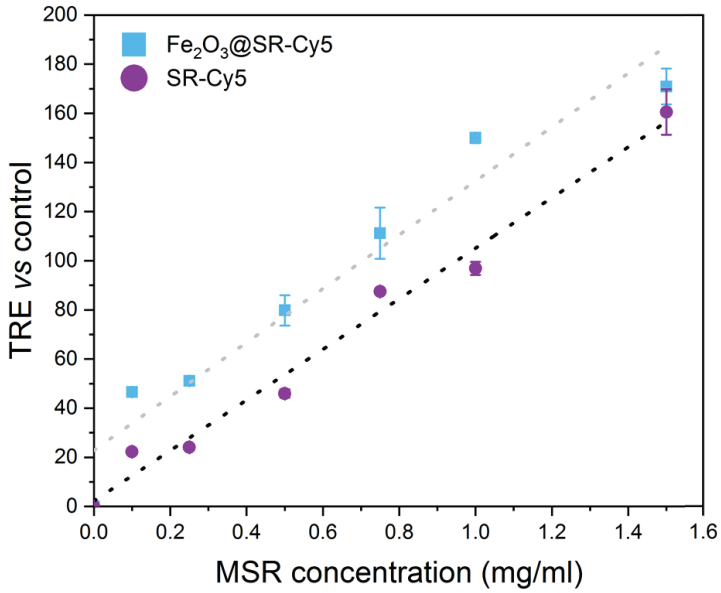


Figure 4-11. The absorbance of SR-Cy5 compared to Cy5 solution. Characteristic double peak of Cy5 is observed after functionalization of silica. Inset: A dispersion of SR-Cy5.

While acquiring fluorescence spectra of the samples, the emission peaks of Cy5 were difficult to analyse as they were overlapping with a strong scattering signal that was observed for all MSRs. For this reason, the fluorescence emission of SR-Cy5 and Cy5-functionalized $\text{Fe}_2\text{O}_3@SR$ ($\text{Fe}_2\text{O}_3@SR\text{-Cy5}$) was instead studied in a fluorescence imaging instrument. The same measurement technique was later used for *in vivo* fluorescence studies of the MSRs.

Optical imaging phantoms were made by preparing a dispersion of rods in an aqueous solution of D-mannitol (55 mg/ml) that was then diluted to obtain a range of concentrations (0–1.5 mg/ml). Mannitol solution was used instead of water due to the increased stability of the dispersion of rods in this medium. Emission was measured under excitation at 640 nm. The particles exhibited high fluorescence, linearly increasing with the concentration (Figure 4-12). The total radiant efficiency (TRE) was very similar for both SR-Cy5 and $\text{Fe}_2\text{O}_3@SR\text{-Cy5}$. Therefore, it was decided that the iron oxide NP-loaded rods would be used for *in vivo* studies, as this system offers the potential of combining two modalities without a decrease in its performance as a fluorescence imaging agent.

a



b

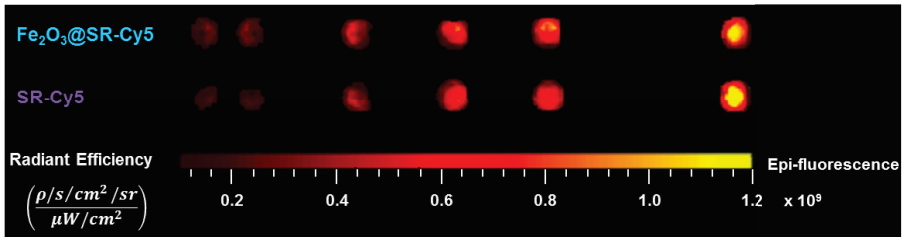


Figure 4-12. *Fluorescence imaging.* (a) TRE vs control of SR-Cy5 and Fe₂O₃@SR-Cy5 plotted as a function of sample concentration showing a linear dependence. $n = 2$. (b) Fluorescence images of SR-Cy5 and Fe₂O₃@SR-Cy5 dispersions for the same MSR concentrations as in (a).

4.4. Chapter summary

A protocol of MSR surface functionalization with amine groups has been developed. The problem of an inefficient coating has been solved by choosing the optimal solvent and reaction temperature, as well as performing a high-temperature treatment after the reaction that increased the formation of siloxane bonds. Degradation of rods has been prevented by using low APTES concentrations. Successful aminosilane coating was achieved for reaction times as short as 1 h.

The presence of amine groups has been confirmed by a shift from negative to positive values of the zeta potential, the appearance of characteristic bands in FT-IR spectroscopy and both nitrogen and carbon peaks in XPS. XPS elemental quantification was also used to estimate the grafting density on the exterior surface of the rods and it was found to be compatible with predominant surface coverage by APTES.

Amino-functionalized MSR have been surface modified with fluorophores: fluorescamine, emitting in green, and Cyanine5, emitting in red. The presence of fluorescamine on the surface was confirmed by observation of the sample under irradiation with UV light, reflected by the appearance of a fluorescence peak at 525 nm in fluorescence spectroscopy. The presence of Cy5 was confirmed by the appearance of a specific Cy5 absorption band in UV-Vis, as well as by measuring the radiant intensity of fluorescence imaging phantoms excited at 640 nm. These results indicated the potential use of the material as a fluorescence imaging contrast agent, which will be further assessed by *in vivo* trials. It also indicated that the material combines two imaging modalities (MRI and optical imaging contrast agents) which are appealing for *in vitro* studies.

4.5. Annex

4.5.1. Materials

(3-aminopropyl)triethoxysilane (APTES), fluorescamine and triethylamine were purchased from Sigma-Aldrich and used as received. Cyanine5 NHS ester (Cy5-NHS) was purchased from Lumiprobe and used as received. The purity of all reagents was 98% or higher.

4.5.2. Amino-functionalization of MSRs

Amine groups were introduced to the silica rods surface by aminosilanization with (3-aminopropyl)triethoxysilane (APTES), in a protocol that was adapted from the literature^{7,36} with modifications. A solution of ethanol in water (70:30 v/v) was prepared and heated to 70 °C. 20 mg of MSRs were dispersed in 20 ml of this solution by ultrasonication. 120 µl of APTES were added to the dispersion and the mixture was kept at 70 °C under reflux for 1 h. The particles were then washed three times in ethanol and centrifuged at 16773 x g. Then the particles were dispersed in a small amount of ethanol and dried at 60 °C. This step was followed by heating at 120 °C for 2 h in air.

4.5.3. Zeta potential measurements

Zeta potential values of silica rods before and after surface functionalization were measured by Zetasizer Nano ZS (Malvern). MSRs were dispersed in distilled water at a concentration of 0.5 mg/ml and placed in a zeta potential cuvette for the measurements.

4.5.4. Transmission electron microscopy (TEM)

MSR morphology after functionalization with APTES was examined by a JEOL 1210 transmission electron microscope (TEM) operating at 120 kV accelerating voltage. Samples for TEM analysis were prepared by drop-casting ethanol dispersions of the rods (1 mg/ml) on TEM copper grids.

4.5.5. Fourier transform infrared spectroscopy (FT-IR)

Fourier transform infrared spectra were measured by a FT-IR spectrometer (FT-IR JASCO 4700LE) in transmittance mode in a range from 4000 cm⁻¹ to 400 cm⁻¹, using a KBr pellet technique.

4.5.6. X-ray photoelectron spectroscopy (XPS)

The XPS analysis was performed at the *Advanced Microscopy Laboratory* (LMA) unit at the *Universidad de Zaragoza*. The measurements were performed with Kratos AXIS Supra XPS spectrometer using monochromatic X-ray source (Al K α 120 W, 8 mA / 15 kV) under a pressure of 10⁻⁹ Torr. The size of the area analysed was 2 mm x 1 mm. The samples in powder form were placed together on a holder on a conducting double-sided tape to be analysed in the same conditions. Because the samples under investigation were magnetic, the magnetic lenses of the spectrometer could not be used and the measurements were performed in electrostatic mode. It was necessary to employ a charge neutralizer and optimize its parameters to the samples because a strong effect of differential charge was observed that was not neutralized with the default parameters of the equipment. For each sample, a general scan was performed, followed by high resolution regions of interest: C 1s, N 1s, O 1s and Si 2p.

4.5.7. MSR functionalization with fluorescamine

In a typical synthesis, a stock solution was prepared by dissolving 1.4 mg of fluorescamine in 4 ml of acetone. 5 mg of aminofunctionalized MSRs were dispersed in 2.5 ml of acetone and sonicated in an ultrasound bath. Then, 2.5 ml of fluorescamine stock solution were added to the dispersion. The mixture was left to react overnight at room temperature, in the dark, under magnetic stirring. Then, the particles were purified by washing three times with ethanol and centrifugation (16773 x g, 8 min). Finally, the precipitate was dispersed in a small amount of acetone and dried in vacuum. The product was stored at 4°C in the dark.

4.5.8. MSR functionalization with Cyanine5

Cyanine5 solution was prepared by dissolving 1 mg of Cyanine5 NHS ester in 5 ml of acetone. 10 mg of aminofunctionalized MSRs were dispersed in the solution by sonication in an ultrasound bath. Then, 80 μ l of trimethylamine were added. The mixture was left to react overnight at room temperature, in the dark, under magnetic stirring. Then, the particles were purified by washing three times with ethanol and centrifugation (16773 x g, 8 min). Finally, the precipitate was dispersed in a small amount of acetone and dried in vacuum. The product was stored at 4 °C in the dark.

4.5.9. Fluorescence spectroscopy

The samples were dispersed in acetone at a concentration of 1 mg/ml and placed in a quartz cuvette. The fluorescence spectra were recorded with an LS 45 Spectrofluorometer (Perkin-Elmer). The emission spectra of fluorescamine-functionalized samples were recorded at excitation wavelength $\lambda = 390$ nm.

4.5.10. Ultraviolet-visible (UV-Vis) absorption spectroscopy

Dispersions of MSRs in acetone at 1 mg/ml were prepared in 96 well plates (ThermoFisher). The UV-Vis spectra were collected on an Infinite M200PRO Microplate Reader (TECAN) working in absorbance mode.

4.5.11. Fluorescence imaging

Fluorescence molecular imaging (FMI) studies were performed at the Pre-clinical imaging Platform of *Vall d'Hebron Institut de Recerca* (VHIR, Barcelona) in collaboration with the group of Dr. Anna Rosell, under the technical supervision of Alba Grayston. The fluorescence of MSRs was characterized using an IVIS® Lumina LT Series III imaging system (Perkin Elmer, Waltham, MA). All images were acquired at the following $\lambda_{\text{ex}}/\lambda_{\text{em}}$ ranges: 625-655 nm/695-770 nm, centered at 640 nm/732 nm, respectively. A series of concentrations of SR-Cy5 and Fe₂O₃@SR-Cy5 dispersed in a D-mannitol aqueous solution (3 mg/ml) were prepared in saline (1.5 mg/ml, 1 mg/ml, 0.75 mg/ml, 0.5 mg/ml, 0.25 mg/ml, and 0.1 mg/ml), and duplicates of 100 μL per well were imaged in a 96-well plate. Background wells containing saline (0 mg/ml) were used for background measurements. The fluorescence was measured as total radiant efficiency - TRE ([photons/s]/[$\mu\text{W}/\text{cm}^2$]). For quantification, circular ROIs were manually drawn surrounding the fluorescence signal and total radiant efficiency (TRE; [photons/s]/[$\mu\text{W}/\text{cm}^2$]) was measured using the Living Image software (Perkin Elmer, Waltham, MA) and corrected by the TRE from the corresponding ROI in the background control well.

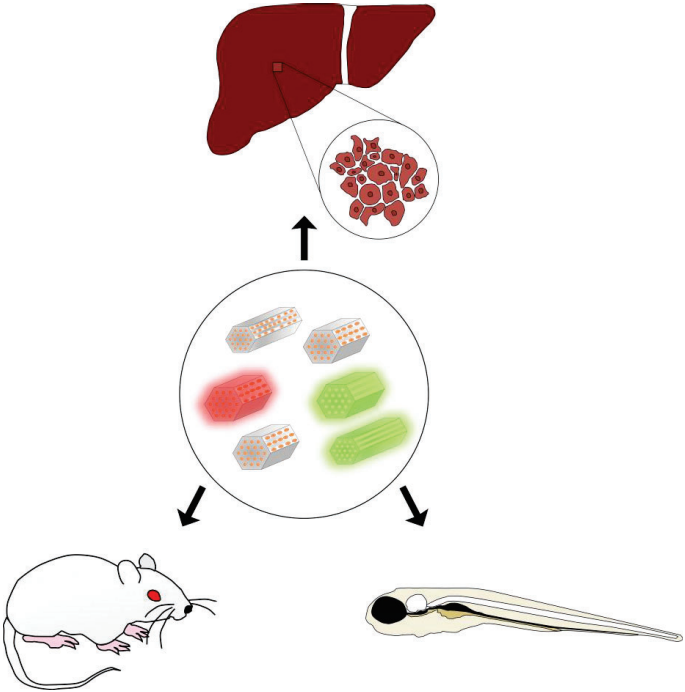
4.6. Chapter references

1. Hasany, M. *et al.* Silica nanoparticle surface chemistry: An important trait affecting cellular biocompatibility in two and three dimensional culture systems. *Colloids Surfaces B Biointerfaces* **182**, 110353 (2019).
2. Yu, T., Malugin, A. & Ghandehari, H. Impact of Silica Nanoparticle Design on Cellular Toxicity and Hemolytic Activity. *ACS Nano* **5**, 5717–5728 (2011).
3. Tran, V. A., Vo, V. G., Shim, K., Lee, S.-W. & An, S. S. A. Multimodal Mesoporous Silica Nanocarriers for Dual Stimuli-Responsive Drug Release and Excellent Photothermal Ablation of Cancer Cells. *Int. J. Nanomedicine* **15**, 7667–7685 (2020).
4. Jiao, Y., Sun, Y., Tang, X., Ren, Q. & Yang, W. Tumor-Targeting Multifunctional Rattle-Type Theranostic Nanoparticles for MRI/NIRF Bimodal Imaging and Delivery of Hydrophobic Drugs. *Small* **11**, 1962–1974 (2015).
5. Quan, G. *et al.* Lactosaminated mesoporous silica nanoparticles for asialoglycoprotein receptor targeted anticancer drug delivery. *J. Nanobiotechnology* **7** (2015).
6. Chong, A. S. M. & Zhao, X. S. Functionalization of SBA-15 with APTES and Characterization of Functionalized Materials. *J. Phys. Chem. B* **107**, 12650–12657 (2003).
7. Liu, Y., Li, Y., Li, X.-M. & He, T. Kinetics of (3-Aminopropyl)triethoxysilane (APTES) Silanization of Superparamagnetic Iron Oxide Nanoparticles. *Langmuir* **29**, 15275–15282 (2013).
8. Stein, A., Melde, B. J. & Schroden, R. C. Hybrid Inorganic–Organic Mesoporous Silicates—Nanoscope Reactors Coming of Age. *Adv. Mater.* **12**, 1403–1419 (2000).
9. Pasternack, R. M., Amy, S. R. & Chabal, Y. J. Attachment of 3-(Aminopropyl)triethoxysilane on Silicon Oxide Surfaces: Dependence on Solution Temperature. *Langmuir* **24**, 12963–12971 (2008).
10. Smith, E. A. & Chen, W. How To Prevent the Loss of Surface Functionality Derived from Aminosilanes. *Langmuir* **24**, 12405–12409 (2008).
11. Manzano, J. S. *et al.* Kinetics of the functionalization of mesoporous silica nanoparticles: Implications on surface group distributions, adsorption and catalysis. *Microporous Mesoporous Mater.* **305**, 110276 (2020).
12. Blitz, J. P., Shreedhara Murthy, R. S. & Leyden, D. E. The Role of Amine Structure on Catalytic Activity for Silylation Reactions with Cab-O-Sil. *J. Colloid Interface Sci.* **126**, 387–392 (1988).
13. White, L. D. & Tripp, C. P. Reaction of (3-Aminopropyl)dimethylethoxysilane with Amine Catalysts on Silica Surfaces. *J. Colloid Interface Sci.* **232**, 400–407 (2000).
14. Ishida, H. A review of recent progress in the studies of molecular and microstructure of coupling agents and their functions in composites, coatings and adhesive joints. *Polym. Compos.* **5**, 101–123 (1984).
15. Sharma, K. K., Anan, A., Buckley, R. P., Ouellette, W. & Asefa, T. Toward Efficient Nanoporous Catalysts: Controlling Site-Isolation and Concentration of Grafted Catalytic Sites on Nanoporous Materials with Solvents and Colorimetric Elucidation of Their Site-Isolation. *J. Am. Chem. Soc.* **130**, 218–228 (2008).
16. Kim, J., Seidler, P., Fill, C. & Wan, L. S. Investigations of the effect of curing conditions on the structure and stability of amino-functionalized organic films on silicon substrates by Fourier transform infrared spectroscopy, ellipsometry, and fluorescence microscopy. *Surf. Sci.* **602**, 3323–3330 (2008).
17. Tian, R. *et al.* Infrared Characterization of Interfacial Si-O Bond Formation on

- Silanized Flat SiO₂/Si Surfaces. *Langmuir* **26**, 4563–4566 (2010).
18. Caravajal, G. S., Leyden, D. E., Quinting, G. R. & Maciel, G. E. Structural Characterization of (3-Aminopropyl)triethoxysilane-Modified Silicas by Silicon-29 and Carbon-13 Nuclear Magnetic Resonance. *Anal. Chem.* **60**, 1776–1786 (1988).
 19. Vrancken, K. C., Possemiers, K., Van Der Voort, P. & Vansant, E. F. Surface modification of silica gels with aminoorganosilanes. *Colloids Surfaces A Physicochem. Eng. Asp.* **98**, 235–241 (1995).
 20. Peña-Alonso, R., Rubio, F., Rubio, J. & Oteo, J. L. Study of the hydrolysis and condensation of γ -Aminopropyltriethoxysilane by FT-IR spectroscopy. *J. Mater. Sci.* **42**, 595–603 (2007).
 21. Soltani, R., Dinari, M. & Mohammadnezhad, G. Ultrasonic-assisted synthesis of novel nanocomposite of poly(vinyl alcohol) and amino-modified MCM-41: A green adsorbent for Cd(II) removal. *Ultrason. - Sonochemistry* **40**, 533–542 (2018).
 22. Zhang, F. & Srinivasan, M. P. Self-Assembled Molecular Films of Aminosilanes and Their Immobilization Capacities. *Langmuir* **20**, 2309–2314 (2004).
 23. McGovern, M. E., Kallury, K. M. R. & Thompson, M. Role of Solvent on the Silanization of Glass with Octadecyltrichlorosilane. *Langmuir* **10**, 3607–3614 (1994).
 24. Ye, L. *et al.* High sensitivity biosensors based on germanium nanowires fabricated by Ge condensation technique. *Mater. Lett.* **172**, 142–145 (2016).
 25. Sosa, N., Chanlek, N. & Wittayakun, J. Facile ultrasound-assisted grafting of silica gel by aminopropyltriethoxysilane for aldol condensation of furfural and acetone. *Ultrason. - Sonochemistry* **62**, 104857 (2020).
 26. Tanuma, S., Powell, C. J. & Penn, D. R. Calculation of electron inelastic mean free paths (IMFPs) VII. Reliability of the TPP-2M IMFP predictive equation. *Surf. Interface Anal.* **35**, 268–275 (2003).
 27. Powell, C. J. & Jablonski, A. *NIST Electron Inelastic-Mean-Free-Path Database, Version 1.2, SRD 71*. (National Institute of Standards and Technology, 2010).
 28. Zhuravlev, L. T. The surface chemistry of amorphous silica. Zhuravlev model. *Colloids Surfaces A Physicochem. Eng. Asp.* **173**, 1–38 (2000).
 29. Udenfriend, S. *et al.* Fluorescamine: A Reagent for Assay of Amino Acids, Peptides, Proteins, and Primary Amines in the Picomole Range. *Science* **178**, 871–872 (1972).
 30. Cyanine dyes. *Lumiprobe GmbH. GE Healthcare* Available at: <https://www.lumiprobe.com/tech/cyanine-dyes>.
 31. Petrov, S. A. *et al.* Polypeptide-Based Molecular Platform and Its Docetaxel/Sulfo-Cy5-Containing Conjugate for Targeted Delivery to Prostate Specific Membrane Antigen. *Molecules* **25**, 5784 (2020).
 32. Hermanson, G. T. Chapter 5 - Homobifunctional Crosslinkers. in *Bioconjugate Techniques* (ed. Hermanson, G. T.) 275–298 (Academic Press, 2013).
 33. Jiménez Sánchez, G. *et al.* Fluorescent Radiosensitizing Gold Nanoparticles. *Int. J. Mol. Sci.* **20**, 4618 (2019).
 34. Tarpani, L. & Latterini, L. Effect of metal nanoparticles on the photophysical behaviour of dye–silica conjugates. *Photochem. Photobiol. Sci.* **13**, 884 (2014).
 35. Wang, L., Gaigalas, A. K. & Reipa, V. Optical properties of AlexaTM 488 and CyTM5 immobilized on a glass surface. *Biotechniques* **38**, 127–132 (2005).
 36. Zhu, M., Lerum, M. Z. & Chen, W. How To Prepare Reproducible, Homogeneous, and Hydrolytically Stable Aminosilane-Derived Layers on Silica. *Langmuir* **28**, 416–423 (2012).

Chapter 5

Cell and animal studies



5.1. Introduction

Needless to mention that nanomaterials intended for medical applications must not cause cytotoxicity and should perform the desired function in the living organisms. For that, a battery of *in vitro* and *in vivo* tests are needed in pre-clinical models before human clinical trials can start as the last validation towards clinical translation. Animal models can be used to identify disease mechanisms and to evaluate the performance and toxicity in preclinical testing of the nanomedicinal formulations.¹⁻⁴ It is known that the bioavailability and toxicity of nanomaterials may be influenced by species and level of organization (cell, embryo, juvenile, adult, male/female, healthy/disease-afflicted).⁵ Therefore, it is important to study the toxicity of nanomaterials in a comparative manner between different models.¹ Thanks to their similarities to humans, reliable data can be often obtained through laboratory rodent studies, for which accurate models of diseases such as in the case of NAFLD have been developed.²⁻⁴

In addition, the small tropical freshwater fish, zebrafish (*Danio rerio*) is an attractive alternative for evaluating toxicity, safety and mechanisms of action of nanomaterials at a preliminary pre-clinical stage. Zebrafish is a widely used model due to its small size, ease of culture, transparency of the embryos, low cost and possibility of high throughput screening.^{5,6} Zebrafish are similar to humans in terms of hepatic cellular composition, function, signaling, and response to injury.¹ For this reason, zebrafish have been used for modeling various liver diseases including NAFLD.^{7,8} Zebrafish form a functional liver in just 4 days post-fertilization.⁸ This species also offer the possibility of testing the effects of therapeutic formulations at different levels of biological organization and developmental stages: cells, embryos or fry.

In this chapter, *in vitro* and *in vivo* studies have been performed to assess the toxicity, uptake and performance of the MSR formulations in different organisms. First, cell viability has been studied using a zebrafish liver cell line (ZFL) which is a common model used for investigating the toxicity of different compounds.^{6,9,10} Similar studies have been then performed on human hepatocytes (Huh7.5). Following *in vitro* studies, the toxicity of MSRs functionalized with fluorescamine was evaluated in zebrafish larvae model and the uptake was monitored in a fluorescence microscope.

Preclinical *in vivo* biodistribution taking advantage of two functional properties of the MSR composites was performed in rodents. MRI imaging studies were carried out after tail-vein injecting rats with Fe₂O₃@SR. The changes in MRI T₂ contrast were evaluated and the effect on the animal respiration was monitored. The biodistribution of MSRs was then analysed using two distinct techniques. Finally, MSRs functionalized with Cyanine5 were used for fluorescent imaging in mice. These experiments aimed at setting the foundation for future studies of the MSR theranostic potential in more complex models of NAFLD.

5.2. *In vitro* studies of MSRs

The studies involving ZFL cells and zebrafish larvae have been done in collaboration with the Evolutionary Immunology group led by Dr. Nerea Roher at the *Institut de Biotecnologia i de Biomedicina* (IBB-UAB). I performed the experiments in the facilities of IBB-UAB under the supervision of Dr. Mariana Teles and Dr. Nerea Roher.

5.2.1. ZFL cell viability and uptake

Cell viability and cellular uptake assays were performed on ZFL. A representative microscopy image of ZFL cells used is shown in Figure 5-1.

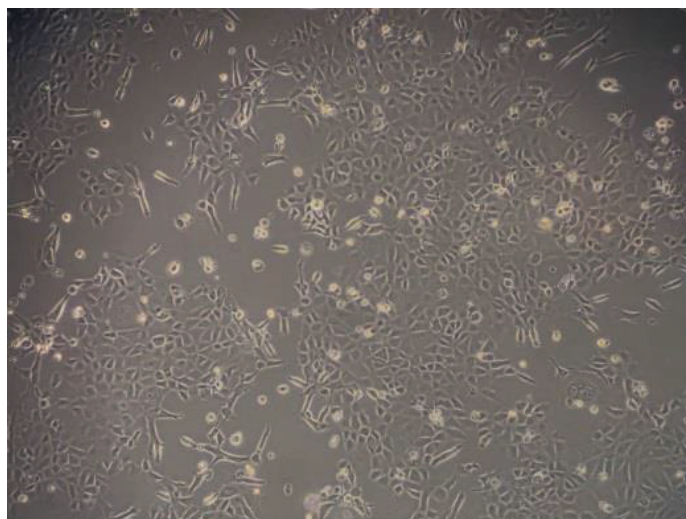


Figure 5-1. ZFL cells observed by an optical microscope.

ZFL cell viability after being exposed to long and short rods with negative and positive surface charge ($\text{Fe}_2\text{O}_3@LR$, $\text{Fe}_2\text{O}_3@LR\text{-NH}_2$, $\text{Fe}_2\text{O}_3@SR$, $\text{Fe}_2\text{O}_3@SR\text{-NH}_2$) was studied using the MTT (3-[4,5-dimethylthiazol-2-yl]-2,5-diphenyltetrazolium bromide) reduction assay. This colorimetric method signals cell metabolism based on the ability of the mitochondrial enzymes to convert the yellow compound MTT to a blue formazan dye. The amount of dye that is produced is proportional to the number of viable, metabolically active cells.⁶

The results of the MTT assay in ZFL cells after 6 h of exposure to MSRs ($n = 12$) are shown in Figure 5-2. It can be observed that none of the four types of MSRs caused cytotoxicity in ZFL cells for concentrations up to 50 $\mu\text{g/ml}$. At 200 $\mu\text{g/ml}$, the

number of viable cells decreased significantly for negatively and positively charged long rods, $\text{Fe}_2\text{O}_3@\text{LR}$ and $\text{Fe}_2\text{O}_3@\text{LR-NH}_2$, respectively. The lowest toxicity in ZFL cells at 200 $\mu\text{g}/\text{ml}$ was observed for positive short rods, $\text{Fe}_2\text{O}_3@\text{SR-NH}_2$.

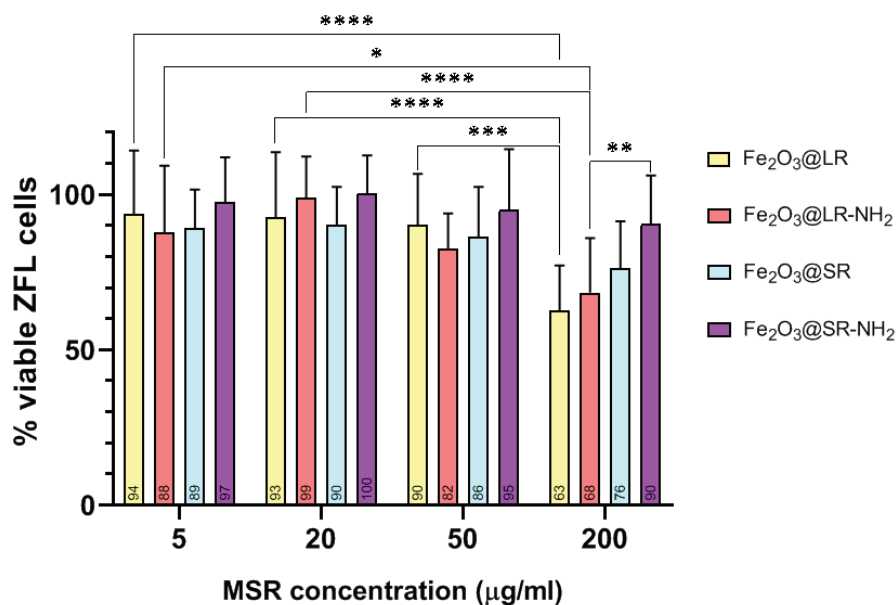


Figure 5-2. ZFL cell viability after 6 h of exposure to the different types of MSRs at four different concentrations. $n = 12$. * $P \leq 0.05$, ** $P \leq 0.01$, *** $P \leq 0.001$, **** $P \leq 0.0001$.

As reported in the literature described in Chapter 1, a relation between the aspect ratio of mesoporous silica rods and cytotoxicity has been often observed. However, this effect is complex and greatly depends on the cell type. The results of the cell viability assay performed on ZFL cells suggest that the toxicity is dependent on the concentration and the aspect ratio of MSRs, while the surface charge did not produce a significant effect. At 200 $\mu\text{g}/\text{ml}$, the MSRs of AR = 2.2 ($\text{Fe}_2\text{O}_3@\text{SR}$) induced significantly less cytotoxicity in ZFL cells than rods of AR = 4.7 ($\text{Fe}_2\text{O}_3@\text{LR}$).

Uptake of the MSRs by ZFL cells has been studied by SQUID magnetometry at 10 K. Short rods ($\text{Fe}_2\text{O}_3@\text{SR}$, $\text{Fe}_2\text{O}_3@\text{SR-NH}_2$), which were found to be less cytotoxic than long rods, were used in the experiment. The high sensitivity of the SQUID technique can allow measuring the very small magnetic moment of tiny amounts of magnetic material, being the remanent magnetization value proportional to the amount of the magnetic material, not affected by the diamagnetic signal from organic matter. After exposure to MSRs, cells were thoroughly washed to remove particles attached to cell membrane and cell pellets were collected from each well. The hysteresis loops of the

cell pellets were used to determine the remanent magnetic moment (m_r) that was divided by the number of cells in the pellet. The mass of MSRs per cell was determined by dividing the obtained value by the remanent magnetization (M_r) of MSRs (3.3 emu/g of sample for $\text{Fe}_2\text{O}_3@SR$ and 3.0 emu/g of sample for $\text{Fe}_2\text{O}_3@SR\text{-NH}_2$). Figure 5-3 shows a representative hysteresis loop of MSRs and a ZFL cell pellet. The values calculated for each type of MSRs are gathered in Table 5-1.

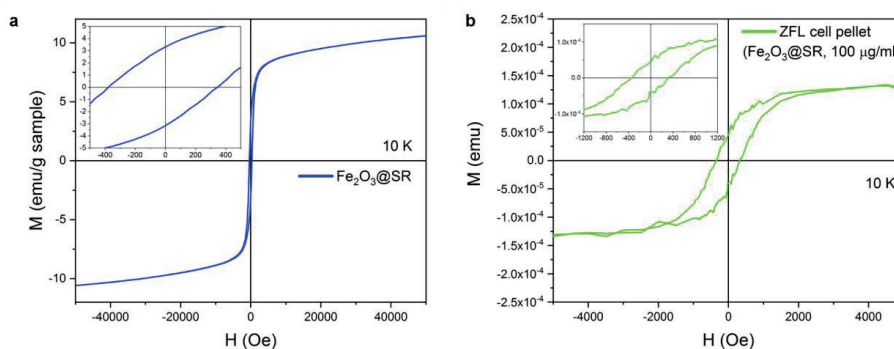


Figure 5-3. Magnetic hysteresis loops recorded at 10 K for $\text{Fe}_2\text{O}_3@SR$ (a) and a pellet of ZFL cells incubated with $\text{Fe}_2\text{O}_3@SR$ (100 $\mu\text{g/ml}$) (b).

Table 5-1. Uptake of MSRs by ZFL cells studied by SQUID magnetometry. Mean values of the magnetic remanence values at 10 K measured for pellets of ZFL cells treated with different concentrations of $\text{Fe}_2\text{O}_3@SR$ and $\text{Fe}_2\text{O}_3@SR\text{-NH}_2$ ($n=4$). The magnetic remanence was divided by the number of cells (approximately 125000 cells were present in each pellet). The remanent magnetic moment per cell was then divided by the M_r measured for MSRs of known mass and the results are presented as mass of MSRs per cell.

MSR sample	[MSR] ($\mu\text{g/ml}$)	m_r (10^{-6} emu)	m_r/cell (10^{-11} emu/cell)	MSR uptake (pg/cell)
$\text{Fe}_2\text{O}_3@SR$	20	2.2 ± 0.3	1.8 ± 0.3	5 ± 1
	50	24 ± 4	19 ± 3	58 ± 9
	100	42 ± 12	34 ± 9	102 ± 28
$\text{Fe}_2\text{O}_3@SR\text{-NH}_2$	20	6 ± 6	5 ± 5	16 ± 17
	50	13 ± 4	11 ± 3	35 ± 11
	100	39 ± 9	32 ± 8	105 ± 26

This method allowed us to calculate the uptake of MSRs by ZFL cells and to express it as the mass of sample uptaken per cell. By calculating the mass of a single rod

($m = 0.2$ pg, see Annex for calculations), the uptake could be also measured as the approximate number of MSRs uptaken per ZFL cell. Figure 5-4 shows the uptake of MSRs by ZFL cells.

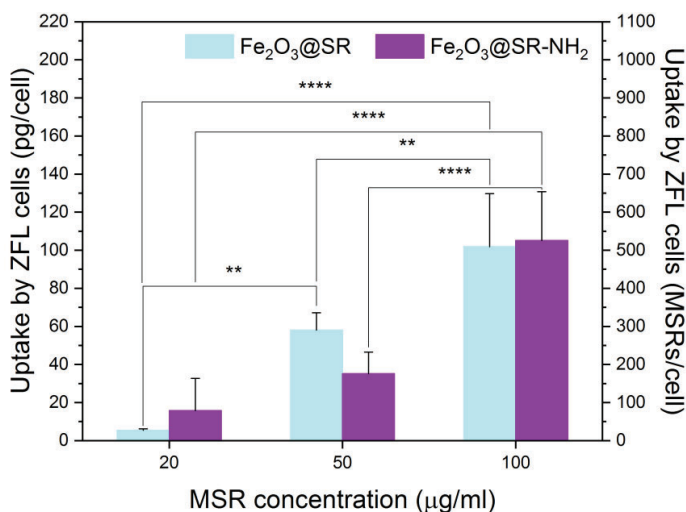


Figure 5-4. The number of the MSRs uptaken by ZFL cells (shown as the mass of sample per cell and number of MSRs per cell) as calculated from remanence magnetization values measured at 10 K. ** $P \leq 0.01$, **** $P \leq 0.0001$.

It was observed that the uptake of MSRs was concentration-dependent for both types of short rods, increasing with the concentration of MSRs. There were no significant differences in the uptake between the negatively and positively charged rods. The ZFL studies have shown that MSRs were successfully taken up by the ZFL cells despite the large dimensions of the rods, and without inducing cytotoxicity even when a large number of rods were internalized by the cells.

5.2.2. Huh7.5 cell viability and uptake

The following part of the thesis aimed to study the cytotoxicity and uptake of MSRs in human hepatocytes, Huh7.5. I had the opportunity to undergo training and perform the experiments in the facilities of *Instituto de Biomedicina de Sevilla (IBiS)* in the SeLiver group led by Prof. Manuel Romero and under the supervision of Dr. Ángela Rojas. However, due to the outbreak of COVID-19 pandemic, the experiments could not be finished. The results of cell viability and uptake that are briefly presented herein are thus preliminary and not conclusive.

Because the cell viability results obtained from MTT assay have shown a high variability between experiments, the viability of Huh7.5 cells incubated with MSRs was determined using trypan blue method.¹¹ After the exposure time (12 h), the cells were washed, trypsinized and aliquots of the cell suspensions were mixed with trypan blue. The stained cells were then counted in a Neubauer chamber. The calculated percentages of viable cells are shown in Figure 5-5.

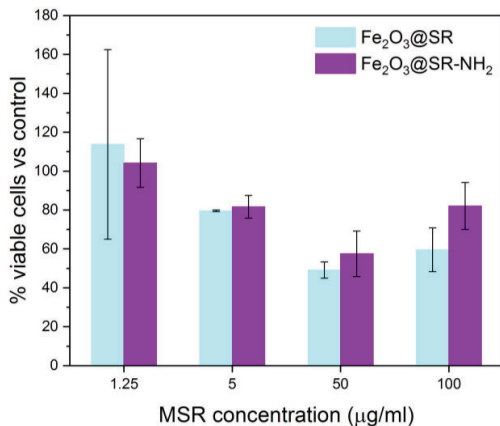


Figure 5-5. Uptake of MSRs by Huh7.5 cells as measured by counting Trypan blue stained cells.

The uptake of MSRs by Huh7.5 cells was studied by SQUID magnetometry. The results are not conclusive because only two replicates (or only one replicate for some samples) could be measured. The results are presented in Table 5-2. The partial results suggested a dose-dependent uptake. At 50 µg/ml, the uptake by Huh7.5 cells at 12 h was comparable with that observed in ZFL cells at 6 h, while at 100 µg/ml it seemed much larger in Huh7.5 cells, although more statistics are needed to draw more robust conclusions.

Table 5-2. Uptake of MSRs by Huh7.5 cells studied by SQUID magnetometry. Mean values of the magnetic remanence values at 10 K measured for pellets of Huh7.5 cells treated with different concentrations of Fe₂O₃@SR and Fe₂O₃@SR-NH₂ (n=2). The magnetic remanence was divided by the number of cells (approximately 75000 cells were present in each pellet). The remanent magnetic moment per cell was then divided by the M_r measured for MSRs of known mass and the results are presented as mass of MSRs per cell.

MSR sample	[MSR] ($\mu\text{g/ml}$)	m_r (10^{-6} emu)	m_r/cell (10^{-11} emu/cell)	MSR uptake (pg/cell)
Fe ₂ O ₃ @SR	50	19 (n = 1)	25	76
	100	205 (n = 1)	273	827
Fe ₂ O ₃ @SR-NH ₂	50	18 \pm 9	24 \pm 13	80 \pm 43
	100	71 \pm 1	94 \pm 1	313 \pm 3

5.3. Uptake of MSRs in zebrafish larvae and effects on survival

Zebrafish larvae were used as an intermediate model between *in vitro* and *in vivo* for larger vertebrates to study the uptake and toxicity of the MSRs. The larvae were incubated with MSRs functionalized with fluram to enable the observation of the rods inside the larvae using fluorescence microscopy.

Figure 5-6 shows the adult zebrafish and the stages between zebrafish eggs and larvae. The zebrafish eggs were collected and placed in E3 medium. Fertilized eggs were separated from unfertilized ones. After hatching, 3 days post-fertilization larvae were placed in a 96 well plate (1 larva per well) and incubated with a dispersion of fluorescent MSR.

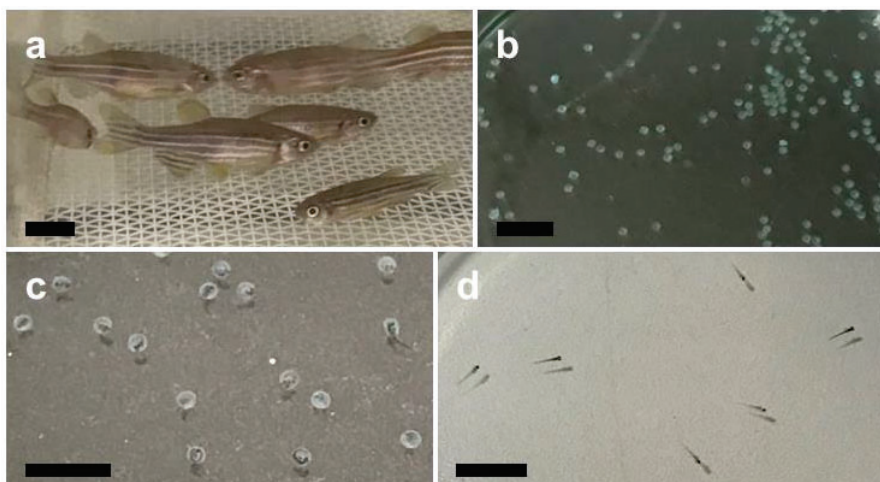


Figure 5-6. Zebrafish lifecycle. (a) Zebrafish. (b) Zebrafish eggs. (c) Zebrafish eggs hatching. (d) Zebrafish larvae. Scale bars: 1 cm.

The toxicity of MSRs on the larvae was monitored by observing the larvae in an optical microscope up to 96 h after exposure to LR-FL and SR-FL at various concentrations (20, 50, 100, 200, 400 and 1000 $\mu\text{g/ml}$). The results are presented in Figure 5-7. 100% survival was observed at 96 h for each studied concentration ($n \geq 5$).

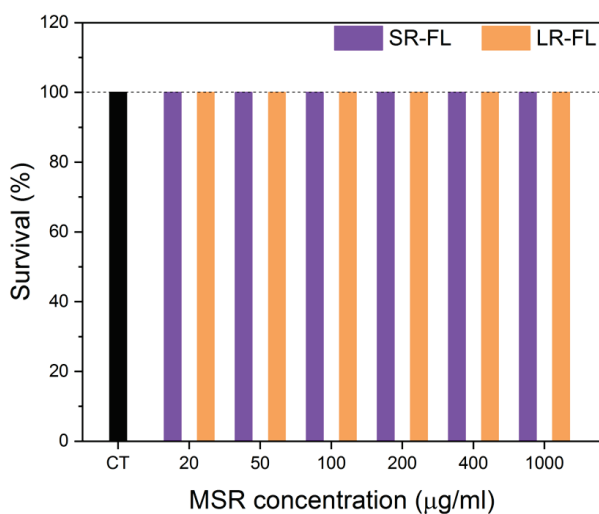


Figure 5-7. Zebrafish larvae survival after 96 h of exposure to fluorescamine-functionalized MSRs.

The uptake of MSRs by zebrafish larvae was then studied in a fluorescence microscope. At 96 h of exposure, a strong green fluorescence of fluram-functionalized rods that was easily distinguishable from the larva autofluorescence was observed, suggesting that the nanoparticles could be located in the liver and intestine (Figure 5-8 d, f).

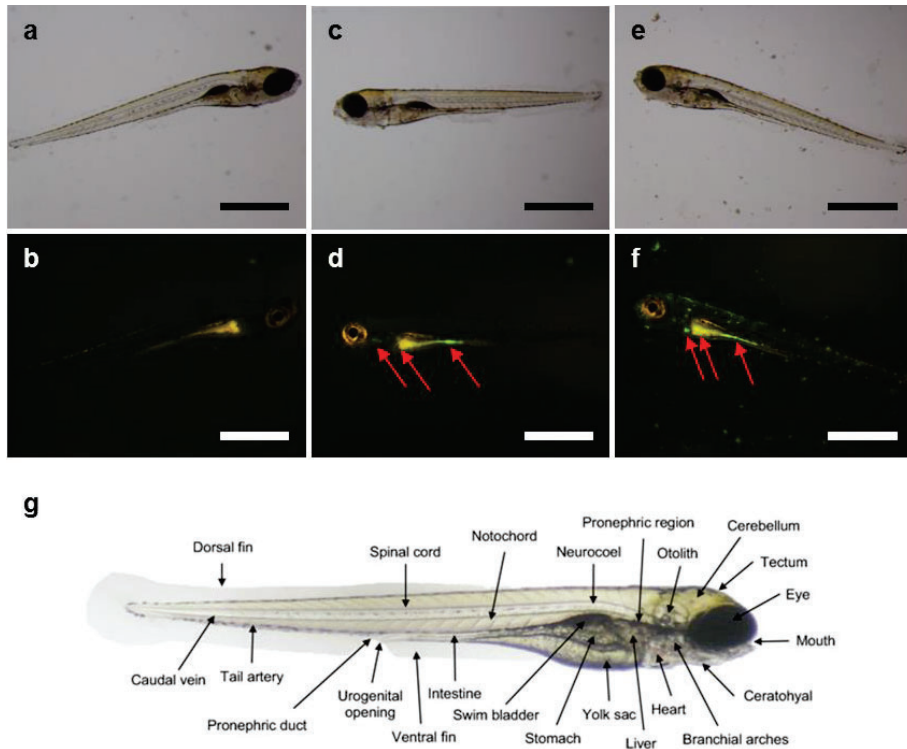


Figure 5-8. MSR uptake by zebrafish larvae. Bright-field microscopy images (top) and corresponding fluorescence images (middle) of an untreated larva (a, b) and two distinct larvae incubated with LR-FL (1 mg/ml) for 96 h (c-f). Fluorescence from MSRs is indicated with red arrows. Scale bars: 1 mm. (g) Anatomy of a zebrafish larva - obtained from *Environ. Sci. Eur.* (2020) by R. von Hellfeld et al.¹²

Specific experiments for tracking the evolution of MSR distribution inside zebrafish larvae were performed using the highest exposure concentration of 1000 $\mu\text{g}/\text{ml}$. After 24 h exposure, the larvae were observed in the fluorescence microscope and then transferred to clean aquarium water. After an additional period of 24 h, the same larvae were observed again. The microscopy images are presented in Figure 5-9. At 24 hours of exposure, MSRs seemed to be accumulated in the liver and following

subsequent 24 h exposure (i.e. after 48 h), it appeared that the fluorescence signal moved to the intestine.

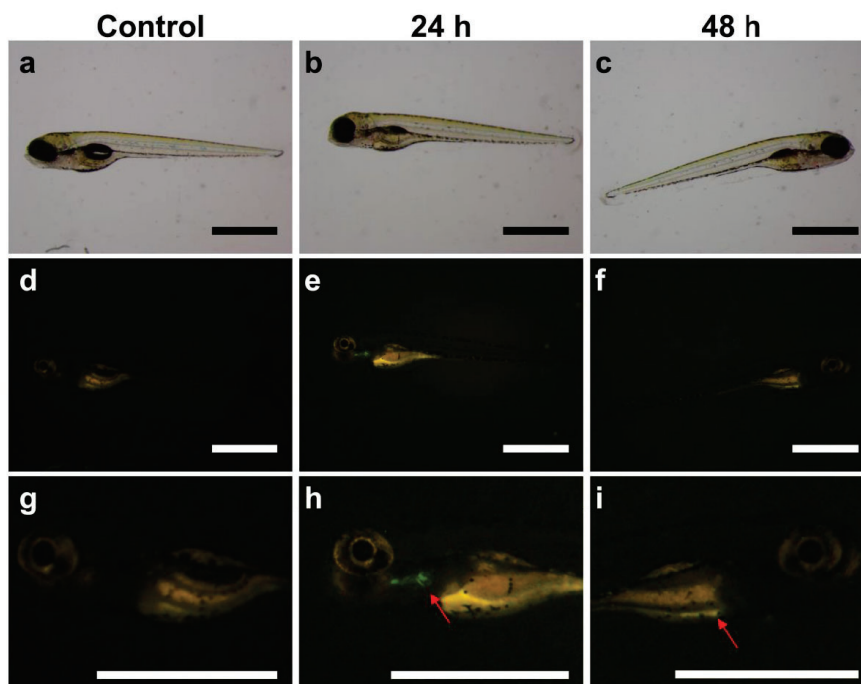


Figure 5-9. Evolution of MSR uptake in zebrafish larvae. Bright field optical microscopy images of an untreated larva (a) and a larva treated with LR-FL at 1000 $\mu\text{g}/\text{ml}$ (b, c). Corresponding fluorescence images after 24 h (d, e), and 48 h (f). Corresponding high magnification images showing regions of interest (g, h, j). Scale bars: 1 mm. Fluorescence from MSRs is indicated with arrows.

Globally, the experiments carried out on zebrafish larvae have suggested that MSRs could pass through the liver of the larvae without causing toxicity, even at concentrations as high as 1000 $\mu\text{g}/\text{ml}$. This is an important first step to set the ground for the future use of this model to study the diagnostic and therapeutic potential of MSRs in NAFLD in zebrafish fed with a high-fat diet.^{13,14}

5.4. MRI imaging in rats

The magnetic MSRs were further used as MRI T_2 contrast agents in experiments on rats. Those experiments were performed in a service regime at the *ICTS ReDIB-Molecular and Functional Imaging Facility* located at the *CIC-Biomagune*. For that,

we selected the short magnetic rods system, as the cell studies suggested that they may cause lower toxicity. Four rats were injected with a dispersion of $\text{Fe}_2\text{O}_3@\text{SR}$ (3 mg/ml in D-mannitol, 1.2 ml) and the MRI T_2 contrast was observed until 60 min post-injection. MRI scans were performed in axial and coronal planes. T_2^* relaxation time maps recorded in axial planes for two studied rats are presented in Figure 5-10. The other two animals did not give reliable results. Slices in which the liver covers the largest area were selected and compared.

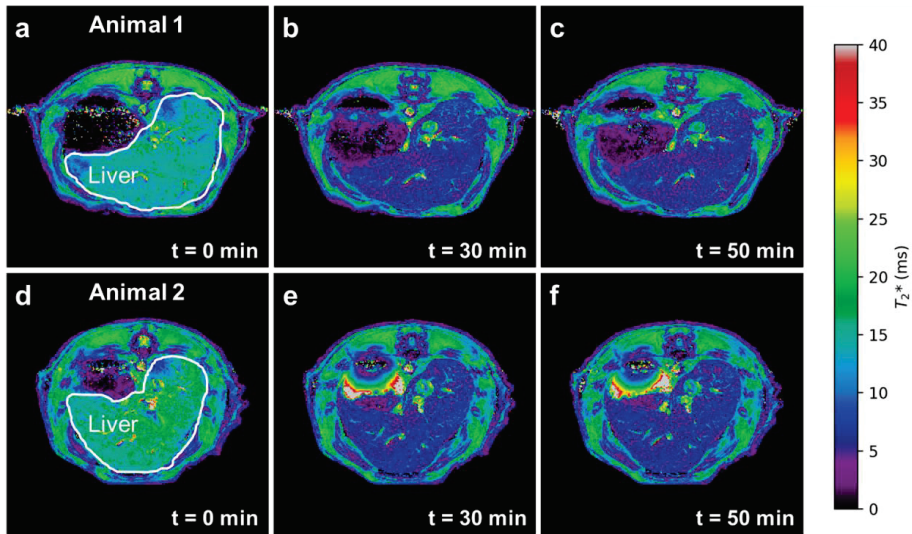


Figure 5-10. T_2^* relaxation time maps of the abdominal area of (a, b, c) animal 1 and (d, e, f) animal 2 recorded at various times: $t = 0$ (pre-injection), $t = 30$ min and $t = 50$ min post-injection of $\text{Fe}_2\text{O}_3@\text{SR}$.

It can be seen that after the injection of MSRs, the contrast in the area of the liver decreases. The maps from Figure 5-10 have been used to determine the T_2^* values in the liver, as shown in Table 5-3. The results indicated a two-fold decrease of the MRI T_2^* contrast in the liver for both animals.

Table 5-3. T_2^* values in the liver of the two studied rats, before and 50 min after MSR injection.

Animal	Time	T_2^* (ms)
1	pre-injection	14 ± 3
1	50 min	7 ± 4
2	pre-injection	17 ± 5
2	50 min	7 ± 5

T_2 relaxation time maps recorded in coronal planes are shown in Figure 5-11. Similar to the T_2^* maps, slices with the largest area occupied by the liver were analysed.

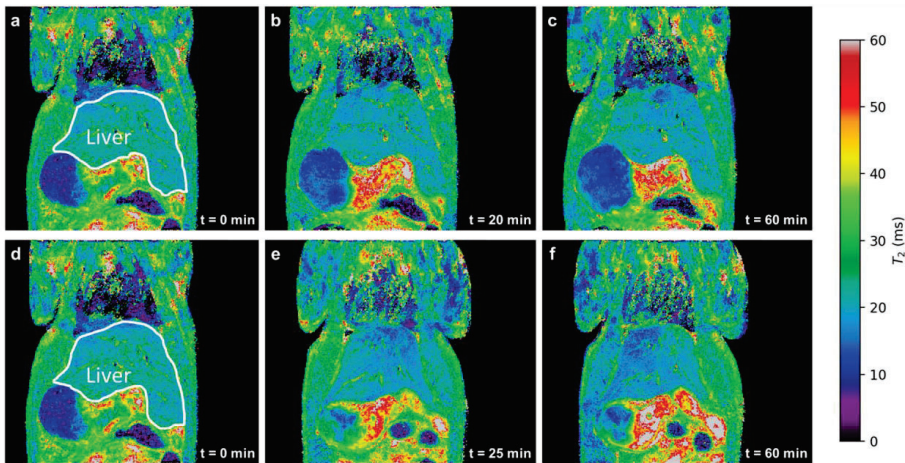


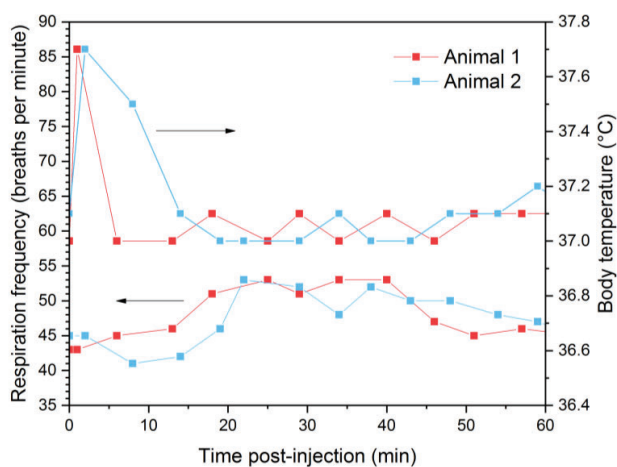
Figure 5-11. T_2 relaxation time maps of the abdominal area of (a, b, c) animal 1 and (d, e, f) animal 2 recorded at various times: $t = 0$ (pre-injection), $t = 20$ -25 min and $t = 60$ min post-injection of $\text{Fe}_2\text{O}_3@SR$.

In contrast to the maps recorded in axial planes in a T_2^* sequence, the coronal MRI T_2 images did not show a significant contrast change for the experiment. These findings are confirmed by the T_2 relaxation time values listed in Table 5-4.

Table 5-4. T_2 values in the liver of the two studied rats, before and 60 minutes after MSR injection.

Animal	Time	T_2 (ms)
1	pre-injection	22 ± 5
1	60 min	21 ± 4
2	pre-injection	23 ± 6
2	60 min	20 ± 6

Due to the characteristics of the lungs, changes in MRI T_2 -contrast in this organ cannot be easily seen. Therefore, the potential accumulation in the lungs was assessed indirectly by monitoring the animal respiration rate. During the acquisition of MRI scans, no critical changes in animal respiration or body temperature have been observed (Figure 5-12). The animals survived the experiment.

**Figure 5-12.** Respiration and body temperature of the two studied rats monitored after intravenous injection of $\text{Fe}_2\text{O}_3@SR$.

We thus conclude that T_2^* sequences of axial planes were more effective to image the liver with the $\text{Fe}_2\text{O}_3@SR$. Furthermore, considering the better relaxivity value for the $\text{Fe}_2\text{O}_3@LR$ reported in Chapter 3, this system should be also investigated in the future, now that is proved that the rats did not show adverse effects under the administration of the short rods.

Following the MRI scans, the animals were sacrificed and the organs of interest (livers and lungs) were extracted. The organs were lyophilized and made into a homogeneous powder (Figure 5-13).

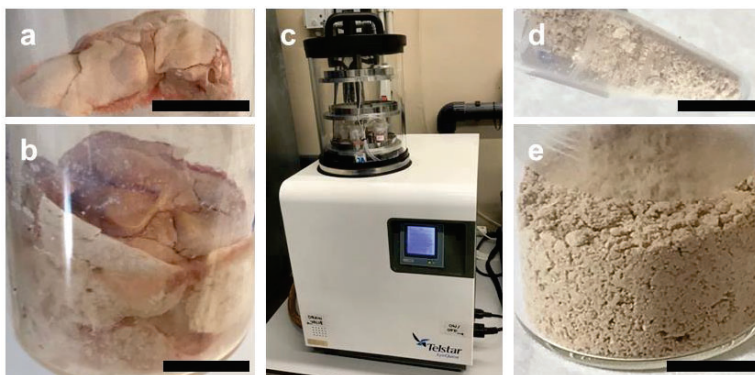


Figure 5-13. Lyophilized organs of rats: (a) lungs and (b) liver. (c) Lyophilizer. Homogenized samples of (d) lungs and (e) liver. Scale bars: 1 cm.

More quantitative biodistribution of magnetic rods was then assessed by two distinct techniques: SQUID magnetometry and ICP-OES. Magnetization *vs* magnetic field measurements of liver and lung samples of control and treated animals were measured at 10 K. Figure 5-14 shows the data corresponding to half loop measurements (sufficient for our purposes) after the correction of the diamagnetic contributions. The organs of both treated animals displayed similar magnetization curves. In the case of livers, a small magnetic remanence was observed for the control animal, and this value was subtracted from the M_r measured for livers of treated animals. The obtained remanence values and the MSR content in the organs calculated from the remanent magnetization of $\text{Fe}_2\text{O}_3@SR$ ($M_r = 3.3$ emu/g) are listed in Table 5-5.

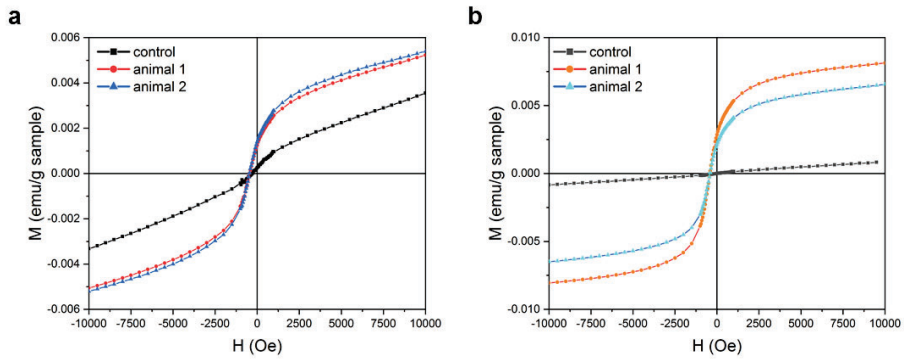


Figure 5-14. Magnetic hysteresis loops at 10 K recorded for (a) livers and (b) lungs.

Table 5-5. Fe₂O₃@SR quantification by SQUID in livers and lungs of rats, 60 min after administration.

Organ	M_r (10^{-3} emu/g sample)	Total organ mass (g)	Total m_r of the organ (10^{-3} emu)	MSR mass in the organ (mg)
Liver 1	1.00	2.18	2.18	0.66
Liver 2	1.15	2.15	2.47	0.75
Lungs 1	2.86	0.23	0.66	0.20
Lungs 2	2.14	0.24	0.51	0.16

The results were compared with data obtained from ICP-OES, where the amounts of iron and silicon in liver and lung samples of control and treated animals were quantified. The data is presented in Table 5-6. The quantification of iron using this method was not possible for liver samples, as a large amount of endogenous iron was present in the livers as it can be seen from the control organ. Endogenous iron was also found in lungs, although in smaller quantities.

Table 5-6. Fe₂O₃@SR quantification by ICP-OES analysis of Fe and Si in livers and lungs of control (CT) and treated (1, 2) rats.

Organ	Total organ mass (mg)	Fe content (mg/g)	Si content (mg/g)	Total Fe (mg)	Total Si (mg)
Liver CT	1927	0.57	<0.01	1.10	0.02
Liver 1	2182	0.50	0.16	1.10	0.35
Liver 2	2152	0.58	0.13	1.25	0.28
Lungs CT	232	0.09	<0.05	0.02	0.01
Lungs 1	230	0.29	0.30	0.07	0.07
Lungs 2	244	0.26	0.12	0.06	0.03

The total mass of MSR sample in the organs was then calculated from ICP-OES assuming 10.5 wt. % iron in Fe₂O₃@SR (determined using the same technique as described in Chapter 3) and similarly, 39.8 wt. % of silicon. The total amount of rods in the organs calculated from Si analysis by ICP-OES was then compared with data derived from SQUID measurements and is shown in Figure 5-15. The total mass of MSRs injected in each animal was 3.6 mg (1.2 ml of MSR dispersion at 3 mg/ml).

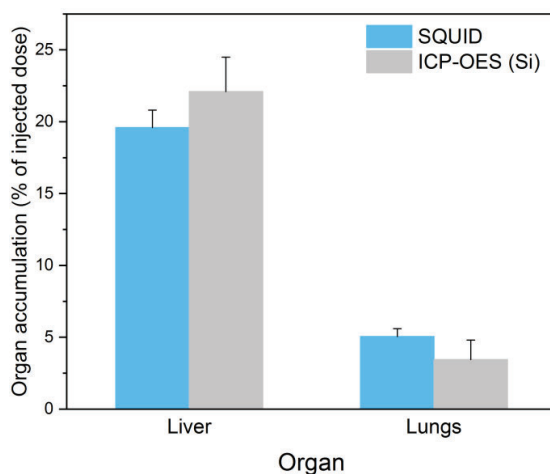


Figure 5-15. Biodistribution in livers and lungs calculated from SQUID and ICP-OES data.

The results of MSR quantification by SQUID were in good agreement with the ones derived from the elemental analysis of Si. Both techniques have shown approximately between four- and six-fold higher uptake by the liver compared to the lungs and that approximately 20% of the administrated sample accumulated in the liver 60 min after administration. Quantification by elemental analysis of Fe could not be compared in liver samples and yielded different results in lungs, due to the presence of endogenous iron in these organs.

The accumulation in the organs was compared with the results reported in the literature for different MSNs (Table 5-7). For comparison, the accumulation in the organs was expressed in % of injected dose per gram of tissue (%ID/g tissue).

Table 5-7. Comparison of the liver and lung accumulation of MSRs with values reported in the literature for similar materials. The accumulation of MSRs expressed in % of injected dose per g of tissue is the mean of the values calculated by the SQUID and ICP-OES techniques.

Source	Material	Dimensions (nm)	Time post-injection (h)	Liver accumulation (%ID/g tissue)	Lung accumulation (%ID/g tissue)
This work	MSR loaded with Fe ₂ O ₃ NPs	400 × 900	1	10 ± 1	18 ± 5
[15]	MS spheres	120	0.5	17 ± 3	147 ± 37
			2	11 ± 3	139 ± 52
	MSR	136 × 1028	0.5	19 ± 5	132 ± 23
			2	21 ± 8	6 ± 2
[16]	MSR	150 × 250	3	45 ± 5	18 ± 3
	MSR	150 × 450	3	41 ± 5	18 ± 4
[17]	MS, almost spherical	900	1	18 ± 3	12.2 ± 0.1
[18]	Porous silicon discoidal particles	400 × 1000	4	26 ± 2	17 ± 3

The accumulation in the liver generally seemed lower than reported in most studies, while similar or lower values were observed for lung accumulation. However, the results could not be compared accurately due to the differences in time post-injection, the animal model used and the size of particles. More studies are needed for longer exposure times to monitor the evolution of liver accumulation of the MSRs. The accumulation profile of Fe₂O₃@LR should be also compared with that of Fe₂O₃@SR.

5.5. Fluorescence molecular imaging in mice

Fluorescent, Cyanine5 labeled short rods loaded with iron oxide NPs ($\text{Fe}_2\text{O}_3@\text{SR-Cy5}$) were used to study their biodistribution by fluorescence molecular imaging (FMI). Those experiments were performed at the Pre-clinical imaging Platform at the *Vall d'Hebron Institut de Recerca* (VHIR, Barcelona) in collaboration with the group of Dr. Anna Rosell. Five mice were injected with a dispersion of the rods in D-mannitol via the tail vein and fluorescence was recorded at 30 min and 60 min. The images acquired at the two time points are presented in Figure 5-16. The fluorescence values are listed in Table 5-8.

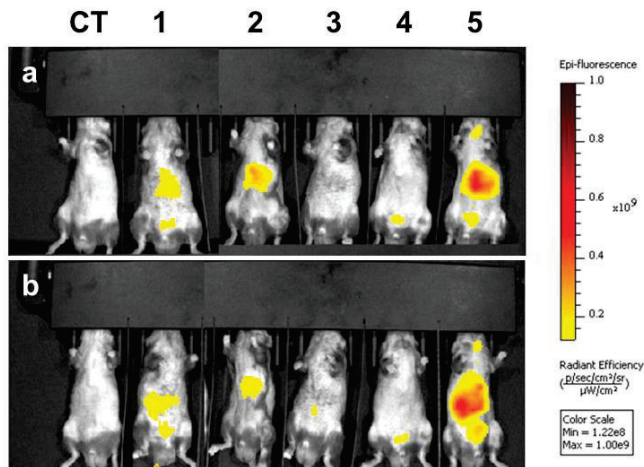


Figure 5-16. *In vivo* fluorescence images of mice injected with $\text{Fe}_2\text{O}_3@\text{SR-Cy5}$ at (a) 30 min, (b) 60 min.

Table 5-8. *In vivo* fluorescence values measured in the abdomen at 30 min and 60 min post-injection.

Animal ID	<i>In vivo</i> fluorescence in the abdomen (TRE vs control)	
	30 min	60 min
1	2.8	2.6
2	2.8	1.8
3	1.8	1.4
4	1.2	1.0
5	5.6	5.8

There were problems with injecting animal 4, therefore this animal will not be considered in the following discussion. A clear fluorescence signal was observed at 30 min in the abdominal area of animals 1, 2 and 5 and remained relatively unchanged at 60 min. At 60 min, fluorescence was also observed in the abdomen of animal 3. The quantitative analysis of fluorescence intensity in the abdomen has shown similar fluorescence values in the first three animals at 30 min, and a slight decrease of these values was observed at 60 min.

After imaging at 60 min, the mice were sacrificed and the major organs (brain, lungs, liver, spleen, and kidneys) were extracted. The fluorescence images of the organs of treated animals compared with control are shown in Figure 5-17. The fluorescence values in the organs in relation to control are listed in Table 5-9.

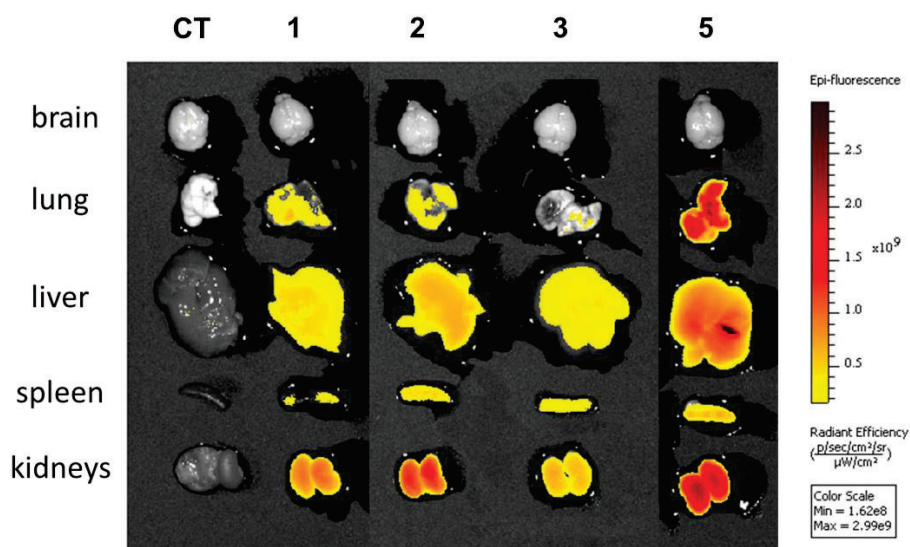


Figure 5-17. *Ex vivo* fluorescent images of organs extracted from mice treated with $Fe_2O_3@SR-Cy5$.

Table 5-9. *Ex vivo* fluorescence values measured in the major organs.

Animal ID	<i>Ex vivo</i> fluorescence (TRE vs control)				
	Brain	Lung	Liver	Spleen	Kidneys
1	1.1	6.7	2.8	5.6	10.2
2	1.1	3.9	2.9	7.5	6.8
3	1.1	2.4	1.9	4.7	4.2
5	1.4	38.0	7.1	19	22.9

As expected, high fluorescence was observed in the livers. No fluorescence was observed in the brains. In contrast to the results of biodistribution studies of MRI imaged rats, the fluorescence studies suggested a relatively high accumulation of MSRs in the lungs. Moreover, the fluorescence emission in the kidneys was also high, which could mean that the MSRs were excreted rapidly or that the cyanine itself was filtered after detaching from the rods. More studies are necessary to explain this effect. The amount of silicon and magnetic iron oxide in different organs should be determined by ICP-OES and SQUID, respectively.

5.6. Chapter summary

The toxicity, uptake and biodistribution of MSRs were assessed by performing both *in vitro* and *in vivo* tests. Studies carried out on ZFL cells showed no toxicity at 6 h for concentrations up to 50 $\mu\text{g/ml}$ of both long and short rods, negatively and positively charged ($\text{Fe}_2\text{O}_3@\text{LR}$, $\text{Fe}_2\text{O}_3@\text{LR-NH}_2$, $\text{Fe}_2\text{O}_3@\text{SR}$, $\text{Fe}_2\text{O}_3@\text{SR-NH}_2$). At 200 $\mu\text{g/ml}$, the toxicity was significantly higher for long rods and still low for both types of short rods. The surface charge was not found to have a significant effect on cytotoxicity.

The uptake of MSRs by ZFL cells was measured by SQUID magnetometry and was found to be concentration-dependent and similar for negatively and positively charged rods. The SQUID technique allowed us to detect quantities as low as several picograms per cell. The results suggested that despite the somehow large dimensions of MSRs, a fair number of rods has been uptaken by the zebrafish liver cells (~ 500 rods when incubated 6 h at 100 $\mu\text{g/ml}$).

In vivo studies on zebrafish larvae indicated no toxicity of short and long rods at concentrations up to 1 mg/ml after 96 h of exposure time. Interestingly, the uptake of fluorescent rods by the liver was observed at 24 h, and at 48 h the rods seem to be located in the intestine of the larvae.

MRI studies were performed on rats after intravenous injection with magnetic short rods ($\text{Fe}_2\text{O}_3@\text{SR}$). A decrease of MRI T_2^* signal in the axial plane was observed at 30 min and 60 min in the liver, suggesting a high accumulation of the contrast agent in the liver. The injection did not cause any anomalous respiration of the animals indicating low impact on the lungs. The accumulation of MSRs in the liver was confirmed by biodistribution studies of extracted organs. The MSR content in the liver and lungs was assessed using two methods: SQUID magnetometry and elemental analysis by ICP-OES. Quantification of magnetic iron oxide using the magnetic remanence values measured by SQUID and measuring the silicon content by ICP-OES led to similar estimates of the MSR content in the livers and lungs. The iron content measured by ICP-OES could not be compared with those values due to a large amount of endogenous iron present in the organs, especially in the liver. The results suggested that up to 20% of the injected MSRs were accumulated in the liver, ~ 5 times more than in the lungs. This corresponded to approximately 10% ID/g of the liver and 18% ID/g of lungs.

Fluorescence imaging was performed *in vivo* on mice after intravenous injection of Cyanine5-functionalized magnetic short rods ($\text{Fe}_2\text{O}_3@\text{SR-Cy5}$). Bright fluorescence was observed in the abdomen at 30 min and 60 min post-injection. *Ex vivo* imaging of the major organs has also shown a high accumulation in the liver but also in the lungs and kidneys. The accumulation in the lungs and particularly kidneys of mice, not observed in rats, deserves further detailed studies.

5.7. Annex

5.7.1. Materials

Zebrafish liver (ZFL) cells were cultured at 28 °C, 5% CO₂ in Dulbecco's modified Eagle's medium (DMEM) with 4.5 g/l glucose, supplemented with 0.01 mg/ml insulin, 50 ng/ml EGF, 5% (v/v) antibiotic/antimycotic solution, 10% (v/v) heat inactivated fetal bovine serum (FBS) and 0.5% (v/v) heat inactivated trout serum (TS) as described in literature.¹⁹ The MTT substrate and DMSO were purchased from Sigma-Aldrich. Huh7.5 cells (Apath LLC, New York, USA) were routinely cultured in DMEM (ThermoFisher, MA, USA) supplemented with 10% FBS and 1% penicillin-streptomycin in an incubator under an atmosphere of 5% CO₂ at 37 °C.

5.7.2. ZFL cell viability studies

Zebrafish cell line (ZFL) studies were performed at the *Institut de Biotecnologia i de Biomedicina* (IBB-UAB, UAB Campus, Bellaterra, Spain) in the Evolutionary Immunology group led by Dr. Nerea Roher. I performed those experiments in the facilities of IBB-UAB under the supervision of Dr. Mariana Teles and Dr. Nerea Roher.

Cytotoxic effects of MSRs on ZFL were assessed using the MTT assay. After 2 h in minimal medium (0–0.5% FBS; 2% antibiotic/antimycotic), cultures were incubated with MSRs (Fe₂O₃@LR, Fe₂O₃@LR-NH₂, Fe₂O₃@SR, Fe₂O₃@SR-NH₂, each MSR type and condition in triplicate). 10% of culture medium volume was removed and replaced with the same volume of either water or stock solution of MSRs, to obtain MSR concentrations of 0, 5, 20, 50 and 200 µg/ml. The cells were incubated with MSRs for 6 h at 28 °C. Cells were then washed in PBS and the MTT substrate was added to 10% of the total volume and further incubated at 28 °C for 30 min. The solution was removed, the cells were solubilized in DMSO and the lysate absorbance was read on a Victor 3 plate reader (PerkinElmer) at 550 nm. The experiment was repeated four times for each type of MSRs. Data were normalized using GrahPad Prism (version 7.01 for Windows, GraphPad Software, San Diego, California USA, www.graphpad.com) such that the control readings were set at 100%. Two-way ANOVA was performed with Dunnett's multiple comparison test.

5.7.3. ZFL cell uptake studies

Before the exposure, the cells in culture were counted in a Neubauer chamber and evenly distributed into wells of a 96 well plate to obtain approximately 125000 cells in each well. The cultures were incubated with MSRs similarly as in the MTT assay protocol. After the exposure for 6 h, the cells were washed with PBS and centrifuged (200 x g, 10 min at 4 °C). Uptake of MSRs by ZFL was assessed using magnetometry measurements at 10 K. The pellets were collected and measured by superconducting

quantum interference magnetometer device (SQUID, Quantum Design Inc.) operating at a maximum applied field of 60 kOe. The m_r values were divided by the number of cells calculated before the experiment. The obtained values were then compared with magnetic remanence values registered for MSR samples of known mass measured by SQUID in the same conditions. The number of uptaken particles per cell was determined assuming an approximate mass of MSRs $m_{MSR} = 0.2$ pg, which was calculated using a formula $m = \frac{\rho\pi r^2 L}{1 + \rho V_{total}}$, where ρ is the density of silica (2.2 g/cm^3), r is the mean radius of the MSRs, L is the mean length of the MSRs, and V_{total} is the pore volume determined from nitrogen adsorption experiments.²⁰

5.7.4. Huh7.5 cell viability and uptake studies

Huh7.5 cell viability and uptake studies were performed at the *Instituto de Biomedicina de Sevilla* (IBiS, Sevilla, Spain) in the SeLiver group led by Prof. Manuel Romero. I performed these experiments in the facilities of IBiS under the supervision of Dr. Ángela Rojas.

Huh7.5 cells were cultured on a 24 well plate (500 μl medium per well) at approximately 75000 cells per well. For cell viability studies, 25 μl of culture medium were removed from each well and 25 μl of water or MSR stock solutions were added to obtain final MSR concentrations of 0, 2.5, 10, 50 and 100 $\mu\text{g/ml}$ ($n = 2$). The cells were incubated with MSRs for 12 h. Then the cells were washed with PBS, trypsinized and transferred to Eppendorf tubes. Cell viability was determined using trypan blue test in a Neubauer chamber. Trypan blue (0.4% wt./v, 30 μl) was added to an aliquot of cell suspension (30 μl) and incubated at room temperature. The viable cells were counted by bright field microscopy. The cells from each suspension were counted in duplicate. The viability values of treated cells were expressed as a percentage of viability of control cells.

For uptake studies, the cell suspensions obtained in the experiment described above were centrifuged (200 x g, 10 min at 4 °C). The pellets were collected and their m_r was measured at 10 K by superconducting quantum interference magnetometer device (SQUID, Quantum Design Inc.) operating at a maximum applied field of 60 kOe. The obtained values were divided by the number of cells calculated before the experiment, and then compared with magnetic remanence values registered for MSR samples of known mass measured by SQUID in the same conditions.

5.7.5. Uptake and toxicity studies in zebrafish larvae

Zebrafish larvae studies were performed at the *Institut de Biotecnologia i de Biomedicina* (IBB-UAB, UAB Campus, Bellaterra, Spain) in the Evolutionary Immunology group led by Dr. Nerea Roher. The experiments were performed in the facilities of IBB-UAB under the supervision of Dr. Mariana Teles and Dr. Nerea

Roher. All experiments involving zebrafish (*D. rerio*) were performed following International Guiding Principles for Research Involving Animals (EU 2010/63) and previously authorized by the Ethics Committee of the *Universitat Autònoma de Barcelona* (UAB, CEEH number 1582).

Wild-type zebrafish (*Danio rerio*) were kept in a re-circulating aquarium with water temperature maintained between 26 and 28 °C. The lighting conditions were 14 : 10 h (light : dark) and adult fish were fed twice a day at a rate of 2% body weight. Ammonia and nitrite levels were kept below the detection level and pH was maintained between 6.8 and 7.5. The nitrate levels were maintained at < 100 mg/l. For in-tank breeding, one female and three males were transferred to a breeding tank in the late afternoon. The divider was removed the next morning after the onset of light. Embryos were collected after 1–2 h and cultured in embryo medium (E3 medium) in a Petri dish (Deltalab). Fertilized eggs were separated from unfertilized eggs using a plastic pipette (Deltalab). The medium was changed to a fresh one every 24 h. At 3 days post-fertilization (dpf), the larvae were placed in a 96-well plate (ThermoFisher), one larva per well containing 200 µl aquarium water or fluram functionalized MSR at 20, 50, 100, 200, 400 and 1000 µg/ml. For mortality studies, groups of larvae ($n \geq 5$ per condition) were used and monitored for 96 h using an optical microscope (Olympus). For uptake studies, groups of 4 larvae per condition were used. After 24 h and 48 h of exposure, the uptake was confirmed by imaging the larvae using a fluorescence stereomicroscope (Nikon SMZ800) coupled with a camera (Nikon DS-Fi2) and a mercury lamp (Nikon C-LHGFI HG lamp, 130 W, wavelength range: 380-600 nm).

5.7.6. *In vivo* MRI studies in rats

Magnetic resonance imaging (MRI) *in vivo* experiments were performed in *CIC BiomaGUNE* (Donostia – San Sebastián) in the *Singular Scientific and Technical Infrastructure* (ICTS) of *ReDIB-Molecular and Functional Imaging Facility* under the technical supervision of Dr. Daniel Padro. The animal license of the ICTS is AE-biomaGUNE-1116. Five female rats of RjHan:Sb type born on 18/02/2021 were used in this study. Four rats were treated with MSRs and imaged and one was used as control for biodistribution studies.

Magnetic resonance imaging (MRI) *in vivo* experiments were performed at 7 T on a Bruker Biospec 70/30 equipped with a system of gradients of 12 cm interior diameter (400 mT/m) and connected to a console Bruker AVANCE III (300 MHz) configured with 2 transmission channels and 4 reception channels. The experiments were carried out using a volumetric antenna of 72 mm in diameter with the transmission and reception of the signal optimized for the body of a rat. The animals were kept under anesthesia during the measurements using isoflurane (1 - 1.5%). The temperature of the animal was kept at approximately 37.0 °C through a system of hot air (SA instruments, NY, USA) and its respiration and temperature during the MRI image

acquisition were monitored through a system SAI M1030 (SA instruments, NY, USA), which at the same time was used to synchronize the acquisition of images with the animal respiration. The monitoring was done at very short time intervals. The MRI session started with the acquisition of base scans before the injection of MSRs. For the injection, the MRI bed where the animal was located was taken out without changing the position of the animal and intravenous injection with 1.2 ml of a dispersion of $\text{Fe}_2\text{O}_3@SR$ (3 mg/ml in an aqueous solution of D-mannitol, 55 mg/ml) via the tail vein was performed. After the injection, the bed was introduced inside the scanner in the same position as before. The scans were repeated until acquiring the last scans at $t = 60$ min after the injection. For T_2 maps, MRI signal was measured at coronal planes using the sequence of Bruker MSME (Multi slice Spin echo) with the following parameters: 20 TEs within the interval $TE = 7.5 - 150$ ms, respiration synchronized with the acquisition, FOV = 60 x 60 mm, ACQ Matrix = 256 x 256, RECO Matrix = 256 x 256, Slice Thickness = 1.5 mm, N Slices = 8, Averages = 2. For T_2^* maps, MRI signal was measured at axial planes using the sequence of Bruker MGE (Multi gradient echo) with the following parameters: 10 TEs within the interval $TE = 3 - 39$ ms, respiration synchronized with the acquisition, FOV = 60 x 60 mm, ACQ Matrix = 256 x 192, RECO Matrix = 256 x 256, Slice Thickness = 1.5 mm, N Slices = 8, Averages = 2.

After the MRI session, the animals were sacrificed, perfused with a saline serum and the livers and lungs were extracted. Organs of an untreated animal were also extracted and used as control. The organs were frozen at -80°C and freeze-dried in a LyoQuest-Telstar lyophilizer (0.05 mBar, 72 h). Then the organs were crushed and made into a homogeneous powder.

Magnetic hysteresis loops at 10 K were collected by a superconducting quantum interference magnetometer device (SQUID, Quantum Design Inc.) with a maximum applied field of 50 kOe.

For ICP-OES analysis of organs, approximately 0.50 g of liver sample in duplicate or 0.05 g of lung sample in duplicate (weighed on analytical balance XPE205DR, Mettler Toledo) were digested with a mixture of concentrated HNO_3 and HF in a microwave oven (Milestone, Ultrawave model). The resulting digestions were introduced into an ICP-OES spectrometer (Agilent, model 5900), and the content of Fe and Si was determined.

5.7.7. *In/ex vivo* fluorescence imaging in mice

Biodistribution studies by fluorescence molecular imaging (FMI) were performed at the Pre-clinical imaging Platform from VHIR (Barcelona) in collaboration with the group of Dr. Anna Rosell, under the technical supervision of Alba Grayston. Ethical approval for the experiments was received by the *Comité d'experimentació animal del Vall d'Hebron Institut de Recerca, procediment 70.18/10860*.

FMI was performed to track the biodistribution of Fe₂O₃@SR-Cy5 *in vivo* and *ex vivo* using a IVIS® Lumina LT Series III imaging system (Perkin Elmer, Waltham, MA). All images were acquired at the following $\lambda_{ex}/\lambda_{em}$ ranges: 625-655 nm/695-770 nm, centered at 640 nm/732 nm, respectively.

To study the *in vivo/ex vivo* biodistribution, C57BL/6JRj adult male mice (8 weeks of age) were injected via the tail vein with 200 μ l of 3 mg/ml Fe₂O₃@SR-Cy5 dispersion in a D-mannitol aqueous solution (55 mg D-mannitol/ml H₂O). For the *in vivo* acquisitions, mice were anesthetized with isoflurane via facemask (5% for induction, 1.5% for maintenance in 95% O₂) and *in vivo* images in the dorsal and ventral views of the whole body were acquired at 30 min and 60 min post-injection. At the end of the scan, mice were euthanized by cervical dislocation under anesthesia and brain, heart, lungs, liver, spleen, and kidneys were dissected to measure the fluorescence of the principal organs *ex vivo*. A control animal was used as a background measurement both *in vivo* and *ex vivo*.

For quantification, circular ROIs were manually drawn surrounding the fluorescence signal and total radiant efficiency (TRE; [photons/s]/[μ W/cm²]) was measured using the Living Image software (Perkin Elmer, Waltham, MA) and corrected by the TRE from the corresponding ROI in the background control animal. For the *in vivo* analysis, abdominal ROIs were drawn on the ventral images due to the position of the organs of interest, and for the *ex vivo* analysis, ROIs of each dissected organ were drawn in both dorsal and ventral positions, and the mean value was considered.

5.8. Chapter references

1. Goessling, W. & Sadler, K. C. Zebrafish: An Important Tool for Liver Disease Research. *Gastroenterology* **149**, 1361–1377 (2015).
2. Tsuchida, T. *et al.* A simple diet- and chemical-induced murine NASH model with rapid progression of steatohepatitis, fibrosis and liver cancer. *J. Hepatol.* **69**, 385–395 (2018).
3. Smith, B. R. & Gambhir, S. S. Nanomaterials for in Vivo Imaging. *Chem. Rev.* **117**, 901–986 (2017).
4. Takahashi, Y., Soejima, Y. & Fukusato, T. Animal models of nonalcoholic fatty liver disease/ nonalcoholic steatohepatitis. *World J. Gastroenterol.* **18**, 2300–2308 (2012).
5. Thit, A., Skjolding, L. M., Selck, H. & Sturve, J. Effects of copper oxide nanoparticles and copper ions to zebrafish (*Danio rerio*) cells, embryos and fry. *Toxicol. Vitro.* **45**, 89–100 (2017).
6. Seok, S. H. *et al.* Arsenite-induced apoptosis is prevented by antioxidants in zebrafish liver cell line. *Toxicol. Vitro.* **21**, 870–877 (2007).
7. Shwartz, A., Goessling, W. & Yin, C. Macrophages in Zebrafish Models of Liver Diseases. *Front. Immunol.* **10**, 2840 (2019).
8. Pham, D. H., Zhang, C. & Yin, C. Using Zebrafish to Model Liver Diseases-Where Do We Stand? *Curr. Pathobiol. Rep.* **5**, 207–221 (2017).
9. Lu, X. *et al.* Microcystin-LR-regulated transcriptome dynamics in ZFL cells. *Aquat. Toxicol.* **212**, 222–232 (2019).
10. Eide, M., Rusten, M., Male, R., Jensen, K. H. M. & Goksøyr, A. A characterization of the ZFL cell line and primary hepatocytes as in vitro liver cell models for the zebrafish (*Danio rerio*). *Aquat. Toxicol.* **147**, 7–17 (2014).
11. Del Campo, J. A. *et al.* Simvastatin and metformin inhibit cell growth in hepatitis C virus infected cells via mTOR increasing PTEN and autophagy. *PLoS One* **13**, e0191805 (2018).
12. von Hellfeld, R., Brotzmann, K., Baumann, L., Strecker, R. & Braunbeck, T. Adverse effects in the fish embryo acute toxicity (FET) test: a catalogue of unspecific morphological changes versus more specific effects in zebrafish (*Danio rerio*) embryos. *Environ. Sci. Eur.* **32**, 122 (2020).
13. Forn-Cuní, G., Varela, M., Fernández-Rodríguez, C. M., Figueras, A. & Novoa, B. Liver immune responses to inflammatory stimuli in a diet-induced obesity model of zebrafish. *J. Endocrinol.* **224**, 159–170 (2015).
14. Chen, B. *et al.* Microarray Expression Profiling and Raman Spectroscopy Reveal Anti- Fatty Liver Action of Berberine in a Diet-Induced Larval Zebrafish Model. *Front. Pharmacol.* **10**, 1504 (2019).
15. Yu, T., Hubbard, D., Ray, A. & Ghandehari, H. In vivo biodistribution and pharmacokinetics of silica nanoparticles as a function of geometry, porosity and surface characteristics. *J. Control. Release* **163**, 46–54 (2012).
16. Shao, D. *et al.* The shape effect of magnetic mesoporous silica nanoparticles on endocytosis, biocompatibility and biodistribution. *Acta Biomater.* **49**, 531–540 (2017).
17. De Barros, A. L. B. *et al.* Synthesis, characterization, and biodistribution studies of ^{99m}Tc-labeled SBA-16 mesoporous silica nanoparticles. *Mater. Sci. Eng. C* **56**, 181–188 (2015).
18. Godin, B., Chiappini, C., Srinivasan, S. & Alexander, J. F. Discoidal Porous Silicon Particles: Fabrication and Biodistribution in Breast Cancer Bearing Mice. *Adv. Funct.*

- Mater.* **22**, 4225–4235 (2012).
19. Torrealba, D. *et al.* Nanostructured recombinant cytokines: A highly stable alternative to short-lived prophylactics. *Biomaterials* **107**, 102–114 (2016).
 20. Liu, J. *et al.* Effects of Fumed and Mesoporous Silica Nanoparticles on the Properties of Sylgard 184 Polydimethylsiloxane. *Micromachines* **6**, 855–864 (2015).

Chapter 6

Conclusions

6.1. General conclusions

In this thesis, I have presented the synthesis of magnetic and fluorescent mesoporous silica nanorods as a system for future potential application in imaging and therapy of NAFLD.

I developed a reproducible synthesis of mesoporous silica rods of two aspect ratios, namely, 4.7 and 2.2, identified along the thesis as long and short rods. Both types of rods were characterized by a high surface area (up to $\sim 800 \text{ m}^2/\text{g}$) and pore volume (up to $\sim 1 \text{ cm}^3/\text{g}$), and hexagonally-ordered pores of *circa* 5 nm in diameter, oriented parallel to the main rod axis. The pores and the surface of the rods were functionalized with chemical species with the aim of achieving multiple imaging and therapeutic modalities in one system.

A magnetic component, $\gamma\text{-Fe}_2\text{O}_3$ nanoparticles, were crystallized inside the pores using wet impregnation followed by a thermal treatment in reducing atmosphere ($425 \text{ }^\circ\text{C}$, Ar/H_2). The $\gamma\text{-Fe}_2\text{O}_3$ particles (width $\sim 4.9 \text{ nm}$, length $\sim 6.9 \text{ nm}$) had an ellipsoidal shape with a slight preferential growth along the pores, and the slight growth across the pores resulted in deformations of the pore and a decrease of the pore periodicity. The magnetic rods were loaded with $\sim 15\%$ wt. iron oxide, endowing the material with superparamagnetic properties. The performance as T_2 -weighted contrast agent was slightly superior in long rods ($r_2 = 143 \text{ mM}^{-1} \text{ s}^{-1}$) than in short rods ($r_2 = 108 \text{ mM}^{-1} \text{ s}^{-1}$). Cerium oxide, whose therapeutic value against NAFLD has been recently described, was introduced inside the pores. It was observed that a system incorporating ceria and iron oxide species in the pores was magnetic but not crystalline, suggesting a presence of amorphous iron oxide co-localized with Ce^{4+} species. The attempts to load the MSRs with contrast agents for computed tomography did not produce satisfactory results. The materials were also evaluated as US imaging and did not produce contrast comparable to commercially available US contrast products.

Next, I reported a strategy of functionalizing MSRs with APTES to saturate the surface with a stable layer of amine groups endowing the rods with a positive surface charge. The surface character of the rods was then used to functionalize the rods with two fluorophores of distinct emission wavelengths: Cyanine5, producing a material emitting in red ($\sim 730 \text{ nm}$) and fluorescamine, endowing the rods with green light emission (525 nm). Cyanine5-functionalized rods demonstrated good fluorescence performance, allowing their use for *in vivo* imaging in rodents.

In vitro toxicity studies of magnetic rods on ZFL cells indicated that positively and negatively charged long and short rods did not induce cytotoxicity at 6 h exposure for concentrations up to $50 \text{ } \mu\text{g}/\text{ml}$. At $200 \text{ } \mu\text{g}/\text{ml}$, short rods were found to be significantly less cytotoxic towards ZFL cells. The uptake was high and concentration-dependent, and no differences were observed between the uptake of rods with different surface charges. Despite the large size of the rods, it has been

determined by magnetometry studies that a large number of MSRs has been internalized into the cells (up to approximately 500 MSRs per cell after 6 h exposure at a 100 $\mu\text{g/ml}$ concentration). *In vivo* experiments on zebrafish larvae indicated the lack of toxicity at concentrations up to 1000 $\mu\text{g/ml}$. The observation of larvae suggested that the rods might have accumulated in the liver at 24 h, and subsequently passed to the intestine.

The MSRs were demonstrated to be also safe *in vivo* in rodents at 1 h of exposure. *In vivo* biodistribution monitored by MRI has shown accumulation of rods in the liver at 30 min post intravenous injection, which was evident in axial images. Fluorescence imaging *in vivo* studies on mice injected with Cyanine5-functionalized MSRs indicated the presence of the rods in the abdominal area of the animals at 30 min post-injection. The *ex vivo* fluorescence at 1 h post-injection showed similar fluorescence signal intensity in the liver, lungs and kidneys.

I reported a method to quantify the biodistribution of magnetic rods using two distinct techniques, giving similar results – one based on analysing the magnetic remanence of the lyophilized organ samples and the other analysing the Si content of the same samples by ICP-OES. The uptake in the livers of rats at 1 h post-injection was found to be \sim 5-fold higher than in the lungs. Approximately 20% of the rods accumulated in the liver.

Finally, we have also reported that MSRs can be used as catalytic nanomotors after coating half of the rod with a platinum layer. Iron oxide loaded rods displayed superior directional motion compared to empty rods, possibly because of a stabilization effect caused by the release of catalytic products through the pores.

6.2. Outlook and future perspectives

This thesis has opened a new line of research within my host group setting up a robust and reproducible fabrication route for monodispersed magnetic and fluorescent mesoporous silica nanorods. The materials presented in this thesis are proposed as potential theranostic agents targeting liver disease and exhibit features that can be advantageous for this purpose. Namely, the incorporation of multiple functional moieties into the system, no visible toxic effects for the studied concentrations and times and a preferential accumulation in the liver. However, this work is very preliminary and further studies are necessary to confirm the applicability of these materials to this aim. Some of the main challenges are listed below:

- i) A still greater control of the synthesis should be achieved to be able to fabricate rods of many aspect ratios in a predictable way.
- ii) The incorporation of all the discussed functionalities into a single system should be attempted, for both LR and SR.

iii) More studies are needed to determine the stability of fluorophore attachment to the MSRs, to be able to exclude the possibility of fluorophore detachment being the reason for the fluorescence signal observed *ex vivo* in the kidneys of MSR-treated mice.

iv) Detailed toxicity and uptake studies should be performed on human hepatocytes. Attachment of moieties such as N-acetylgalactosamine or lactobionic acid to the rod's surface amines should be considered as it could increase the uptake of the rods by hepatocytes by targeting the ASGPR receptors.

v) The biodistribution of long and short rods has to be compared in rodents, and the time of exposure should be increased to give more information and time-track changes regarding the liver and lung accumulation. The calculated amount of particles present in the liver (approximately 20% of injected dose or 10 %ID/g tissue) could be increased and should be monitored for longer times.

vi) Studies involving animal models of fatty liver disease should be undertaken to assess the performance of MSRs as theranostic agents, starting with zebrafish fed with a high fat diet. The accumulation would be compared between the high fat diet model and control animals. The performance of MSRs incorporating multiple functionalities should be then assessed in NAFLD models in rodents. The distribution of MSRs in rodents with and without attached magnet could be also compared to assess the additional potential for magnetic targeting of the rods.

vii) Considering the abundance of urea in the liver, the fabrication of urea-powered nanomotors by attachment of urease to the surface amines of MSRs is to be considered. The system could allow for the superior transport of the imaging and therapeutic agents inside the liver.

Group of Nanoparticles and Nanocomposites
Institut de Ciència de Materials de Barcelona (ICMAB-CSIC)
nn.icmab.es, [@NNgroupICMAB](https://twitter.com/NNgroupICMAB) / www.icmab.es
Campus UAB, 08193 Bellaterra, Barcelona, Spain



jan93nano@gmail.com
[@jang_nano](https://twitter.com/jang_nano)
[linkedin.com/in/jan-grzelak](https://www.linkedin.com/in/jan-grzelak)

Jan Grzelak

PERSONAL DETAILS

DATE OF BIRTH: 20th October 1993
NATIONALITY: Polish



PERSONAL STATEMENT

I am a PhD candidate in Materials Science with a strong background in nanomaterials, chemistry and physics and an interest in multimodal nanocarriers for medical diagnosis and therapy.

My doctoral research was focused on the synthesis of multifunctional mesoporous silica nanorods for applications as potential theranostic agents for non-alcoholic fatty liver disease (NAFLD). The project required me to optimize the synthesis of such nanomaterials with two different aspect ratios using the sol-gel method and equip them with functional moieties, such as magnetic nanoparticles for magnetic resonance imaging (MRI) synthesized inside silica pores or fluorescent molecules conjugated to the nanomaterial surface used for optical imaging. In order to study the materials in terms of their structure and function, I have employed various lab-based measurement techniques: scanning and transmission microscopy, nitrogen adsorption isotherm, dynamic light scattering and zeta potential, X-ray diffraction, SQUID magnetometry, fluorescence spectroscopy, UV-Vis absorption spectroscopy, FTIR spectroscopy, among others. During the development of my project I have also been able to study the interaction of my materials with cells (zebrafish cell line ZFL and Huh7.5 hepatocytes), and I have learned to culture cells and perform the MTT assay. I have assessed the biodistribution of silica nanorods in zebrafish larvae and in rodents.

Over the course of my research work, I have demonstrated my ability to conduct my research independently and work as part of a team in collaborations with various groups from other research centres (IBB-UAB, IBiS). Apart from research skills, I have also developed strong communication skills by presenting my research on a regular basis at group meetings and conferences.

EDUCATION

Nov. 2017-

**Institut de Ciència de Materials de Barcelona (ICMAB-CSIC),
Barcelona, Spain**

PhD in Materials Science

- Thesis: Magnetic and fluorescent mesoporous silica nanorods towards liver theranostic uses
- PhD thesis advisors: Prof. Anna Roig, Dr. Martí Gich

2015-2017

University of Warsaw,
Warsaw, Poland

MSc Nanostucture Engineering

- Dissertation: Synthesis of supports for catalysis with palladium nanoparticles templated by bacterial cellulose
- Thesis advisor: Dr. Martí Gich, Dr. Anna Laromaine, Dr. Maciej Mazur
- Grade: 5 (out of 5)

2012-2015

University of Warsaw,
Warsaw, Poland

BSc Nanostructure Engineering

- Dissertation: Synthesis and self-assembly studies of plasmonic nanoparticles surface-modified with liquid-crystalline ligands
- Thesis advisor: Dr. Wiktor Lewandowski
- Grade: 5 (out of 5)

RESEARCH EXPERIENCE

Nov. 2017-

Institut de Ciència de Materials de Barcelona (ICMAB-CSIC)
Barcelona, Spain

Predocctoral Researcher within “la Caixa” Foundation

INPhINIT Fellowship programme (H2020/MSCA)

- Development of mesoporous silica nanorods of different aspect ratios
- Development of functionalization strategies in order to introduce imaging modalities
- Structural and functional characterization of the materials

HONORS AND AWARDS

- “la Caixa” Foundation INPhINIT Marie Skłodowska-Curie Fellowship for Doctoral Studies in Spain 2017
- Rector’s Scholarship for best students, University of Warsaw 2014/2015
- Scholarship from the European Social Fund "New challenges - new directions" at the Faculty of Physics, University of Warsaw 2012-2015 (3 times)

RESEARCH SKILLS

- Synthesis of mesoporous silica rods via sol-gel chemistry, and their characterization by conventional lab-based measurement techniques (N₂ adsorption isotherm, TEM, SEM, TGA, DLS)
- Synthesis of magnetic particles and study of their structural and functional properties using XRD, TEM, SEM-EDX, SQUID magnetization measurements
- Functionalization of nanoparticle surface with aminosilanes and its characterization by Zeta potential measurements, FTIR spectroscopy, XPS
- Nanoparticle functionalization with fluorophores with a wide range of emission wavelengths: fluorescamine, Cyanine5 and Cyanine7.5, and material characterization using UV-Vis absorption spectroscopy and fluorescence spectroscopy
- Self-user of SEM, UV-Vis spectrometer, FT-IR spectrometer, fluorimeter, Zetasizer, plate reader
- Synthesis of silver nanoparticles with liquid-crystalline ligands; ligand exchange
- Hands-on experience in cell culture (ZFL and Huh7.5 cells), MTT assay
- Hands-on experience in working with zebrafish larvae

-
- Data analysis using Origin Lab, MAUD, ImageJ, GraphPad Prism programs
 - Use of graphical programs: Inkscape, Blender
 - MS Office: Excel, PowerPoint, Word
 - Basic knowledge of Mathematica, Matlab, C++ Programming

RESEARCH STAYS

- Cell viability and uptake studies performed on zebrafish liver cells (ZFL), uptake studies performed on zebrafish larvae – autonomous work – Evolutionary Immunology Group, Institut de Biotecnologia i Biomedicina (IBB-UAB), Barcelona, Spain. January 2020 – June 2021 (part-time)
- Cell viability assays performed on Huh7.5 cells – training followed by autonomous work - SeLiver Group, Instituto de Biomedicina de Sevilla (IBiS), Sevilla, Spain. March 2020 (2 weeks)

LANGUAGES

- Polish (native proficiency)
- English (excellent – C1)
- Spanish (excellent)
- German (intermediate)
- Chinese (basic)
- Catalan (basic)

PUBLICATIONS

Refereed Papers

- **Nanorods based on mesoporous silica containing iron oxide nanoparticles as catalytic nanomotors: study of motion dynamics**
R. Mestre, N. Cadefau, A. C. Hortelão, **J. Grzelak**, M. Gich, A. Roig and S. Sánchez
ChemNanoMat (2020), doi: 10.1002/cnma.202000557
- **Modifying Thermal Switchability of Liquid Crystalline Nanoparticles by Alkyl Ligands Variation**
J. Grzelak, M. Żuk, M. Tupikowska and W. Lewandowski
Nanomaterials 2018, 8(3), 147; doi: 10.3390/nano8030147

In preparation

- **Magnetic mesoporous silica nanorods of two aspect ratios**
- **Bioevaluation of magnetic mesoporous silica rods: cytotoxicity, cell uptake and biodistribution**

Journal Covers

- **ChemNanoMat 2/07 2021 (author of cover art)**

CONFERENCE PARTICIPATION

- **J. Grzelak**, A. Roig, M. Gich, “Mesoporous silica nanorods as multimodal contrast agents for medical imaging”, *5th Scientific Meeting of PhD Students at UAB Campus*, Bellaterra, Barcelona, 17-18th September 2020 (Poster)
- **J. Grzelak**, A. Roig, M. Gich, “Mesoporous magnetic nanorods for theranostics”, *NanoBio&Med2019 International Conference*, 19-21st November 2019, Barcelona, Spain (Oral presentation)

-
- **J. Grzelak**, A. Roig, M. Gich, “Mesoporous silica nanorods as theranostic platforms”, *International School of Nanomedicine, 4th Course: “Precision Nanomedicine”*, 2-8th July 2019, Erice, Italy (Oral presentation)
 - **J. Grzelak**, A. Roig, M. Gich, “Mesoporous silica nanorods as theranostic platforms”, *12th International Conference and Workshop on Biological Barriers (BioBarriers 2018)*, 27-29th August 2018, Saarbrücken, Germany (Oral presentation)
 - **J. Grzelak**, A. Roig, M. Gich, “Mesoporous silica nanorods as theranostic platforms”, *1st Spanish Conference on Biomedical Applications of Nanomaterials (SBAN)*, Madrid, Spain, 7-8th June 2018 (Poster)

CONFERENCE ORGANIZATION

- Organization and management of scientific conference with over 100 participants, *4th Scientific Meeting of BNC-b Students (JPhD2019)*, Barcelona, Spain, 6-7 June 2019

CERTIFICATES

- MCB63X: Principles of Biochemistry (HarvardX)

OTHER NOTABLE SKILLS AND ACHIEVEMENTS

- Presentation of a seminar “[Face masks during COVID-19 pandemic: materials and reusability](#)” at ICMAB
- Laboratory manager: January-February 2020
- Research group website management (nn.icmab.es): September 2019 – September 2021
- Supervision of a Bachelor’s degree: Marc Cervantes Orús, “*Grafting liquid-sòlid d’aminosilans sobre superfícies de sílice: estudi bibliogràfic del procés per obtenir una funcionalització reproducible sobre nanorods SBA-15*”, Degree in Nanoscience and Nanotechnology, Universitat Autònoma de Barcelona, 2020

HOBBIES

- Volleyball, skiing, music, cinema, traveling, cooking

REFERENCES UPON REQUEST

1. Prof. Anna Roig Serra
ICMAB-CSIC, Barcelona
Tel: +34 935 801 853 Ext. 325
E-mail: roig@icmab.es

2. Dr. Martí Gich Garcia
ICMAB-CSIC, Barcelona
Tel: +34 935 801 853 Ext. 347
E-mail: mgich@icmab.es

3. Dr. Mariana Teles Pereira
IBB-UAB, Barcelona
Tel: +34 93 5813473
E-mail: mariana.teles@uab.cat

4. Dr. Ángela Rojas Álvarez-Ossorio
Institute of Biomedicine of Sevilla (IBiS), Sevilla
Tel: +34 955 923 076/77
E-mail: marojas-ibis@us.es

ICMAB

INSTITUT DE CIÈNCIA DE MATERIALS DE BARCELONA



EXCELENCIA
SEVERO
OCHOA

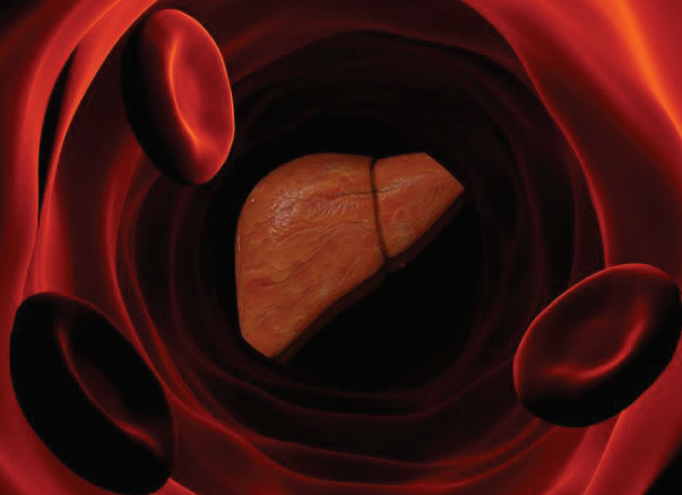


CSIC

CONSEJO SUPERIOR DE INVESTIGACIONES CIENTÍFICAS



GROUP OF NANOPARTICLES
& NANOCOMPOSITES



UAB

Universitat Autònoma
de Barcelona